

UC Santa Cruz

UC Santa Cruz Electronic Theses and Dissertations

Title

Low-Cost Photovoltaics: Luminescent Solar Concentrators And Colloidal Quantum Dot Solar Cells

Permalink

<https://escholarship.org/uc/item/3w1875c1>

Author

Leow, Shin Woei

Publication Date

2014

Copyright Information

This work is made available under the terms of a Creative Commons Attribution License, available at <https://creativecommons.org/licenses/by/4.0/>

Peer reviewed|Thesis/dissertation

UNIVERSITY OF CALIFORNIA
SANTA CRUZ

**LOW-COST PHOTOVOLTAICS: LUMINESCENT SOLAR
CONCENTRATORS AND COLLOIDAL QUANTUM DOT SOLAR CELLS**

A dissertation submitted in partial satisfaction of the requirements
for the degree of

DOCTOR OF PHILOSOPHY

in

ELECTRICAL ENGINEERING

by

Shin Woei Leow

September 2014

The Dissertation of Shin Woei Leow is
approved:

Professor Michael S. Isaacson, chair

Professor Sue A. Carter

Professor Joel Kubby

Tyrus Miller
Vice Provost and Dean of Graduate Studies

Copyright © by

Shin Woei Leow

2014

Table of Contents

Table of Contents	iii
List of Figures	vi
List of Tables	xii
Abstract	xiii
Acknowledgements.....	xvi
I. Introduction.....	1
1 Introduction to Photovoltaics	2
1.1 The Push towards Solar Energy	2
1.2 Solar Cell Current-Voltage Analysis.....	4
1.3 Quantum Efficiency	6
1.4 Practical Solar Cells Devices	8
II. Luminescent Solar Concentrators	11
2 Introduction to LSC	12
3 Design of LSC Panels with Front Facing Solar Cells.....	16
3.1 Introduction	16
3.2 Experimental Methods	18
3.2.1 Construction of LSC panels	18
3.2.2 Optical measurements	18
3.2.3 Electrical measurements.....	20
3.3 Results and Discussion.....	21

3.3.1	Optical properties of the luminescent absorber.....	21
3.3.2	Optimization of LSC panel thickness and panel edge treatment ..	22
3.3.3	LSC panel optimization: design projections and effect of PV cell	24
3.3.4	LSC window demos	30
3.3.5	Cost per watt optimization	36
3.4	Conclusion.....	37
4	Monte-Carlo Ray-Tracing Simulation Model for LSCs	38
4.1	Introduction	38
4.2	Weighted Monte-Carlo Ray Tracing Simulation	40
4.2.1	Photon localization.....	43
4.2.1.1	Line intersection test	44
4.2.1.2	Point-in-Box test	47
4.2.2	Interface interaction	49
4.2.2.1	Reflected and refracted ray calculations	50
	Absorption, emission and scattering	53
4.3	Simulation Results.....	54
4.3.1	Waveguide thickness and cell dimensions	55
4.3.2	Panel layout	58
4.3.3	Response to illumination angle and edge surface treatment	61
4.3.4	LSC loss mechanisms	63
4.4	Comparisons of LSC Layout.....	65
4.5	Summary and Conclusions.....	66
III.	Quantum Dot Solar Cells	68
5	Introduction.....	69
6	Quantum Dot Solar Cells	72
6.1	Quantum Confinement	72
6.2	The Schokley-Queisser Limit.....	74
6.2.1	Carrier generation beyond the SQ limit	74
6.2.2	Charge carrier recombination.....	77

6.3	Synthesis of Quantum Dots.....	78
6.4	Fabrication of QD Solar Cell Devices.....	80
6.4.1	Substrate cleaning	81
6.4.2	Sol-Gel and nano-particle titanium dioxide deposition	81
6.4.3	Quantum Dot deposition	82
6.4.4	Ligands	84
6.4.5	Metallization	86
7	Germanium Quantum Dot Solar Cells	88
7.1	Introduction	88
7.2	Experimental Methods	89
7.3	Results and Discussion.....	91
7.3.1	Thermal Annealing.....	94
7.4	Conclusions	96
8	Silicon Nano-Particle Solar Cells	97
8.1	Experimental Methods	98
8.2	Results and Discussion.....	100
8.3	Conclusion.....	104
	Appendix.....	105
	Bibliography	112

List of Figures

Figure 1.1 Average distribution of worldwide insolation.	3
Figure 1.2 Ideal circuit model of a solar cell	4
Figure 1.3 Current-Voltage (solid) and Power-Voltage (dotted) curves of an ideal solar cell under illumination. The maximum power generated occurs at current and voltage values below I_{sc} and V_{oc} respectively. The ratio of the shaded to the sold rectangle gives the fill factor of the solar cell.	6
Figure 1.4 Schematic of a practical solar cell with parasitic shunt and series resistances.	8
Figure 1.5 Effect of shunt increasing series (A) and shunt (B) resistance on the I-V curve.....	9
Figure 1.6 Schematic of a solar panel with PV cells connected in series. Current mismatch in shaded and un-shaded cells can cause the shaded cell diode to go into reverse bias, and eventually break down and may result in permanent damage to the cell.....	10
Figure 2.1 Schematic of conventional LSC design with side-mounted PV cells (I) with a magnified view of dye molecules embedded in the flexible acrylic sheet (inset); innovative LSC design with front-facing PV cells (II). a, acrylic panel; b, luminescent sheet; c, PV cell; d, incident photon absorbed by luminescent dye; e, photon emitted by luminescent dye, wave-guided and absorbed by PV cell; f, incident photon absorbed by luminescent dye and re-emitted at angle within escape cone; g, dye molecule excited by photon, light is downshifted and re-emitted isotropically; h, downshifted photon is re-emitted into the waveguide; i, dye molecule; and j, direct sunlight absorbed by front-facing PV cell.	14
Figure 2.2 External quantum efficiency of a crystalline silicon solar cell.....	15

Figure 3.1 Integrating sphere setup for measuring re-absorption in the LSC films ...	19
Figure 3.2 LSC masking experimental setup. A single PV cell place in a single large LSC panel with undesired areas masked off to prevent light entry.	21
Figure 3.3 Steady state absorption and photoluminescence emission spectra for LR305 (top). Photoluminescence emission spectra of LR305 embedded in an acrylic sheet for increasing distances between excitation and detection (right). Inset: Molecular structure of LR305.....	22
Figure 3.4 Power gain per area for increasing distances of exposed LSC material to PV cell.....	25
Figure 3.5 Power gain as a function of LSC area surrounding a PV cell in masking experiments and “cut-to-size” windows. Inset: Schematic illustrating that LSC exposed on the long-edge of the PV cell contributes greater power gain than the LSC on the short-edge of the cell. All PV cells have dimensions 12.5 x 1cm or 12.5 x 2cm.	26
Figure 3.6 Power gain as a function of percentage LSC area. The projection line (purple) calculates the LSC panel gain required for the overall panel conversion efficiency to hit 6% with the ratio of PV cells used for a given area. In this graph, the PV cells were assumed to have 18% power conversion efficiency	27
Figure 3.7 Cell width demos. A: panel with one 1 cm wide PV cell; B: panel with two 1 cm wide PV cells; C: panel with one 2 cm wide PV cell.	29
Figure 3.8 Different testing methods: (1) flash tester; (2) outside with demo lying flat; (3) outside with demo tilted towards the sun.	31
Figure 3.9 Design of LSC windows. A: 2x power gain; B: 6% panel efficiency; C: Tic-Tac-Toe; D: 1 cm Zig-Zag; E: 2 cm Zig-Zag. Sample layouts showing potential escape zones (F) and superior light trapping (G).....	34
Figure 4.1 Schematic of the LSC panel with 100 incident photons.a: Incident photon; b: Wave-guided photon; c: PV cell; d: Luminescent layer; e: Waveguide.....	41

Figure 4.2 Ray-tracing algorithm flow chart. The simulation is broken up into several distinct mutually exclusive interactions, namely the interface and layer effects on the photon. Determining the photon location applies the appropriate action for each iteration.	43
Figure 4.3 Vector diagram illustrating the line intersection test. \mathbf{u} and \mathbf{v} are the unit vectors of each line. \mathbf{w} is a vector joining the points of origin for each line and $P(s)$ the point of intersection.	44
Figure 4.4 Vector diagram illustration ray-plane intersection (A) and sum of angles test (B).....	46
Figure 4.5 Definition of plane normal for all planes bounding a region of space	49
Figure 4.6 Vector diagram illustrating the calculation of a reflected ray vector from the incident ray vector and the plane normal unit vector.....	51
Figure 4.7 Vector diagram illustrating the calculation of a refracted ray vector using the incident ray vector and the plane normal unit vector.....	51
Figure 4.8 Visualization of simulated wave-guided rays in the LSC panel with an incident spot size of 5mm and an entry angle.....	55
Figure 4.9 Illustration of the effect waveguide thickness and PV cell width has on the transport efficiency of photons to the PV cell.	56
Figure 4.10 Percentage of photons collected by PV cell through waveguiding action versus the waveguide (acrylic) thickness for a single 1x12.5cm or 2x12.5 cm wide cell.....	57
Figure 4.11 Waveguided photons absorbed by the PV cell are counted and grouped by the position absorbed. PV cell width is divided into 500 μ m sections each representing a group. Waveguide thickness: 4.76mm	58
Figure 4.12 Power gain versus 1-sided LSC panel width. PV cell width:2cm, Photons incident angle: 0 deg with respect to plane normal.....	59
Figure 4.13. Power gain versus the size of exposed LSC, comparing experimental (triangle) and simulation (diamond) results	60

Figure 4.14 Apportion of photons collected by the PV cell as a function of the incident illumination angle. (a) % of photons referenced to the total number of incident photons on the LSC panel. Light intensity is reduced for larger angles as light is spread over a larger area (b) % of photons referenced to the maximum number of incident photons possible (0 degrees) on the LSC	61
Figure 4.15 Power gain as a function of the incident illumination angle, with (solid line) and without (dotted line) reflective edges.	63
Figure 4.16 Photon distribution in the LSC with (circle) and without (cross) reflective edges. Non-radiative and escape cone losses from single and multiple absorption events are classified separately. Losses from multiple absorptions are grouped collectively under re-absorption losses. Top-reflection refers to incident light reflecting off the top of the waveguide. Photons collected by the PV cell are also separated into those from direct irradiation and those channelled by the waveguide. Photons which pass through the LSC panel without undergoing any absorption or scattering are classified as unabsorbed.	63
Figure 4.17 Distribution of photon losses in response to increasing panel size. Similar to Figure 4.16, losses from multiple absorption events are grouped into the Reabsorb category.....	65
Figure 4.18 Simulation model and results of three panels with the same PV to luminescent area ration but different layout of PV cells.....	66
Figure 5.1 Broad-band absorption of the solar spectrum by multi-junction tandem solar cells	70
Figure 5.2 Example of a window coated with optically transparent/semi-transparent PV material	71
Figure 6.1 Absorbance and emission spectra of PbS nano-particles increasing in size from ~3nm (left) to ~7nm(right) (reproduced with permission).....	73
Figure 6.2 Multiple exciton generation via impact ionization.....	76

Figure 6.3 Schematic representation of sol-gel synthesis and subsequent processing routes.....	80
Figure 6.4 Sample images of spun cast (A), dip coated (B), doctor blade (C) and drop casted (D) QD films on glass	82
Figure 6.5 Doctor blade coating process.. The blade is use to shear the colloidal nano-particle into a evenly distributed film with the guides determining the thickness of the deposited material.	83
Figure 6.6 Schematic of the ligand exchange process. Shorter ligands result in a closer packed structure which reduces the tunneling barrier width.	86
Figure 6.7 Top down layout and cross sectional view of the quantum dot solar cell structure. Overlap between the metal leads and ITO defines the device area.	87
Figure 7.1 Powder X-ray diffraction measurement of the germanium nano-particles	90
Figure 7.2 Absorbance measurements of Ge nano-particle films fabricated with three spin-cast cycles. Inset: image of the films deposited.	91
Figure 7.3 J-V curves of Ge quantum dot solar cells with nano-particles ranging from 3-7nm taken in the dark (dotted) and under AM1.5 solar illumination (solid).....	92
Figure 7.4 J-V cures of Ge nano-particle devices with increasing number of spin-cast cycles (thickness). Dotted lines indicate dark curves and solid lines are light curves.	93
Figure 7.5 (A) J-V curves of Ge nano-particle devices annealed at 0, 80, 120, 200 and 300°C for 10 mins. (B) Plot of J_{sc} and V_{oc} versus anneal temperature. All Ge films deposited using AI553 for 3 spin-cast cycles.	95
Figure 7.6 Log plot of the absorbance curves for thermally anneal Ge nano-particle films. Anneal temperatures at 0, 80, 120, 200 and 300°C.	96
Figure 8.1 Concentrating Si-np solutions to produce sufficiently thick films during the drop cast process	98
Figure 8.2 (A) Si-np in DI water drop cast in air; (B) Si-np in DI water drop cast under 25" hg vacuum; (C) Si-np in Pyridine drop cast in air; (D) Si-np in Pyridine	

drop cast under 25 " hg vacuum. (E) ITO-Si-np schottky diode formed by vacuum drop cast of 100µl Si-np solution; (F) ITO-Si-np schottky diode formed by vacuum drop cast of 50µl Si-np solution;.....	99
Figure 8.3 (A) Absorbance spectrum of a 100µl drop-cast Si-np film; (B) Photoluminescence spectrum of a 100µl drop-cast Si-np film.	101
Figure 8.4 J-V curves with (solid) and without (dotted) illumination of Si-np Schottky diodes, made using the drop-cast technique with 100µl (green) or 50µl (yellow) of Si-np colloidal solution. Bias voltage swept from -1V to +1V.	102
Figure 8.5 (A) Dark J-V curves: Si-np 100µl drop-cast Schottky device; (B) Illuminated J-V curves: Si-np 100µl drop-cast Schottky device; (C) Dark J-V curves: Si-np 50µl drop-cast Schottky device; (D) Illuminated J-V curves: Si-np 50µl drop-cast Schottky device.....	103

List of Tables

Table 3.1 Power output for various acrylic edge treatments.	24
Table 3.2 Power output and power gain for cell width demos in Figure 3.7.	30
Table 3.3 Summary of variations in power gain and efficiency for different testing methods.	32
Table 3.4 LSC window performance summary. Power gain and panel efficiency measured with flash tester.	32
Table 3.5 Cost per watt for all demos. The right-most column was calculated with \$1.90/W (Sun Power cells) converted to cost/m ² for 20% efficient cells.	36

Abstract

Low-cost photovoltaics: luminescent solar concentrators and colloidal quantum dots
solar cells

By

Shin Woei Leow

Solar energy has long been lauded as an inexhaustible fuel source with more energy reaching the earth's surface in one hour than the global consumption for a year. Although capable of satisfying the world's energy requirements, solar energy remains an expensive technology that has yet to attain grid parity. Another drawback is that existing solar farms require large quantities of land in order to generate power at useful rates. In this work, we look to luminescent solar concentrator systems and quantum dot technology as viable solutions to lowering the cost of solar electricity production with the flexibility to integrate such technologies into buildings to achieve dual land use.

Luminescent solar concentrator (LSC) windows with front-facing photovoltaic (PV) cells were built and their gain and power efficiency were investigated. Conventional LSCs employ a photovoltaic (PV) cell that is placed on the edge of the LSC, facing inward. This work describes a new design with the PV cells on the front-face allowing them to receive both direct solar irradiation and wave-guided photons emitted from a dye embedded in an acrylic sheet, which is optically

coupled to the PV cells. Parameters investigated include the thickness of the waveguide, edge treatment of the window, cell width, and cell placement. The data allowed us to make projections that aided in designing windows for maximized overall efficiency. A gain in power of 2.2x over the PV cells alone was obtained with PV cell coverage of 5%, and a power conversion efficiency as high as 6.8% was obtained with a PV cell coverage of 31%. Balancing the trade-offs between gain and efficiency, the design with the lowest cost per watt attained a power efficiency of 3.8% and a gain of 1.6x.

With the viability of the LSC demonstrated, a weighted Monte-Carlo Ray Tracing program was developed to study the transport of photons and loss mechanisms in the LSC to aid in design optimization. The program imports measured absorption/emission spectra of an organic luminescent dye (LR305), the transmission coefficient and refractive index of acrylic as parameters that describe the system. Simulations suggest that for LR305, 8-10cm of luminescent material surrounding the PV cell yields the highest increase in power gain per unit area of LSC added, thereby determining the ideal spacing between PV cells in the panel. The model also predicts that for different PV cell dimensions, there exists an optimum waveguide thickness which efficiently transports photon collected by the waveguide to the PV cell with minimal loss, and maintains an even distribution of photons across the cell surface. For the case of the 12.5 by 1cm rectangular cells used in this work, the calculated waveguide thickness is 3mm. For larger cells, every 1cm increment in PV cell width

should be accompanied by a 0.75mm increase in waveguide thickness to preserve peak performance.

In line with the goal of pushing for cost competitive photovoltaics, the last part of this work shifts to the study of colloidal quantum dot solar cells. A combination of low temperature, highly scalable fabrication process and reduced material usage for thin films offers us a means to produce flexible and cheap solar cells. Tagging on to existing work already performed on germanium quantum dot solar cells, additional work was carried out to further characterize the material. The effect of film thickness, nano-particle surface conditions and thermal anneal were investigated. There is evidence to suggest that the quantum dot devices contain high levels of parasitic resistances. Short circuit current densities increase by up to two times with two spin-cast layers compared to four, leading to the conjecture that charge carrier life time is low with high levels of recombination. Annealing to improve carrier mobility produces devices with current densities up to $301\mu\text{A}$, a fourfold increase, but output voltages saw a sharp decrease from 0.12V to 0.015V.

In tandem with the work on germanium, experiments on silicon quantum dots were also carried out to investigate their viability for use as photovoltaic devices. The stronger bonds formed by silicon hindered the ligand exchange process. Schottky diodes were made via drop casting and displayed a clear photovoltaic effect albeit with very low current densities. Interestingly, an open circuit voltage was observed even when not under illumination and further investigations are ongoing.

Acknowledgements

Support for the work on luminescent solar concentrators was provided by the U.S. Department of Energy grant No. DE-EE0003455 and by the University of California Discovery grant No. 192864. Portions of this work were performed at the Molecular Foundry and were supported by the Office of Science, Office of Basic Energy Sciences, of the U.S. Department of Energy under Contract No. DE-AC02-05CH11231. I would also like to thank Jeremy Olson, Nathan Green, Shila Alavi, and Glenn Alers at APV Research for sharing their knowledge on panel construction and their help in data collection. Many thanks as well to Dave Thayer in the Wood Shop at UCSC for his advice on a variety of construction ideas.

I would like to acknowledge the NSF Solar program (NSF DMR 1035478) for providing financial support for the research on quantum dot solar cells. Many thanks to our collaborators at UC Davis, Raja, Bradley and Susan for the useful discussions on research and for providing the nano-particles used in our studies

I am deeply grateful for the support and guidance received from my advisors Dr Sue Cater and Dr Michael Isaacson. Their patience with me despite switching through several projects has allowed me the flexibility to experience research on a range of topics that broaden my knowledge base. I would also like to express my thanks to all members of Carter lab for their companionship and assistance especially Ben, Guangmei, Carena, Carley, Ian, Derek and Leila. Many thanks as well to friends I've made in Santa Cruz and Berkeley for keeping me sane and upbeat. My thanks to

Sensei Yoshi, Wink and Chris of UCSC Aikido for all the fun times during training and always giving me something to focus on every week besides work.

I am eternally grateful to my parents and brother without whose support, love and encouragement, I would not be able to pursue this path. Lastly, special thanks to my loving wife, Siew Chin, for providing the impetus that started me down this journey in the first place, a dream that I had almost lost sight of. I am thankful for her love and care and for sharing with me the ups and downs throughout this adventure.

I. Introduction

1 Introduction to Photovoltaics

1.1 The Push towards Solar Energy

The worldwide solar energy market has experienced rapid growth in recent years, with installation of new photovoltaic (PV) panels in the US almost doubling year on year. This trend is expected to continue with increasing adoption of solar power, aided by the falling cost of solar generated power [1], [2] and rising prices of fossil fuels. Figure 1.1 shows the distribution of worldwide isolation. It is clear from the map that many industrialized and rapidly industrializing countries lie outside the hot zone. Depending on regional sunlight conditions, solar power is usually not competitive enough compared to fossil fuels. Although the total required land area to meet the world's current energy needs is relatively small, issues such as distribution and reliability have to be factored in if we are to gain wide acceptance for solar energy. The first steps to improving competitiveness are to trim manufacturing and installation cost of solar panels and enhance PV cell conversion efficiencies.

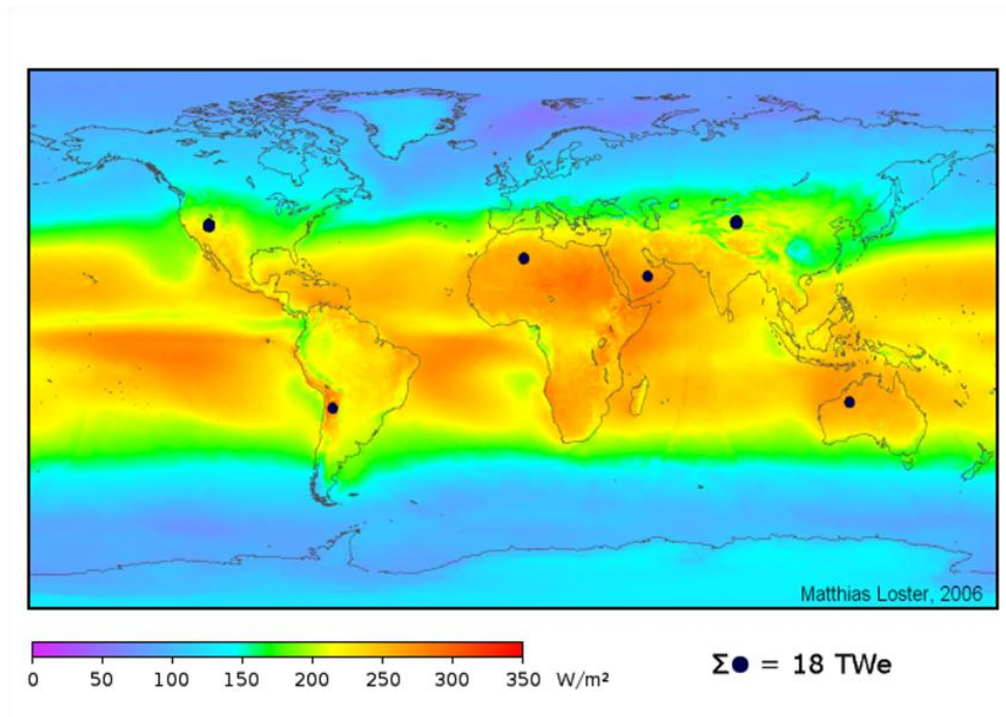


Figure 1.1 Average distribution of worldwide insolation.

Building Integrated Photovoltaics (BIPV) is becoming an increasingly attractive method to supplement the high energy needs of today's dense urban cities by generating some of the buildings power requirement on-site[3]. Countries with low specific land use per capita can hardly spare the extra land area and not to mention the additional environmental cost in building large centralized PV plants[4]. PV solutions utilizing existing spaces would thus be a preferred option. There has been increased interest in studying the performance of BIPV and their use [5]–[7], but we must first make it cost effective and easy to implement if wide adoption of solar energy is to be achieved.

1.2 Solar Cell Current-Voltage Analysis

Solar cells are essentially semiconductor diodes capable of absorbing electromagnetic waves, and generating charge carriers that can be separated and collected before recombination occurs. An ideal solar cell is thus modeled as a diode in parallel with a light controlled current source[8], [9].

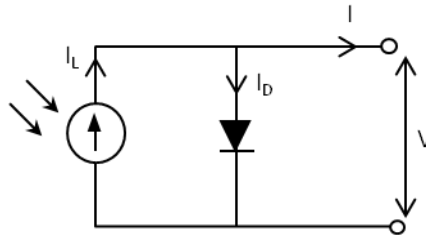


Figure 1.2 Ideal circuit model of a solar cell

From Figure 1.2, when no illumination is present, what we have is just a simple diode with the dark output current (I_{dark}) equal to the diode current I_D .

$$I_{\text{dark}} = -I_D = -I_o \left[\exp\left(\frac{qV}{kT}\right) - 1 \right] \quad (1.1)$$

Where I_o is the reverse saturation current, k is Boltzmann's constant and T is the temperature in Kelvin. When photo current is present the current-voltage (I-V) relationship becomes

$$I_{\text{light}} = I_L - I_D = I_L - I_o \left[\exp\left(\frac{qV}{kT}\right) - 1 \right] \quad (1.2)$$

The short circuit current (I_{sc}) and the open circuit voltage (V_{oc}) are two often mentioned terms which represent the maximum possible current and maximum voltage a PV cell can generate. To obtain I_{sc} , the output voltage (V) is set to 0V. In the ideal model, I_D drops to zero and I_{sc} equals I_L , the light generated current. Similarly, to obtain V_{oc} , the output current is set to zero and we have:

$$V_{oc} = \frac{kT}{q} \ln \left(\frac{I_{sc}}{I_o} + 1 \right) \quad (1.3)$$

V_{oc} is related to the difference in work function between the junction materials and their band gaps. It shows the maximum amount of energy available to do work in the system. A solar cell operating at either of these maximum points however produces no power. Figure 1.3 plots the current-voltage and power-voltage relationship of a PV cell. A performance parameter termed the “fill factor” (FF) measures how good a fit the I-V curve is to I_{sc} and V_{oc} by comparing the ratio of shaded rectangle to the solid rectangle in Figure 1.3.

$$FF = \frac{I_{max} V_{max}}{I_{sc} V_{oc}} \quad (1.4)$$

The power conversion efficiency, η_{PE} , is defined as the power delivered at the maximum operating point taken as a fraction of the incident illumination power (P_{in}).

$$\eta_{PE} = \frac{I_{sc} V_{oc} FF}{P_{in}} \quad (1.5)$$

Since output current increases linearly with the cell area, current density, $J_{sc}=I_{sc}/\text{Area}$, is frequently used in place of I_{sc} in the above calculations to permit direct comparison of performance between solar cells.

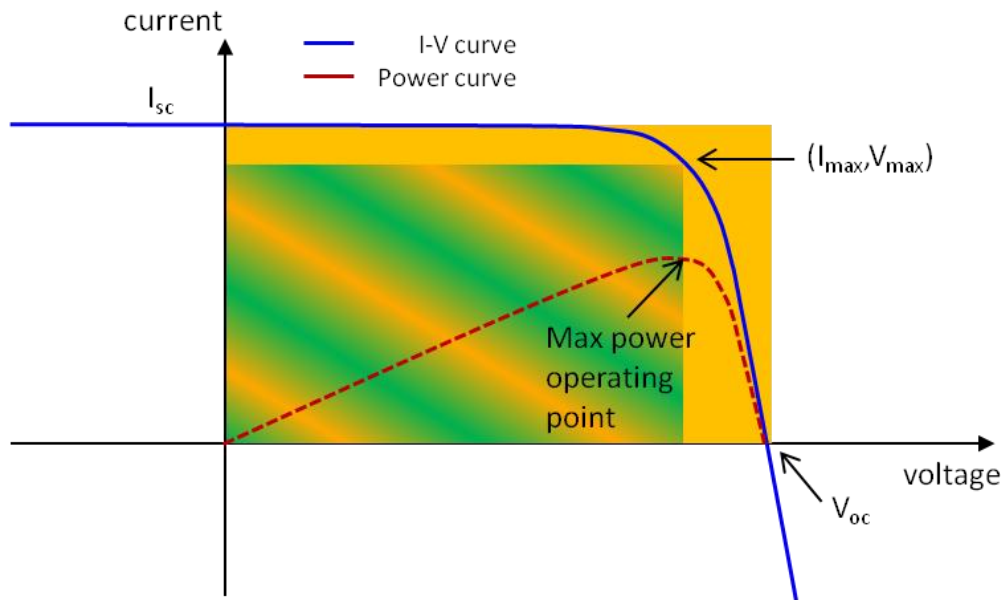


Figure 1.3 Current-Voltage (solid) and Power-Voltage (dotted) curves of an ideal solar cell under illumination. The maximum power generated occurs at current and voltage values below I_{sc} and V_{oc} respectively. The ratio of the shaded to the solid rectangle gives the fill factor of the solar cell.

1.3 Quantum Efficiency

The quantum efficiency of a solar cell measures the rate of carrier generation versus the illumination intensity at a particular wavelength. The energy of a photon is related to its wavelength, λ , and speed, c , by the equation:

$$E_{\text{photon}} = \frac{hc}{\lambda} \quad (1.6)$$

Ideally, each photon with energy greater or equal to the semiconductor band-gap will liberate one valence electron which is then extracted from the device. External quantum efficiency (EQE) includes all external power incident on the cell.

$$\text{EQE} = \frac{\text{electrons/sec}}{\text{photons/sec}} = \frac{I/q}{(\text{total incident power})/E_{\text{photon}}} \quad (1.7)$$

EQE is thus an indicator of absorption efficiency of the device and the severity of surface reflection. The current density J_{sc} can be estimated by performing an integration of EQE over the entire illumination spectrum.

Internal quantum efficiency (IQE) is similar to EQE but discounts reflected and transmitted photons and only consider photons absorbed by the solar cell.

$$\text{IQE} = \frac{\text{electrons/sec}}{\text{absorbed photons/sec}} = \frac{\text{EQE}}{1 - R - T} \quad (1.8)$$

Where R and T are the reflection and transmission coefficient respectively. IQE is thus a direct measurement of recombination and how well a device is able to utilize photons. Poor mobility or short diffusion lengths suppress both EQE and IQE. This is somewhat related to the photon wavelength, with E_{photon} absorbed decreasing with increasing depth in the device. Electron-hole pairs that are generated far from the electrical contacts have a higher probability to recombine before they can be collected.

Quantum efficiency is measured by filtering light from a solar simulator through a monochromator to produce wavelength-specific current, which is then compared to the known response of a Silicon diode.

1.4 Practical Solar Cells Devices

In practice, solar cells are not simple diodes and contain many parasitic losses which can be modeled as a shunt (R_{sh}) and series (R_s) resistor in the equivalent circuit shown in Figure 1.3.

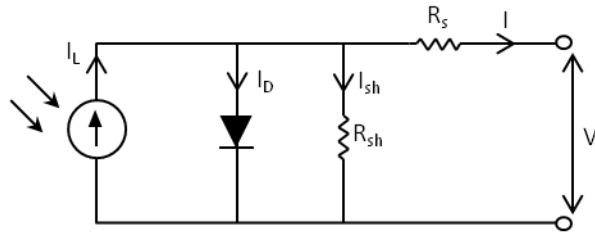


Figure 1.4 Schematic of a practical solar cell with parasitic shunt and series resistances.

Taking these into account, the current-voltage relationship is now given by:

$$I = I_L - I_D - I_{sh} = I_L - I_o \left[\exp\left(\frac{qV + IR_s}{kT}\right) - 1 \right] - \frac{V + IR_s}{R_{sh}} \quad (1.9)$$

Series resistance increases the voltage drop between the output terminals and the diode. Thus for any output current I , output voltage V is lowered in effect pulling the

current controlled section of the I-V curve toward the origin (Figure 1.5A). Series resistance is of greater concern at higher current densities, especially in solar concentrator systems.

The shunting pathway bleeds current away reducing output current, I , at each level of voltage. This causes the voltage controlled portion of the I-V curve to be shifted down toward the origin (Figure 1.5B). At very low resistances, V_{oc} is severely reduced. Low shunt resistances are a result of leaky device with poor rectifying characteristics. The impact of both parasitic resistances is a small FF and lower conversion efficiencies.

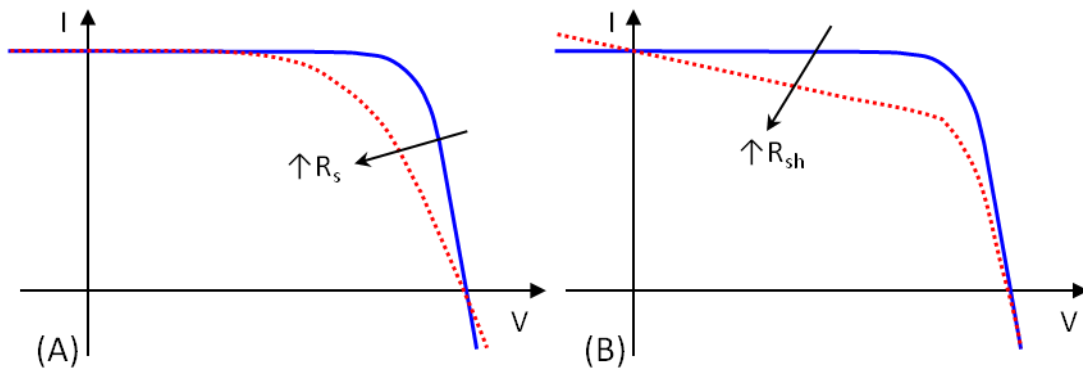


Figure 1.5 Effect of shunt increasing series (A) and shunt (B) resistance on the I-V curve

It is common in PV panels to have strings of solar cells connected in series instead of in parallel. This is so as to avoid having high current flowing in the panel and the corresponding resistive losses. The short coming of such a design is its susceptibility to shading effects, where one or several cells in the string receive less

illumination, thus lowering the photo-current of those cells (Figure 1.6). The mismatch in current not only reduces the overall current and voltage of the panel, but also forces current through the shaded diodes, pushing them into reverse bias. Severe mismatch could lead to diode breakdown and if the condition persists, joule heating could induce permanent physical damage, making recovery impossible[10]–[12]. Bypass diodes and circuits are often built into such panels to avoid or reroute the excess current.

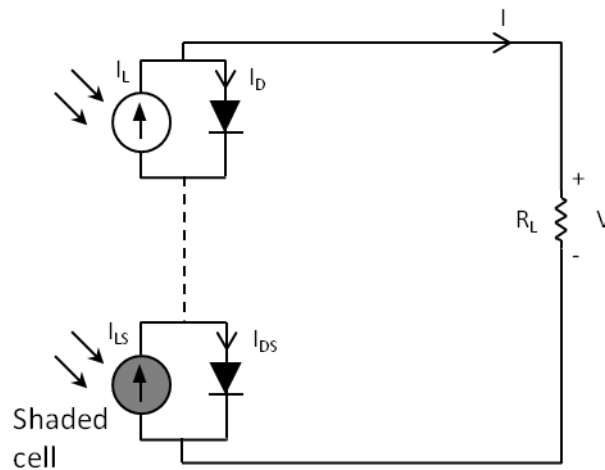


Figure 1.6 Schematic of a solar panel with PV cells connected in series. Current mismatch in shaded and un-shaded cells can cause the shaded cell diode to go into reverse bias, and eventually break down and may result in permanent damage to the cell

II. Luminescent Solar Concentrators

2 Introduction to LSC

Luminescent Solar Concentrators (LSCs) consist of a flat transparent matrix with luminescent particles, such as organic dyes, quantum dots (QDs), or semiconducting polymers [13]–[20] dispersed uniformly within it. Incident light entering the panel is absorbed by the luminescent particles and reemitted at longer wavelengths, with a fraction whose emission angle is larger than the critical angle, remaining trapped in the waveguide through total internal reflection and is later redirected to the PV cells for collection, as illustrated by Figure 2.1. This effectively concentrates light from the larger surface area of the panel onto a smaller PV area, thus increasing the power output of the cell.

This idea was first proposed in the late 70's [21]–[24] and has received renewed interest due to recent availability of more stable and efficient luminescent materials. Constructed out of inexpensive materials and with low processing outlay, the cost per watt of LSC panels can be lower than current PV panels. The ability to concentrate both direct and diffuse light negates the need for expensive solar tracking systems and improves robustness of the LSC panels to shading effects. This allows PV technology to be incorporated into building designs such as façade claddings and roof top fixtures. With tunable color and partial transparency, the technology can also be applied to windows, skylights and greenhouse panels [3], [5], [25]–[27] and is collectively referred to as building integrated photovoltaics (BIPV).

Unfortunately, no one material possesses all the requisite qualities to make an ideal LSC and each material suffers from one or more shortcomings such as a narrow absorption band, self absorption, poor Stoke's shift, low quantum efficiency or rapid degradation[28]. These effects can result in an LSC yielding lower power output than the PV cell used in the LSC, if the PV cell was directly exposed to solar irradiation.

A common configuration for LSC panels is to have the PV cell mounted onto the side of the panel, as in Figure 2.1 (I). While doing so achieves a high concentration factor, the optical efficiency of the panel is often compromised by losses from both self-absorption and light transmission from the limited absorption bandwidth of the luminescent absorbers. Measured panel power conversion efficiencies¹ up to 7.1% have been reported with this configuration [13]–[16], [21], [28]–[30]; however this result was obtained using a low concentration factor² of 2.5, a diffusive backside reflector, and expensive, high efficiency, GaAs PV cells.

¹ power conversion efficiency = incident solar power/converted electrical power

² concentration factor is a ratio of the LSC to PV cell surface area

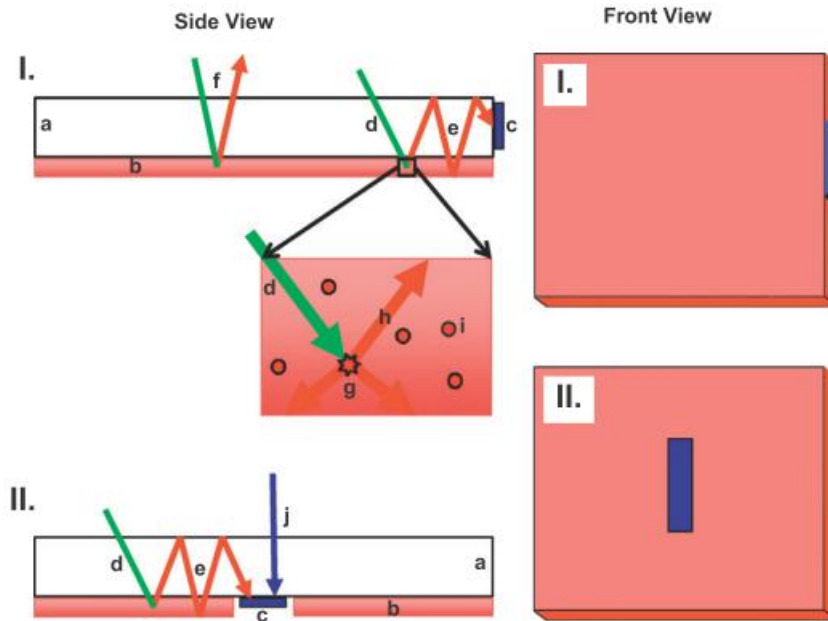


Figure 2.1 Schematic of conventional LSC design with side-mounted PV cells (I) with a magnified view of dye molecules embedded in the flexible acrylic sheet (inset); innovative LSC design with front-facing PV cells (II). a, acrylic panel; b, luminescent sheet; c, PV cell; d, incident photon absorbed by luminescent dye; e, photon emitted by luminescent dye, wave-guided and absorbed by PV cell; f, incident photon absorbed by luminescent dye and re-emitted at angle within escape cone; g, dye molecule excited by photon, light is downshifted and re-emitted isotropically; h, downshifted photon is re-emitted into the waveguide; i, dye molecule; and j, direct sunlight absorbed by front-facing PV cell.

A second effect of LSC's is the downshifting of the incoming spectrum during the absorption-emission process, to one in which the PV cell has higher external quantum efficiency(EQE) [31], [29], [30], [21], [13], [16], [14], [15], [28], [32]–[34]. Figure 2.2 shows an example of a crystalline silicon solar cell's EQE plot, where more charge extraction and thus higher current is obtained moving from wavelength 300 to 600nm. By tuning the emission wavelength of the LSC to match cell performance, potentially higher power output can be achieved for the same area of PV cell used.

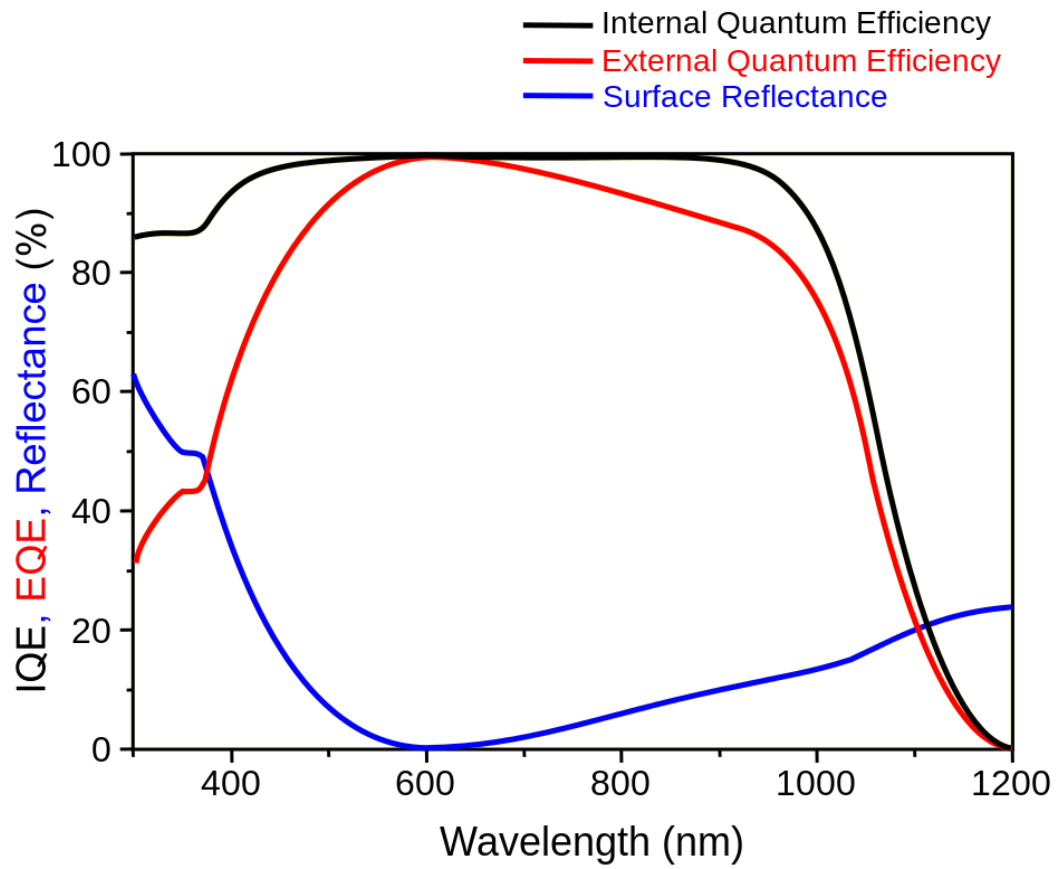


Figure 2.2 External quantum efficiency of a crystalline silicon solar cell

3 Design of LSC Panels with Front Facing Solar Cells

3.1 Introduction

In this chapter, I report on the effect various LSC panel design parameters have on the performance of front-facing solar cells mounted on the back of the panel. A performance parameter gain (γ_{pwr}), is defined to measure the increase in output power of PV cells, attributed to the addition of luminescent absorbers to the panel. The control consists of PV cells with equivalent PV area and position attached to clear waveguides. In this definition, the fill factors for all PV cells used in experiments are presumed to be equal which agrees with our actual measurements.

$$gain = \gamma_{pwr} = \frac{Power_{panel}}{Power_{ctrl}} = \frac{Power_{LSC} + Power_{PV}}{Power_{PV}} \quad (3.1)$$

In a bid to increase the power output of the LSC panel, we have adopted a design with the PV cells mounted front facing, surrounded by luminescent material to capture both direct sunlight and wave-guided concentrated light, as shown in Figure 2.1[35]. Such a layout inherently guarantees that γ_{pwr} per cell is greater than one and imparts flexibility with cell positioning and area coverage when attempting to balance the level of light concentration against losses from re-absorption. In addition, as opposed to having luminescent material dispersed uniformly in the LSC panel, it is instead separated into a thin absorbing layer attached to a much thicker waveguide,

thereby extending the mean-free-path of photons between absorption events [36], [37].

Efficiency of the system can be determined from

$$\eta_{panel} = \left(\frac{A_{PV}}{A_{panel}} \right) \eta_{PE} + \left(\frac{A_{LSC}}{A_{panel}} \right) \eta_{PL} \times \eta_{abs} \times \eta_{WG} \times \eta_{DC} \times \eta_{MPE} \quad (3.2)$$

Where A is the area and η is the efficiency. The subscripts panel, PV, PE, LSC, PL, abs, WG, DC, MPE refer to the overall LSC panel, PV cell, PV conversion efficiency, luminescent material, dye photoluminescence, dye absorption, waveguide, wavelength down-conversion and efficiency at emission wavelength respectively.

A commercial purchased dye, Lumogen Red 305 (LR305), and silicon PV cells were used in the panel construction, thus fixing the values of η_{PE} , η_{PL} , η_{abs} , η_{DC} and η_{MPE} . Experiments were carried out to determine PV to LSC ratio and PV cell placement in order to optimize A_{PV}/A_{panel} and A_{LSC}/A_{panel} . Waveguide thickness and edge properties were also varied to enhance waveguide efficiency (η_{WG}) to effect maximum photon collection for the size of the PV cells used. The highest gain obtained from a LSC panel is 1.8 and on an alternate design, the highest power conversion efficiency achieved was 6.8%.

3.2 Experimental Methods

3.2.1 Construction of LSC panels

Photovoltaic cells (Sun Power, unless otherwise noted), 1 cm x 12.5 cm and 2 cm x 12.5 cm in dimension, were optically attached (Sylgard 184 silicone elastomer, unless otherwise noted) to a clear, rigid, acrylic panel. Flexible acrylic sheets, 500 μm thick embedded with LR305 dye, were fused (Weld-On 4SC solvent) to clear spaces on the acrylic panels surrounding the PV cells (Figure 2.1II). The thin LR305 embedded sheets acts as the absorbing layer for incident photons while the clear acrylic serves as a waveguide for concentrating those photons. PV cells and luminescent material were arranged in various configurations to study how cell placement affects power output and gain in the LSC window (or panel, words used interchangeably).

3.2.2 Optical measurements

Steady-state absorption spectra of the LSC were taken using an N&K UV-vis spectrometer. Steady-state photoluminescence (PL) spectra were measured with an LS-45 Perkin Elmer spectrometer.

To measure photon re-absorption levels in the LSC material, a sample of the luminescent dye embedded in PMMA was attached to an acrylic waveguide. The edge was inserted into an integrating sphere (Labsphere), which was attached to a spectrometer (Ocean Optics). The spectrum of light emitted from the edge was

recorded as the AM1.5 light source is moved further away from the integrating sphere input port. Figure 3.1 illustrates the test setup.

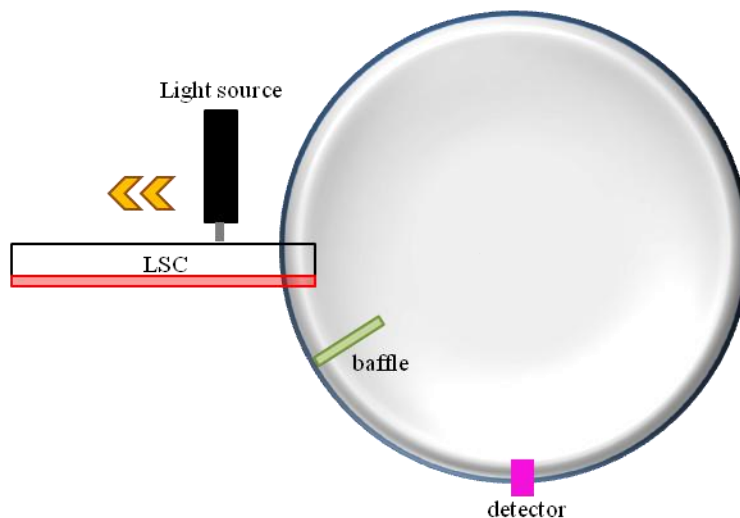


Figure 3.1 Integrating sphere setup for measuring re-absorption in the LSC films

Quantum yields of solid films were measured using an integrating sphere (Horiba JobinYvon) attached to a Fluorolog-3 spectrometer (Horiba). Films were mounted in a solid sample holder at 22.5 degrees incidence to the incoming 573-nm excitation. Excitation and luminescence measurements were collected at a 90° angle from incidence through a 1 nm slit. Dark spectra were subtracted from sample spectra, and then intensity values at each wavelength were corrected based on prior measurements of a calibrated light source. The integrated areas of the excitation peaks (568-580 nm) relative to those of the corresponding blank samples were used to determine absorbed photon counts. The emission photon counts, i.e. the integrated areas of the emission

peaks (578-780 nm) were divided by the absorbed photon counts to arrive at the quantum yield.

3.2.3 Electrical measurements

The short circuit current I_{sc} , open circuit voltage V_{oc} , and resulting output power were measured using a Fluke 26 III multimeter. The measurements were taken outdoors lying flat unless otherwise noted. To obtain a correlation between the area of luminescent material surrounding the PV cell and the gain, we employed a masking setup, as shown in Figure 3.2, where a single PV cell is placed in the middle of a large LSC panel ($45.7 \text{ cm} \times 45.7 \text{ cm}$). To simulate the effect of smaller panels, undesired areas of the LSC panel were covered with a mask template. The LSC area was sequentially increased and the current and voltage values recorded. The resulting extracted power was compared against the power of a reference PV cell and the solar irradiance during the experiment (using a pyranometer, Apogee MP-200) to obtain the gain and solar conversion efficiency, respectively. The reference reading used was obtained by masking off all luminescent material leaving only the PV cell under clear acrylic exposed. Both 1 cm wide and 2 cm wide cells were tested using the same experimental set up.

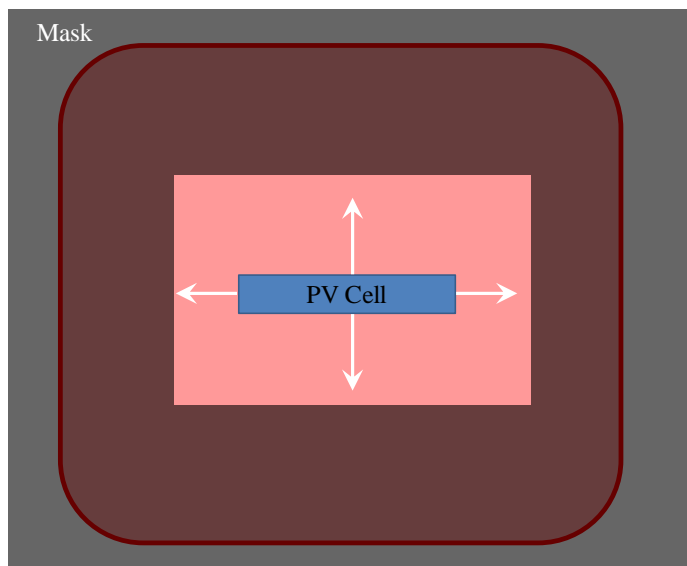


Figure 3.2 LSC masking experimental setup. A single PV cell place in a single large LSC panel with undesired areas masked off to prevent light entry.

3.3 Results and Discussion

3.3.1 Optical properties of the luminescent absorber

Lumogen Red 305 (LR305) was chosen as the LSC luminescent material due to its high quantum yield and stability in air [38]. Absorption (green curve) and PL emission (red curve) for LR305 embedded in PMMA are shown in Figure 3.3A. Clear PMMA was used as a base line scan for absorption spectroscopy. LR305 absorbs strongly below 400 nm and in the 500-600 nm range. Between 400-500 nm, absorption drops to an average value of 61% with a peak at 573 nm. The extinction coefficient at 573 nm was calculated to be 4.0×10^4 . For 437 nm excitation, the PL emission spectrum peaks at 611 nm and has a shoulder around 650 nm. Photon re-absorption in the LSC shifts the emission peak toward the 650 nm shoulder gradually

reducing the overlap between absorption and emission spectra, as shown in Figure 3.3B. The LR305 was embedded into a flexible acrylic sheet of 500 μm thickness in which it has a quantum yield of 85% (+/- 3%).

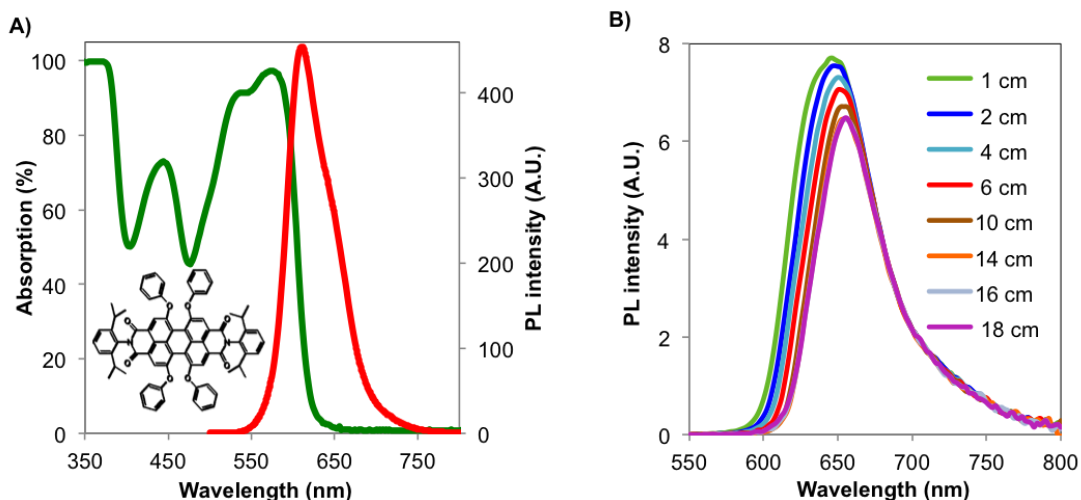


Figure 3.3 Steady state absorption and photoluminescence emission spectra for LR305 (top). Photoluminescence emission spectra of LR305 embedded in an acrylic sheet for increasing distances between excitation and detection (right). Inset: Molecular structure of LR305.

3.3.2 Optimization of LSC panel thickness and panel edge treatment

Several waveguide parameters can be adjusted to increase the amount of light collected by an attached PV cell, two of which are the waveguide thickness and its edge surface properties. Thicker waveguides reduce re-absorption losses but increase the likelihood of photons passing over the PV cell uncollected. The effect is reversed for thinner waveguides. In addition, a waveguide that is too thin will cause the majority of trapped photons to be directed to the edges of the PV cell, leaving the middle unenhanced by the LSC. Hence waveguide thickness and PV cell size must be

properly matched. Acrylic sheet waveguides, 30.5 cm x 30.5 cm, of 4 different thicknesses, 1/16" (0.159 cm), 1/8" (0.318 cm), 3/16" (0.476 cm), and 1/4" (0.635 cm), were used to construct LSC panels and the power output of a 1 cm wide PV cell on each window was tested. For this cell dimension, the 3/16" (0.476 cm) thick acrylic was found to provide the highest power output, and all designs thereafter were based on this thickness.

Next the effect of the waveguide edge on performance was investigated. With rough untreated edges, the probability of trapped light refracting out of the waveguide at the edge is high. Treating the edge to increase reflectivity so that trapped light will not escape at the edges of the panel was used to increase the amount of light collected by the PV cell. Ideally, a surface that is 100% reflective would be engineered to completely remove this mode of loss.

To test the impact of the edge treatment, two 22.8 cm x 22.8 cm LSC windows were constructed. Each window had one 1 cm x 12.5 cm PV cell placed in the center. One had the edges fire-polished to create a smooth vertical wall and the other was left untreated. The surface was further modified in each experiment by coating the edges with black tape, silver-colored reflective tape or left unmodified. The power output was measured for each case and is shown in Table 3.1. In line with expectation, black coating on both panels gave the same power output since all wave-guided light reaching the edge would be absorbed. This was used as a check to ensure that both panels had the same starting conditions. The fire-polished panel showed an increase in power of 4% over the rough edge panel, both with and without reflective coating.

Fire-polish treatment was again applied to a more complex Tic-Tac-Toe window (described below) but showed no significant improvement. This treatment being both time-consuming and costly was discontinued. The addition of a reflective coating increased power output by 11% compared to uncoated edges in both the rough and fire-polished panels. On the masking panel, Figure 3.2, the addition of reflective coating resulted in a 12% increase in power. All subsequent demos had the edge treated with reflective coating.

Edge coating	Power (W)	
	Rough	Fire polished
Reflective	0.470	0.489
None	0.423	0.441
Black	0.378	0.378

Table 3.1 Power output for various acrylic edge treatments.

3.3.3 LSC panel optimization: design projections and effect of PV cell

The next parameter investigated was the gain as a function of the LSC area exposed around the PV cell. A larger LSC area collects more light and concentrates it onto the PV cell, thus increasing its gain. At the same time, a larger proportion of that wave-guided light experience longer mean distance to collection by the PV cell, incurring losses along the way and dropping the increase in gain per area. Masking results for 2 cm PV cell, as seen in Figure 3.4, show that the gain per area LSC plummets significantly from 2 to 6 cm of LSC exposed around the cell and flattens

out as photon re-absorption decreases resulting from the increased red-shift of emission that occurs with distance in the waveguide (Figure 3.3B).

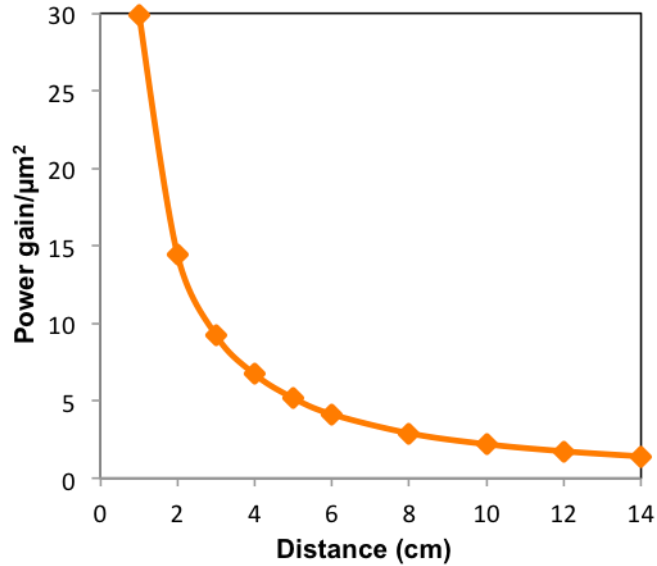


Figure 3.4 Power gain per area for increasing distances of exposed LSC material to PV cell.

It was also observed that LSC material placed along the long edge of the PV cell (Figure 3.5B) contributes a greater gain per area than LSC along the narrow edge of the PV cell (Figure 3.5A). This can be seen from Figure 3.5, where the square mask experiment demonstrates slightly better gain compared to rectangular mask. The rectangular mask traces the shape of the PV cell and adds an equal amount of LSC around the edges as the mask is pulled back. The square mask follows the panel shape and as the mask is withdrawn, it preferentially adds more LSC area on the long edge of the PV cell for the same total LSC area. As seen in Figure 3.5(inset), a dye molecule emitting photons isotropically located at the long-edge of the PV cell will emit photons to be absorbed by the cell over a larger angle than one located the same

distance from the short edge of the cell. Therefore, LSC adjacent to the long-edge emits light that has a higher probability of being wave-guided to the PV cell than LSC along the short-edge, providing a greater contribution to the gain.

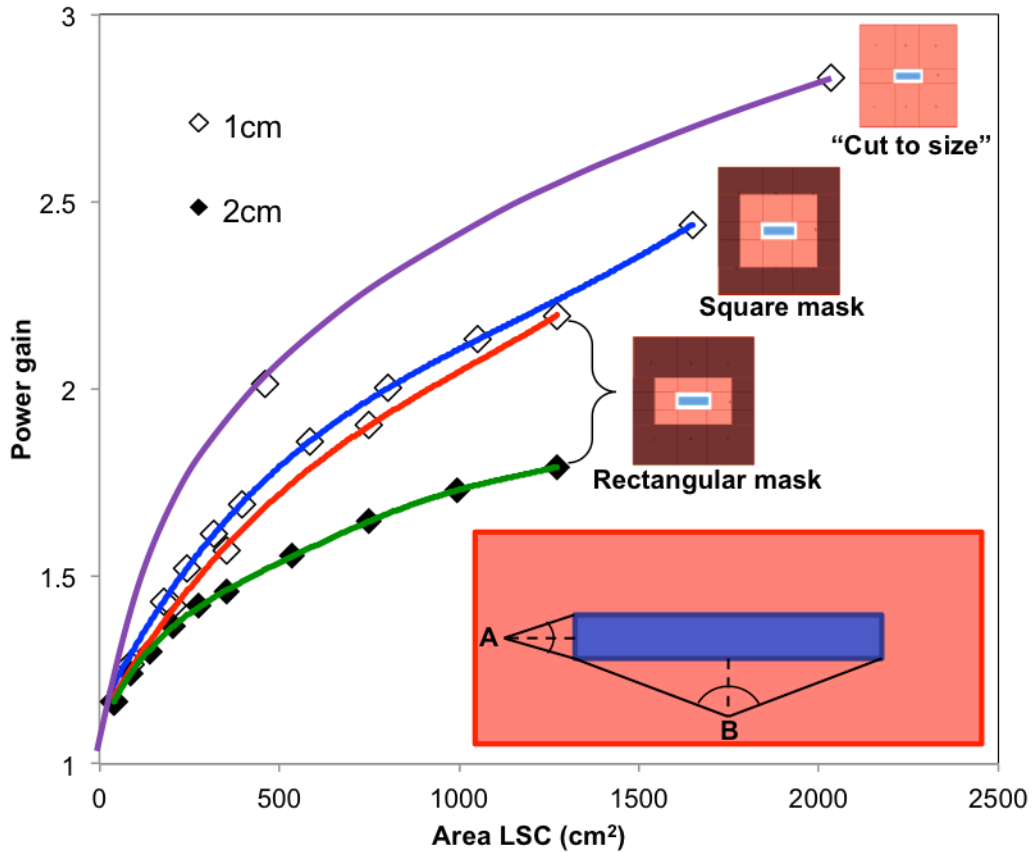


Figure 3.5 Power gain as a function of LSC area surrounding a PV cell in masking experiments and “cut-to-size” windows. Inset: Schematic illustrating that LSC exposed on the long-edge of the PV cell contributes greater power gain than the LSC on the short-edge of the cell. All PV cells have dimensions 12.5 x 1cm or 12.5 x 2cm.

From Figure 3.5, there is a discernible difference in the gain obtained from masking and from LSC panels cut to the same dimension as the mask (labeled as “cut to size”). The masking experiments consistently underestimate the level of actual gain.

This is largely due to additional losses experienced by wave-guided light traveling underneath the mask to the panel edges before being reflected back, instead of doing so at the mask edge as a “cut to size” panel would. As mentioned throughout this paper, longer distances spent in the panel increases the probability of photon of re-absorption or scattering. This discrepancy between masked and “cut-to-size” is factored into our measured masking data accordingly for our design projections in Figure 3.6, labeled as “corrected”.

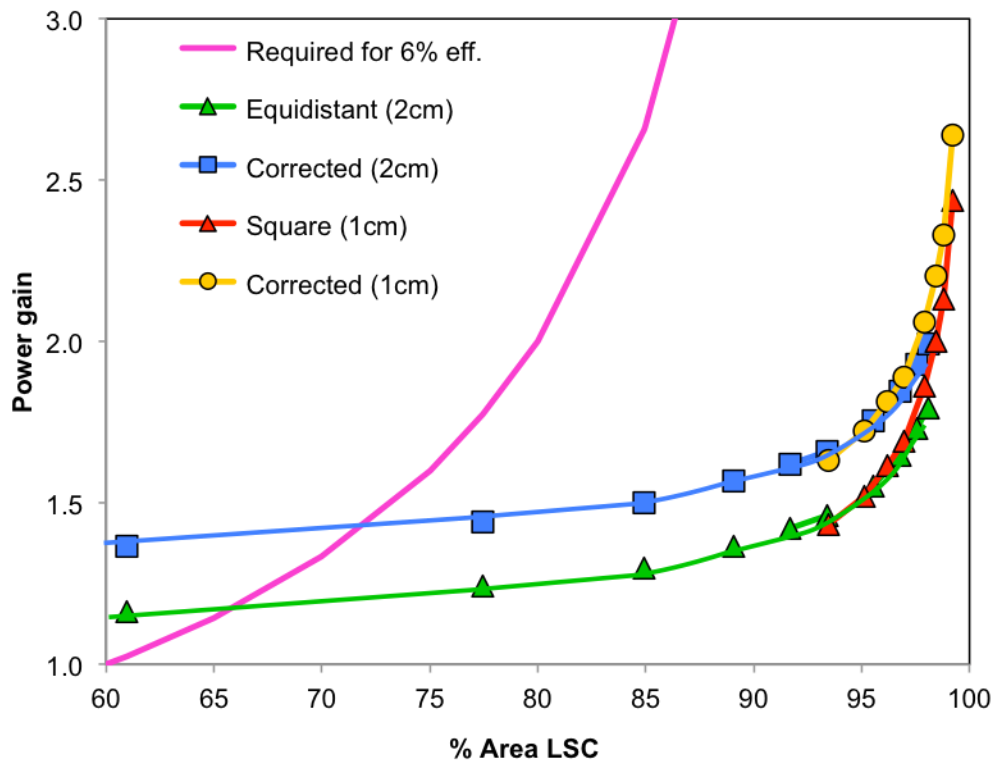


Figure 3.6 Power gain as a function of percentage LSC area. The projection line (purple) calculates the LSC panel gain required for the overall panel conversion efficiency to hit 6% with the ratio of PV cells used for a given area. In this graph, the PV cells were assumed to have 18% power conversion efficiency

Plotting the gain against the percentage area of LSC coverage, we were able to make projections of the area ratio needed to produce panels of a desired efficiency or gain. In Figure 3.6, the projection line (purple) calculates at each percentage area occupied by PV cells, the additional gain that the panel needs to generate in order for the overall panel power conversion efficiency to hit 6%. Projections were calculated assuming the PV cells had 18% efficiency. For high gain, we estimated from Figure 3.6 that a 98-98.5% LSC coverage would yield a gain of 2x. Similarly for high power efficiency, approximately 72-77% LSC coverage would produce a window power conversion efficiency of 6%. Based on these projections, demos were constructed to attain each individual goal. There exists a tradeoff between power efficiency and gain. To achieve a high gain requires a much higher ratio of LSC, which lowers the power conversion efficiency of the LSC window. The converse is also true for the high efficiency panel. To attain both targets simultaneously necessitates improving the gain beyond ratio adjustments. This led us to explore further the effect of cell placement on the gain and power output. Several different designs were constructed and are discussed in section 3.3.4.

In the masking experiments, the 2 cm PV cell had much lower gain per LSC area exposed compared to the 1 cm PV cell on the same setup, as seen in Figure 3.5. One possible reason is that the ratio of LSC area to PV cell area is halved for the 2 cm cell. Normalizing the plot in Figure 3.5 to percentage LSC area, Figure 3.6, yielded a much better correlation between the two curves, but the question still arises, which width of cell, 1 cm or 2 cm, would lead to the optimal design? Two 1 cm cells would

compose a design with a greater amount of LSC directly adjacent to the cells, allowing photons to be collected after traveling a shorter distance in the LSC. One 2 cm cell though yields a more compact design allowing more energy conversion. To satisfy this query, three new panels were constructed for 1 cm and 2 cm cells keeping the PV to LSC ratio the same as shown in Figure 3.7. An 18 cm x 18 cm panel was constructed with one 1 cm by 12.5 cm cell in the center. Two 25.3 cm x 25.3 cm panels were constructed, one with one 2 cm x 12.5 cm cell in the center, and one with two equally spaced 1 cm x 12.5 cm cells.

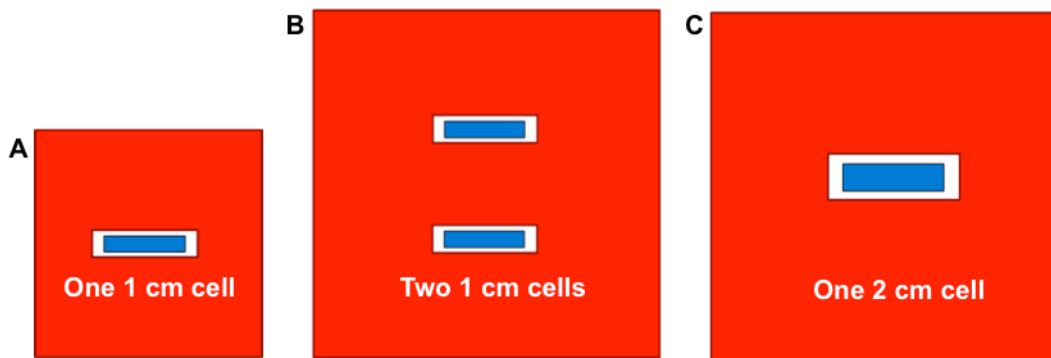


Figure 3.7 Cell width demos. A: panel with one 1 cm wide PV cell; B: panel with two 1 cm wide PV cells; C: panel with one 2 cm wide PV cell.

The output power shown in Table 3.2 was normalized between the cells since the width of the 1 cm cell (0.96 cm) was not in fact half that of the 2cm cell (1.8 cm), and both dimension of cells had different fill factors. After normalizing, the power output and gain of the single 1 cm and 2 cm panels (Figure 3.7A and 6C) were found to be similar, indicating little difference in performance. Of greater interest is the better gain and normalized power seen in the two 1 cm panel (Figure 3.7B) compared to the

2 cm panel, as a result of a change in cell placement. Redistributing the PV area permits wave-guided photons a shorter traveling distance before being collected by the cell. However, cutting the PV cells to size introduces defects into the crystal structure, which act as current shunting pathways that lower the fill factor and output current of the cell. Hence, cutting the cells into smaller pieces is only justified if this loss is more than compensated by an increase in gain through optimized cell layout and panel dimensions. The comparison of 1 cm and 2 cm cells was further explored by constructing more complex windows of identical design using both types of cells, as explained in the following section and shown in Figure 3.9.

Panel	Cell area (cm ²)	Power (W)*	Norm. power (W)**	Power gain
One 1cm cell	12	0.360	0.674	1.9
Two 1cm cells	24	0.777	0.728	2.0
One 2cm cell	22.5	0.699	0.699	1.8

* 1cm fill factor is 0.679, 2cm fill factor is 0.723

** Normalized by cell area

Table 3.2Power output and power gain for cell width demos in Figure 3.7.

3.3.4 LSC window demos

In analyzing the efficiency and gain in the different designs, measurements were taken under three conditions, which yielded varied results. Figure 3.8 depicts the three ways measurements were taken: with a flash tester (Sinton Instruments), outside with the window lying flat, and outside with the window tilted normal to the sunrays; Table 3.3 exemplifies the differences in measurements for the High Power Efficiency window, described below.

Light incident on the LSC at an angle greater than 90° increases the path length of light in the LSC thereby increasing the absorption by the dye and hence the gain. Additionally, the PV cell's efficiency is dependent on the angle of incidence. Best efficiencies are obtained with light at normal incidence and deteriorate with increasing angles as seen in Table 3.3. Taken together, angled light on the LSC window (resulting from taking measurements with the panel lying flat) favors higher gain due to a slightly greater contribution from the LSC and significantly poorer power contribution from the PV cell.

Flash testing involves illuminating the panel with a short burst of simulated sunlight. This prevents the PV cells from heating up and thus yields a higher measured V_{oc} compared to outdoor measurements, and hence a higher cell efficiency. As seen in Table 3.3, the gain of the panel when flash tested was approximately the same as the tilted measurements but with higher efficiencies recorded.

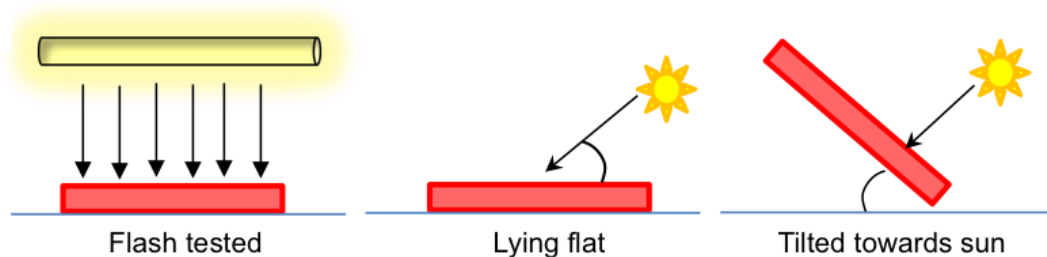


Figure 3.8 Different testing methods: (1) flash tester; (2) outside with demo lying flat; (3) outside with demo tilted towards the sun.

Method	Power gain	Ref. cell efficiency (%)	Panel efficiency (%)
Flash	1.2	19.8	6.8
Flat	1.4	15.5	6.2
Tilted	1.2	18.4	6.6

Table 3.3 Summary of variations in power gain and efficiency for different testing methods.

Gain for the panels measured outdoors was somewhat variable and depended on the month and time of the day measurements were taken. This was largely due to the changes in the angle of the sun. To the best of our abilities, we took outdoor measurements within the same 2-3 hour time slot each day but could not correct for monthly variations in the sun's angle or variation of the sun's intensity. As such, an objective comparison between panels can only be carried out with the flash test data as reported in Table 3.4. Since angled light produces a greater contribution from the luminescent dye, panels with high LSC coverage would exhibit significantly smaller gain with the flash tester compared to outdoors.

Demo	Panel area (cm ²)	Cell coverage	Panel efficiency	Power gain
High Power Eff.	1011	31%	6.8%	1.2
Zig Zag 1cm	2581	15%	3.7%	1.6
Zig Zag 2cm	2581	14%	3.8%	1.6
Tic Tac Toe*	2088	10%	---	1.6
High Power Gain*	2088	5%	---	1.8

*Efficiencies are not comparable to other demos because of difference in cell type

Table 3.4 LSC window performance summary. Power gain and panel efficiency measured with flash tester.

A High Gain window was built to have a gain of 2x with 95% LSC coverage on a 45.7 cm x 45.7 cm panel. Six 1 cm x 15.5 cm PV cells (Evergreen Solar) were arranged in three rows of two, equidistant from each other and the panel edges, as shown in Figure 3.9A. Less LSC coverage was used than projected due to expected improvements in performance from cell placement and additional reflected light from the closer proximity of the window edges to the cells.

The window was tested outdoors lying flat and attained a gain of 2.2x. Adding a white reflective background returned a portion of the transmitted and escaped light to the window and raised gain further to 2.4x. Flash testing with light entering normal to the panel surface gave a lower gain of 1.8x. Power efficiency cannot be accurately compared to other window designs because a different PV cell type was used.

A High Power Efficiency demo, targeted to have a power conversion efficiency of 6%, was built with 69% LSC coverage on a 31.8 cm x 31.8 cm panel. Twelve 2 cm x 12.5 cm PV cells were arranged in six rows of two, equidistant from each other and the edges, as shown in Figure 3.9B. Data taken with the panel lying flat attained a power conversion efficiency of 6.2%, with a gain approaching 1.4x. A maximum panel efficiency of 6.8% was obtained with flash testing. Results are summarized in Table 3.3.

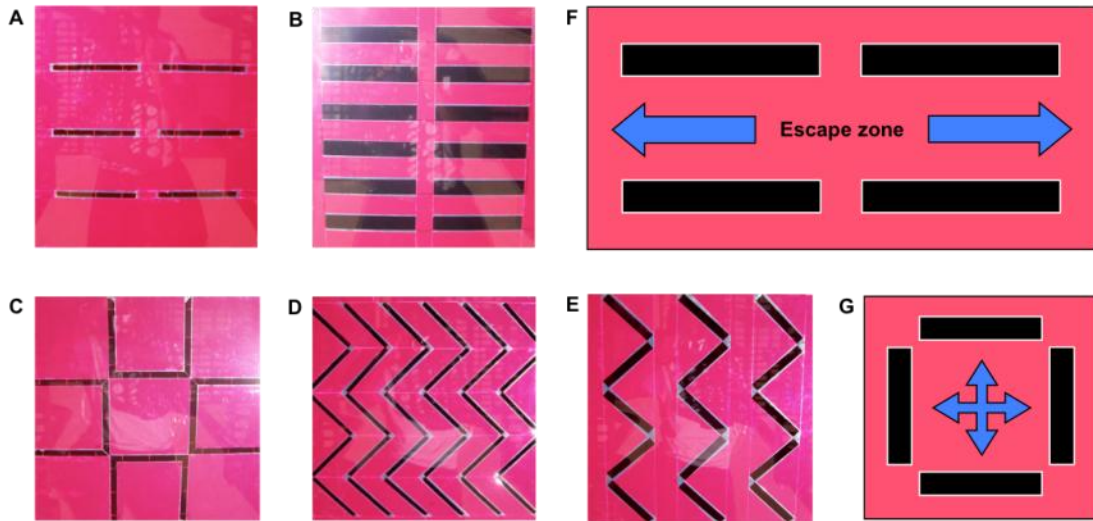


Figure 3.9 Design of LSC windows. A: 2x power gain; B: 6% panel efficiency; C: Tic-Tac-Toe; D: 1 cm Zig-Zag; E: 2 cm Zig-Zag. Sample layouts showing potential escape zones (F) and superior light trapping (G).

In the above two designs, we see many large zones that light can potentially travel and reflect multiple times without ever hitting a PV cell as illustrated in Figure 3.9F. While photons may eventually scatter in a favorable direction, the likelihood of the photon being lost increases with distance travelled after the initial absorption event. A better design reduces these escape zones and increases the amount of light collected as shown in Figure 3.9G.

To find a balance between gain and panel efficiency, two demos with a “Tic-Tac-Toe” pattern were built with 90% LSC coverage on 45.7 cm x 45.7 cm panels. Twelve trapezoidal 15 cm x 12.5 cm x 1.2 cm PV cells (Evergreen Solar) were arranged in a Tic-Tac-Toe formation as shown in Figure 3.9C. One Tic-Tac-Toe window was created on an acrylic panel with fire-polished edges and one Tic-Tac-

Toe window was created on an acrylic panel with rough (untreated) edges. Reflective coating was applied to the edges of both demos.

This design was projected to have a gain of 1.6x based on the masking experiments but attained a factor of 1.8x outdoors. The design was chosen to better capture light radiating isotropically in the LSC material. The panel power efficiency cannot be compared to the other demos due to a difference in PV cell type used. No difference was observed between the panels with fire-polished edges versus the one with rough edges. Fire-polishing acrylic edges appear to have no effect on power output and gain in this design.

To further improve light trapping, a Zig-Zag pattern was constructed next. Two Zig-Zag demos with different cell widths were built on 50.8 cm x 50.8 cm acrylic panels, as shown in Figure 3.9D and E, and were designed to have the same LSC coverage. One panel was built with 15 – 2 cm PV cells and the other was built with 30 – 1 cm PV cells. Inaccuracy in dicing resulted in actual cell widths of 1.8 cm and 0.96 cm respectively, giving both panels slightly different cell coverage than intended.

The 1 cm and 2 cm Zig-Zag demos had a LSC coverage of 85% and 86% respectively. The demos attained gains of 1.4x and 1.5x when tested outdoors, against a projected gain of 1.5x. Construction of the Zig-Zag design was much more complicated than any of the previous panels, resulting in many defects, especially in the seams where LSC pieces were joined. The additional scattering could have adversely affected the panel performance. This drawback might be overcome by laminating the LSC directly over the cells in future iterations. Panel conversion

efficiency was calculated using power output measurements taken with a flash tester. The 1 cm Zig-Zag demo reached a panel conversion efficiency of 3.7% and the 2 cm Zig-Zag demo reached 3.8% efficiency.

Table 3.4 provides a summary of the dimensions and performance of all windows/panels constructed.

3.3.5 Cost per watt optimization

The ultimate objective of this project is to reduce the added cost per watt of solar electricity by incorporating solar cells into a window. In that respect, pushing for high efficiency or high gain does not result in the lowest cost as seen in Table 3.5. The tradeoff between gain and high energy-conversion efficiency is non-linear and a design with the best compromise of these design factors, which in our case is the 2 cm Zig-Zag panel, achieves the lowest cost. Further improvements can be expected by further increasing the gain while maintaining the same coverage. The ongoing goal of removing as many loss mechanisms as possible is in future works.

Demo	Cell coverage	\$/watt**
High Power Eff.	31%	\$1.77
Zig Zag 1cm	15%	\$1.64
Zig Zag 2cm	14%	\$1.52
Tic Tac Toe*	10%	\$1.65
High Power Gain*	5%	\$2.29

*Power calculated with 0.7 fill factor in order to compare \$/watt with demos using Sun Power PV cells.

**Calculated based on Sun Power PV cost of \$380/m² and LSC material cost of \$10/m²

Table 3.5 Cost per watt for all demos. The right-most column was calculated with \$1.90/W (Sun Power cells) converted to cost/m² for 20% efficient cells.

3.4 Conclusion

Front facing PV cells allow us flexibility in designing LSC windows with varied cell coverage and cell placement. The relationship of the gain as a function of LSC exposed in the masking experiments shows a non-linear relationship between gain per unit area and panel efficiency. From the results, we obtained estimates on the minimum coverage needed for each design and noted that area on the short edges of the cell can be sacrificed with minimal impact to performance. These considerations were later incorporated into our cell placement strategies. Cost analysis indicates, contrary to initial expectations, pursuing a high gain at the expense of efficiency resulted in an overall higher cost per watt, even though the LSC material itself was inexpensive. Due to the non-linear tradeoff between gain and efficiency, our demos show that cell coverage of 14% yielded the lowest cost. Analysis of existing windows shows many light loss mechanisms that can still be addressed and future work will be geared towards increasing the absorption spectrum of the LSC and reducing re-absorption losses.

4 Monte-Carlo Ray-Tracing Simulation

Model for LSCs

4.1 Introduction

From the previous chapter, the challenges in trying to design and optimize LSC panels empirically are not trivial. A multitude of environmental and human factors serve to obscure the collected data making comparisons in LSC panel performance difficult and inaccurate at times. Trying to tune the many optical and material parameters experimentally is an exercise in futility not to mention costly, very time consuming and often does not provide an adequate understanding of the physical parameters involved. To that end, I have developed a ray tracing simulation[39], [40] based on the Monte Carlo method[37], [41]–[47], incorporating the measured absorption/emission spectra of the luminescent material dispersed in thin acrylic, and the background scattering effects of acrylic.

The model parameters used to simulate benchmarking data are based on our initial experiments from chapter 3 using LR305 absorbers, an acrylic matrix and commercial PV cells, thus fixing the values of, η_{PE} , η_{PL} , η_{abs} , η_{DC} and η_{MPE} but the model retains flexibility in allowing any of the parameters in the efficiency equation (3.2) to change. This will allow us to investigate different dye concentrations, other types of luminescent particles, matrix material and PV cells to be used in future works. Dye

concentration alters the absorption (η_{abs}) and photoluminescence efficiency (η_{PL}), with higher concentrations improving absorption but also leading to PL quenching due to dye aggregation. Reabsorption loss is also adversely affected by high concentration when significant overlap exists between the absorption and emission spectra of the dye. This is further complicated by structural requirements with flexible panels needing thin, high concentration absorber layers and vice versa for thick panels.

Replicating the experimental setups leaves the LSC to PV cell area ratio and remaining efficiency variables as design parameters to be determined. Waveguide efficiency (η_{WG}) is comprised of many factors including waveguide surface conditions, embedded scattering centres, its refractive index, and owing to the forward facing PV cell design, matching between the waveguide thickness and PV cell dimension. The LSC to PV ratio will be determined by a tradeoff between the power conversion efficiency, cost per watt desired, concentration factor, and re-absorption losses.

The ray tracing model was built in two parts, starting first with a 2-dimensional (2D) model which was later expanded upon and reconfigured into 3-dimensions (3D). Explanations of both 2D and 3D models have been included. Results are drawn from both 2D and 3D simulation. Insofar as benchmarking with earlier experimental data is concerned, both 2D and 3D simulation results are closely correlated and strongly

parallels experimental data permitting detailed study of the distribution of photons and various loss mechanisms present in the LSC panel.

In section 4.2 the workings of the ray tracing program are explained. The analysis of several LSC panel simulations, comparisons with experimental data and the implications on the panel design follows in section 4.3. The various loss modes present in the LSC are also examined. Finally section 4.5 summarizes the work and conclusion.

4.2 Weighted Monte-Carlo Ray Tracing Simulation

Ray-tracing has often been used to model optical systems in many applications, particularly where wave effects can be ignored. Monte Carlo Ray-tracing models for LSCs while not as fast as thermodynamic models[48]–[50], is a less complex and hence an easier model to implement. It affords greater flexibility in altering the panel dimensions and multiple physical effects included in the model. The LSC model consists of layered planar structures divided into several regions as shown in Figure 4.1A single layer of acrylic forms the top of the panel. The second layer is broken into regions of thin acrylic infused with LR305, interspaced by PV cells. Because the PV cells are much thinner than the surrounding luminescent layer, an air gap is added below each PV cell in the model to make up the difference and account for the rare occurrence when photons travel beneath the PV cell. Rectangular boxes are used

initially to simplify analysis, but the program is able to handle non-rectangular dimensions and can simulate any number of additional layers.

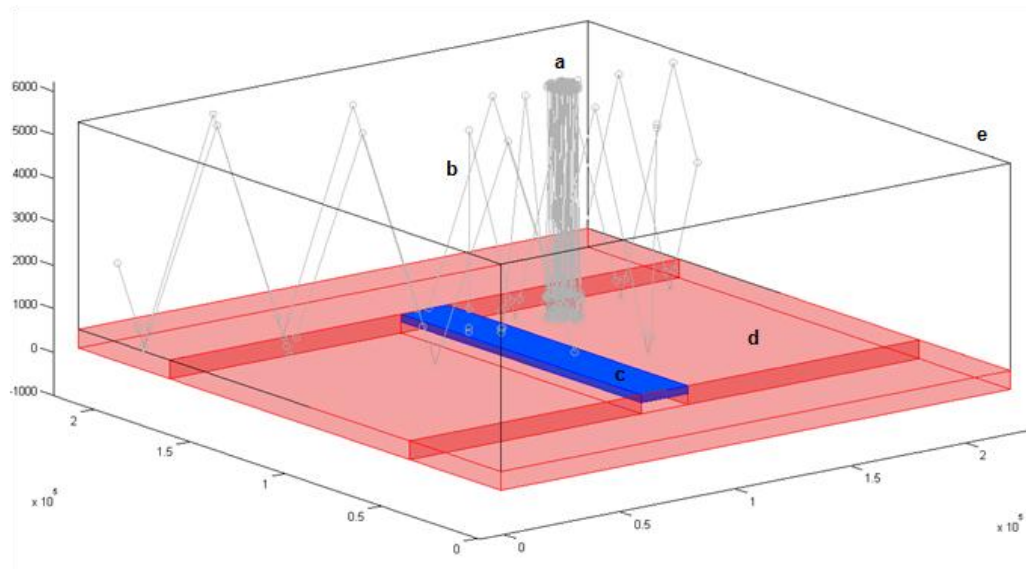
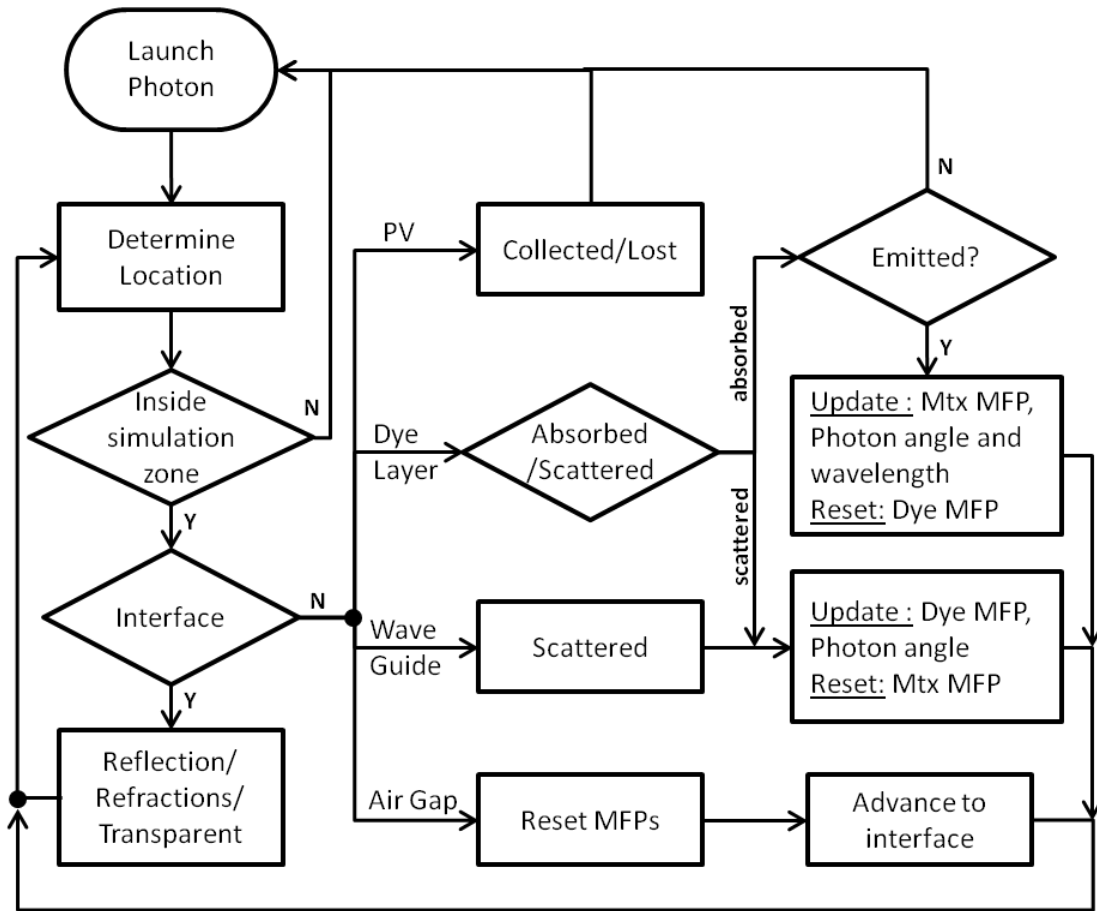


Figure 4.1 Schematic of the LSC panel with 100 incident photons. a: Incident photon; b: Wave-guided photon; c: PV cell; d: Luminescent layer; e: Waveguide

The ray-tracing program follows the path of each individual photon launched at the LSC panel, tracking its position and interaction within the panel until termination, either via collection by a PV cell or lost through non-radiative absorption and escape trajectories. The path and interactions of a photon is strongly influenced by its wavelength. Solar radiation is non-uniform in its wavelength distribution and is dependent on a number of factors such as geographical location, time of day, season and prevailing weather conditions. A Weighted Monte Carlo algorithm[51]–[53] is employed to incorporate this biased probability into the determination of photon outcomes. The initial wavelength of illuminating photons is randomly selected but

skewed in its distribution to replicate the AM 1.5 solar spectrum over a large number of samples. To adequately reproduce the spectrum and obtain statistically reliable results, a minimum of 10^5 photons were simulated in each run. The photon can be assigned an initial fixed or random direction representing focused and diffused illumination respectively. The starting position on the LSC top surface is randomly determined and can be made to be distributed evenly over the entire panel surface or concentrated in any desired region.

Figure 4.2 depicts the ray-tracing simulation algorithm. In summary, based on the photons current location and simulation parameters, the event (absorption, scattering, interface interaction, collection, loss) that is first encountered along the photon's direction is determined; this gives the path length travelled and hence the new photon location. Event specific interactions are evaluated updating the simulation parameters and the photon's current state. In accordance with the Monte Carlo method, outcomes of photon interaction with interface boundaries, luminescent particles and scattering centers are determined by comparing calculated probabilities with randomly generated numbers. At the PV cell, a photon is deemed to have been successfully collected when it strikes the top of the cell from above. Any other approach or position hit is recorded as a loss. Collected photons are further categorized into those with and without sufficient energy to generate photocurrent. Only current generating photons are counted towards γ_{pwr} calculations.



Mtx MFP = Photon Mean Free Path in Matrix
 Dye MFP = Photon Mean Free Path in Dye

Figure 4.2 Ray-tracing algorithm flow chart. The simulation is broken up into several distinct mutually exclusive interactions, namely the interface and layer effects on the photon. Determining the photon location applies the appropriate action for each iteration.

4.2.1 Photon localization

The prevailing effects acting on the photon depend on its locale. Localization is carried out by simultaneously comparing the photon's current coordinates with the boundary of every region in the simulation zone. To cover a multitude of conditions, two localization tests[54], [55] (line intersection and point-in-box) are applied. Each

test identifies a set containing one or more regions in which the photon might reside in. Both sets intersect at only one region which always produces the correct outcome.

4.2.1.1 Line intersection test

In 2D simulations, the light ray and the interface vectors are each defined by a point plus a direction vector

$$\text{Light Ray: } Q(r) = Q_0 + r\vec{v}, \quad \text{Interface: } P(s) = P_0 + s\vec{u} \quad (4.1)$$

By setting \vec{v} and \vec{u} to the mean-free-path and length of the interface respectively, we can determine a result from the sign and magnitude of r and s . A successful ray-interface intersection occurs when the ray is projected to cross the interface in front of the ray ($r > 0$) and within the length of the interface ($0 \leq s \leq 1$). If intersection occurs at a distance longer than the mean-free-path ($r \geq 1$), then an absorption or scattering event flag is raised.

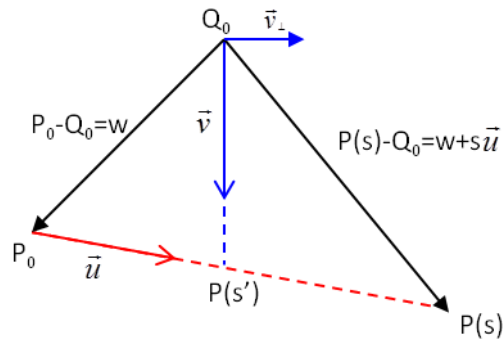


Figure 4.3 Vector diagram illustrating the line intersection test. \vec{u} and \vec{v} are the unit vectors of each line. w is a vector joining the points of origin for each line and $P(s)$ the point of intersection.

From the vector diagram (Figure 4.3), we have at the point of intersection:

$$P(s') - Q_0 = w + s'\vec{u} = r\vec{v} \quad (4.2)$$

Since $r\vec{v}$ is perpendicular to \vec{v}_\perp : $\vec{v}_\perp \cdot (w + s'\vec{u}) = 0$

Rearranging to solve for s' :

$$s' = \frac{-\vec{v}_\perp \cdot w}{\vec{v}_\perp \cdot \vec{u}} = \frac{v_y w_x - v_x w_y}{v_x u_y - v_y u_x} \quad (4.3)$$

Similarly for r , we have $s\vec{u}$ is perpendicular to \vec{u}_\perp , hence $\vec{u}_\perp \cdot (-w + r'\vec{v}) = 0$

$$r' = \frac{\vec{u}_\perp \cdot w}{\vec{u}_\perp \cdot \vec{v}} = \frac{u_x w_y - u_y w_x}{u_x v_y - u_y v_x} \quad (4.4)$$

By projecting the photon's path from its current location and examining the intersections it makes with the boundary of the region, we can determine if the photon is currently inside or outside the region. In the majority of circumstances, if the defined region is a convex polygon, a light ray originating from within will intersect with only one interface of the region. For a concave polygon, multiple boundary intersection can occur. An odd number of interface intersections indicate that a photon is within the region. One drawback is that this test is unable to discriminate the photon's position accurately when the photon is projected to intersect with one or more vertices of the actual region it is residing in. Vertex intersection creates two or more positive boundary intersections within the correct region which is indistinguishable from multiple intersections in other outside regions.

The 3D intersection test is slightly more complex, with an additional test, but otherwise has the same pass criteria as the 2D line intersection test. The ray-plane intersection point is calculated again using vector geometry.

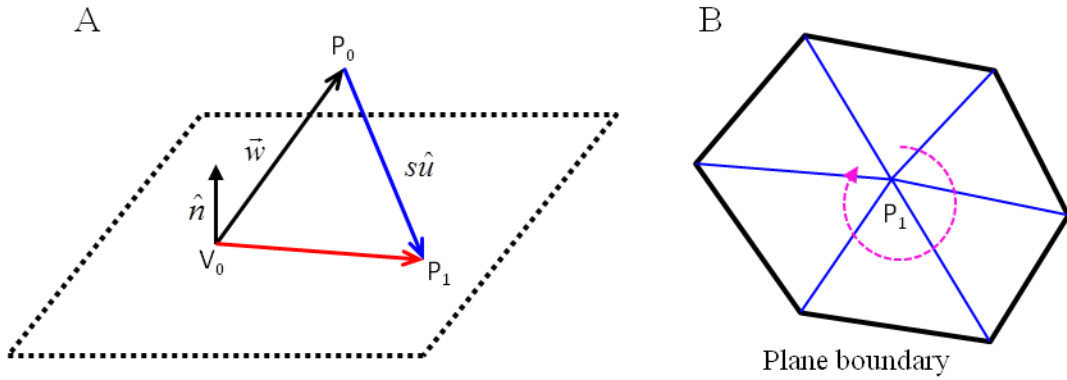


Figure 4.4 Vector diagram illustration ray-plane intersection (A) and sum of angles test (B)

With reference to Figure 4.4A, V_0 is any point on the plane, \hat{n} is the unit normal vector of the plane, P_0 is the photon's current position, P_1 is the point of intersection with the plane, \hat{u} is the unit direction vector of the photon and s is a scalar multiple. If P_1 is on the plane then the vector $(P_1 - V_0)$ is perpendicular to \hat{n} and their dot product gives zero.

$$\hat{n} \cdot (P_1 - V_0) = \hat{n} \cdot (\vec{w} + (P_1 - P_0)) = 0 \quad (4.5)$$

Expanding on the term and rearranging, we can calculate a value for s .

$$\hat{n} \cdot (P_0 - V_0) + s(\hat{n} \cdot \hat{u}) = 0 \quad \rightarrow \quad s = \frac{\hat{n} \cdot (V_0 - P_0)}{\hat{n} \cdot \hat{u}} \quad (4.6)$$

The value of s indicates the intersection direction with $s > 0$, $s = 0$ and $s < 0$ giving ray-plane intersection in the direction of \hat{u} , at P_0 and in the opposite direction of \hat{u} respectively. This by itself is insufficient to determine if the ray-plane intersection has occurred within the boundary of the defined region. With the intersection point P_1 calculated, if it falls within the region boundary, summing up angles created by subtending P_1 with two adjacent vertices of the plane, as illustrated in Figure 4.4B, would give a value of exactly 360° . A successful ray-plane intersection must satisfy the condition of $s \geq 0$ and P_1 within the region boundary.

4.2.1.2 Point-in-Box test

For a 2D simulation, this test uses the two-point method to describe a line. Each region in the simulation is delineated by a polygon which can be decomposed into a number of straight lines. Given two consecutive vertices, (x_1, y_1) and (x_2, y_2) , the line equation derived from the slope is given as:

$$\frac{y_2 - y_1}{x_2 - x_1} = \frac{y - y_1}{x - x_1} \xrightarrow{\text{rearrange}} (y_2 - y_1)x + (x_1 - x_2)y + y_1x_2 - x_1y_2 = 0 \quad (4.7)$$

Substituting the coordinates of the photon into the left hand side will yield a number indicating its position relative to the line, with zero being exactly on the line. A positive or negative number signifies that the photon is either on the right or left of the line, with respect to the line direction, depending on the order of the vertices used. Performing the tests in a clockwise direction, a photon is deemed to be within a region when it lies to the right of all lines that make up the region's boundary. A

limitation to this test occurs when the photon position is exactly on a boundary, in which all regions adjacent to that boundary would be marked as being positively identified.

With planes instead of lines in a 3D simulation model, the position of a point is determined by substituting the photon's position into the normal implicit equation of the plane (4.8)

$$\hat{n} \cdot (P_0 - V_0) = 0 \quad (4.8)$$

Evaluating the left side of the equation will yield a result revealing the position of P_0 relative to the plane, with < 0 , $=0$ and > 0 signifying that P_1 is below, on or above the plane respectively³. To determine if a point is inside the box, normal's for all planes bounding a region must all be defined uniformly pointing toward the interior or exterior of the region. Performing the evaluation for all planes should give the same sign or zero if the photon is inside the box. An example is shown in Figure 4.5.

³ Position is indicated by the direction of the normal with above the plane being in the same side as the normal direction

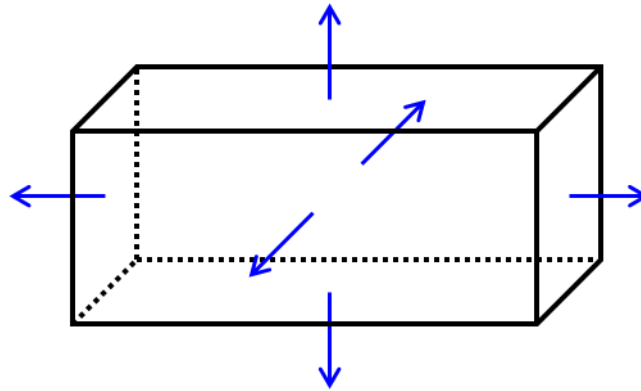


Figure 4.5 Definition of plane normal for all planes bounding a region of space

4.2.2 Interface interaction

In the algorithm, we consider three classes of interface that represents the possible boundary interactions in the LSC panel. The simplest class is a transparent interface, which represents the boundary between adjacent optically coupled regions. The photon is allowed to simply pass through with no additional effects. The next class is that of a reflective interface, where a photon undergoes a reversal in the direction normal to the reflective plane. This class can be configured to be partially absorbing by comparing the result from a random number generator and the probability of absorption. The last class of interface presents a refractive surface to the photon where the photon is either reflected or refracted.

Sunlight as received by the earth is unpolarised, but through scattering interactions with atmospheric constituents, undergoes some degree of polarization. The extent of polarization is related to the relative position of the sun's rays with

respect to the viewer and the composition of particles in the atmosphere. Polarization is greatest at an angle 90^0 from the direction of the rays and negligible in the parallel direction [56]–[58]. Solar panels are typically oriented south facing in the northern hemisphere to maximize daylight exposure and tilted to reduce the angle of incidence. With the large variability in polarization throughout the day and reduced angle of incidence during peak power generation, calculations in the model were simplified by assuming that all received solar illumination is unpolarised, thus we use the averaged reflection coefficient calculated using Fresnel's equation:

$$R = \left[\left(\frac{n_1 \cos \theta_1 - n_2 \cos \theta_2}{n_1 \cos \theta_1 + n_2 \cos \theta_2} \right)^2 + \left(\frac{n_1 \cos \theta_2 - n_2 \cos \theta_1}{n_1 \cos \theta_2 + n_2 \cos \theta_1} \right)^2 \right] \div 2 \quad (4.9)$$

where the subscripts 1 and 2 represent the incident and transmitted zones respectively.

Although the refractive index of acrylic varies slightly with wavelength[59], a fixed index of 1.491 is chosen for simplicity.

4.2.2.1 *Reflected and refracted ray calculations*

Calculating the reflected and refracted rays can be made easy and flexible by the use of vector geometry. Below I will describe a method that makes use of only the plane normal and the incident ray vector to calculate the reflected and refracted vectors. In this way, plane boundaries can take on all orientations in the simulation space allowing for the creation of regions with any polygonal shape.

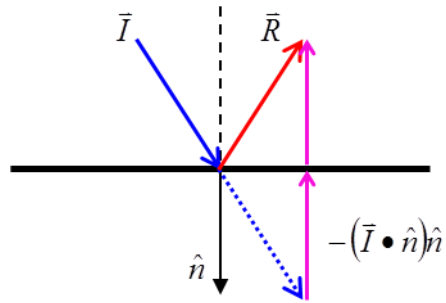


Figure 4.6 Vector diagram illustrating the calculation of a reflected ray vector from the incident ray vector and the plane normal unit vector.

From Figure 4.6, we can see that the reflected vector \vec{R} is obtained by a combination of the incident vector \vec{I} and its projection on to the normal vector \hat{n} .

$$\vec{R} = \vec{I} - 2(\vec{I} \cdot \hat{n})\hat{n} \quad (4.10)$$

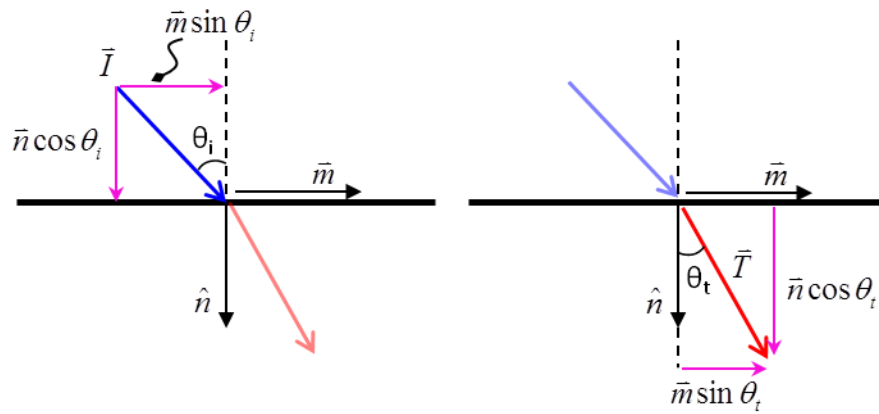


Figure 4.7 Vector diagram illustrating the calculation of a refracted ray vector using the incident ray vector and the plane normal unit vector.

Obtaining the refracted ray \vec{T} is a little more involved. We first recognize that a vector, \hat{m} , parallel to the plane can be obtained by resolving the incident vector \vec{I} .

$$\hat{m} = \frac{\vec{I} - \hat{n} \cos \theta_i}{\sin \theta_i} \quad (4.11)$$

We can then express \vec{T} as a combination of \hat{n} and \hat{m} . Substituting \hat{m} from Equation (4.11), we get:

$$\vec{T} = \hat{n} \cos \theta_t + (\vec{I} - \hat{n} \cos \theta_i) \frac{\sin \theta_t}{\sin \theta_i} \quad (4.12)$$

From Snell's law:

$$\frac{\sin \theta_t}{\sin \theta_i} = \frac{n_i}{n_t} = \eta_r \quad (4.13)$$

Putting Equations (4.13) into (4.12) and after further manipulation, we can express \vec{T} in terms of \vec{I} , \hat{n} and θ_i .

$$\vec{T} = \left[\sqrt{1 - \eta_r^2 (1 - \cos^2 \theta_i)} - \eta_r \cos \theta_i \right] \hat{n} + \vec{I} \eta_r \quad (4.14)$$

We can easily find $\cos \theta_i$ by taking the dot product of \vec{I} and \hat{n} reducing Equation (4.14) to only use \vec{I} and \hat{n} .

Absorption, emission and scattering

The acrylic waveguide has high optical transparency, but for large panels, trapped photons can travel long distances in the waveguide, thus matrix scattering should be considered. The mean-free-path (MFP) of a photon can be calculated from transmission measurements using the Beer-Lambert law given as:

$$MFP = \left| \frac{t}{\ln[T(\lambda)]} \right| \quad (4.15)$$

where t = thickness of sample and $T(\lambda)$ =transmission level measured for each wavelength.

The matrix (Mtx) MFP is substituted into the line intersection test described earlier to determine if a boundary collision or scattering event arises first. Scattering is assumed to be perfectly elastic and a new random direction is assigned to the photon. The Mtx MFP is tracked at all times and should other events precede scattering, the distance travelled is subtracted from the current MFP and reused in the next iteration. Whenever the photon leaves the acrylic matrix (eg. refracts into the air gap), the Mtx MFP is reset to its maximum value as determined by (4.15).

Luminescent particles in the dye layer act as a second scattering center overlying the acrylic matrix. As the two scattering/absorption events are considered independently, a second mean-free-path is introduced for the dye (Dye MFP) calculated using the absorption spectrum measured (Figure 3.3A). Spectrometer (N&K UV-vis) readings were taken, with a clear acrylic sheet of the same thickness

acting as the baseline; hence the results obtained are purely attributed to the LR305 dye. The two MFPs are compared at each iteration, with the smaller value substituted into the intersection test. The Dye MFP is tracked and updated similarly to Mtx MFP; whenever the photon leaves the dye layer, Dye MFP is reset. This can be extended to include more than one luminescent particle or scattering centers to model a multi-dye LSC or one infused with nano-particles.

The measured quantum efficiency of LR305 in acrylic is 85%[35]. A random number is compared against this figure to determine if photon re-emission occurs. Emission is assumed to be isotropic and a random angle is assigned. Emission wavelength selection follows the same weighted algorithm as the initial photon and has its distribution weighted to the photoluminescence spectra (Figure 3.3A) measured (LS-45 Perkin Elmer spectrometer).

4.3 Simulation Results

An array containing the vertex coordinates of all regions in the LSC model is provided as input. The initial photon angle can either be defined or randomly selected. The number of PV cells, their position and the number of layers can all be varied to model a number of different LSC panel designs. To obtain a qualitative feel on the behavior of photons in the LSC panel, the photon trajectories can be plotted and viewed. Figure 4.8 shows the visualization of a LSC panel with two PV cells; each event encountered by the photon can be clearly distinguished.

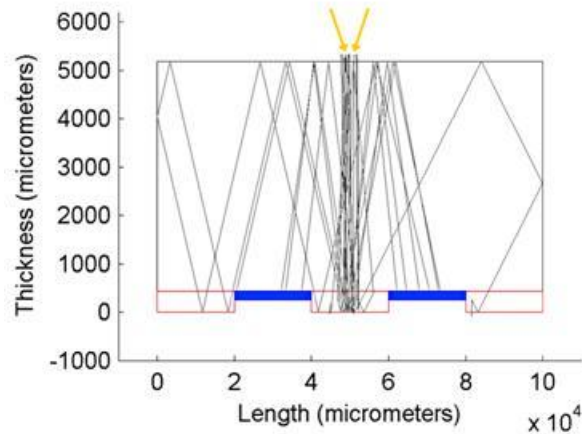


Figure 4.8 Visualization of simulated wave-guided rays in the LSC panel with an incident spot size of 5mm and an entry angle

4.3.1 Waveguide thickness and cell dimensions

For trapped photons in the waveguide, the horizontal distance traversed in plane is determined by the waveguide thickness and given as:

$$\Delta x = h \tan \theta \quad (4.16)$$

where h is the waveguide thickness and θ is the photon direction with respect to the plane normal. Thicker waveguides help suppress re-absorption by allowing photons a longer travel path in the dye-free waveguide. The design objective for LSCs is to channel photons to the PV cell with minimal re-absorption. For front mounted PV cells, a situation arises in which there exists an ideal waveguide thickness for each PV cell dimension. As illustrated in Figure 4.9, waveguides that are too thick or thin increase the number of reflections, and thus interactions a photon endures with the luminescent layer before striking the PV cell.

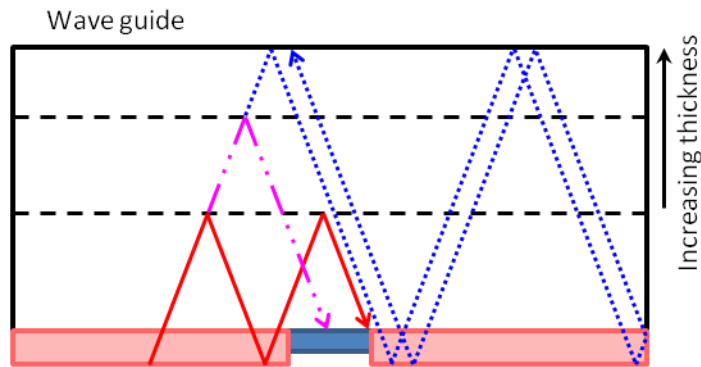


Figure 4.9 Illustration of the effect waveguide thickness and PV cell width has on the transport efficiency of photons to the PV cell.

Standard glass thickness used in windows is between 2-6mm. In this paper, acrylic with similar optical transmission as glass was used as the waveguide material. Standard PV cells purchased are 12.5cm by 12.5cm. From these, 1cm or 2cm wide strips were readily diced and used in panel construction. A single cell was placed in the middle of the LSC and simulations for increasing waveguide thickness were executed for each cell width. The number of trapped photons that were collected by the PV cells was recorded and the results are shown in Figure 4.10. With LR305 as the luminescent species, peak collection occurred at approximately 3mm and 4mm thickness for the 1cm and 2cm wide cells respectively, with the 2cm wide cells exhibiting greater robustness to waveguide thickness variations. A thicker luminescent absorbing layer will exacerbate re-absorption losses increasing the curve roll-off on either side. For large panel structural integrity, a final thickness of 3/16" (4.76mm) was chosen instead.

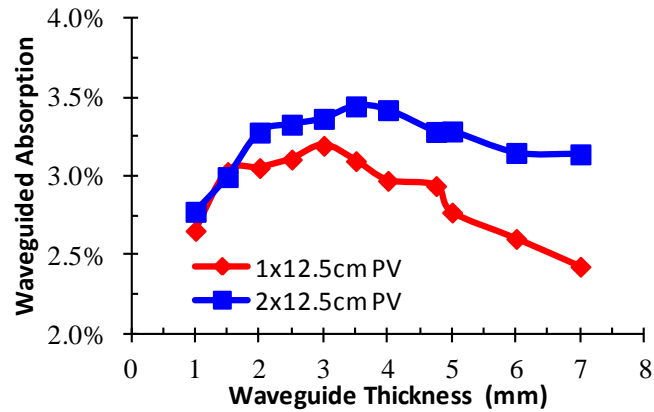


Figure 4.10 Percentage of photons collected by PV cell through waveguiding action versus the waveguide (acrylic) thickness for a single 1x12.5cm or 2x12.5 cm wide cell

Since both direct and indirect light are being collected, γ_{pwr} is maximized when wave-guided photons are able to reach all parts of the PV cell and are evenly distributed across its surface. To better understand the physical effect, cell widths were varied on a 3/16" thick wave-guide and simulated. The cell width is divided into 500 μ m sections. Coordinates of every wave-guided photon collected by the PV cell is recorded and each photon is assigned to one section. From the resulting plots in Figure 4.11, photon concentrations initially become more even as the cell width increases. From 4cm onwards, a marked decline in photons reaching the middle of the cells is observed, indicating that parts of the cell were not being enhanced by the LSC, resulting in a decrease in γ_{pwr} . On very wide cells, the middle sections received only direct illumination with virtually all of the photons absorbed within 3cm from the edge. Together with the waveguide thickness simulations, we can estimate that each centimeter of PV cell width requires an additional 0.15 mm of waveguide thickness

for the best result. The eventual thickness of the LSC panel though would be dictated by more practical issues such as cost, weight, strength and accepted standards in industry.

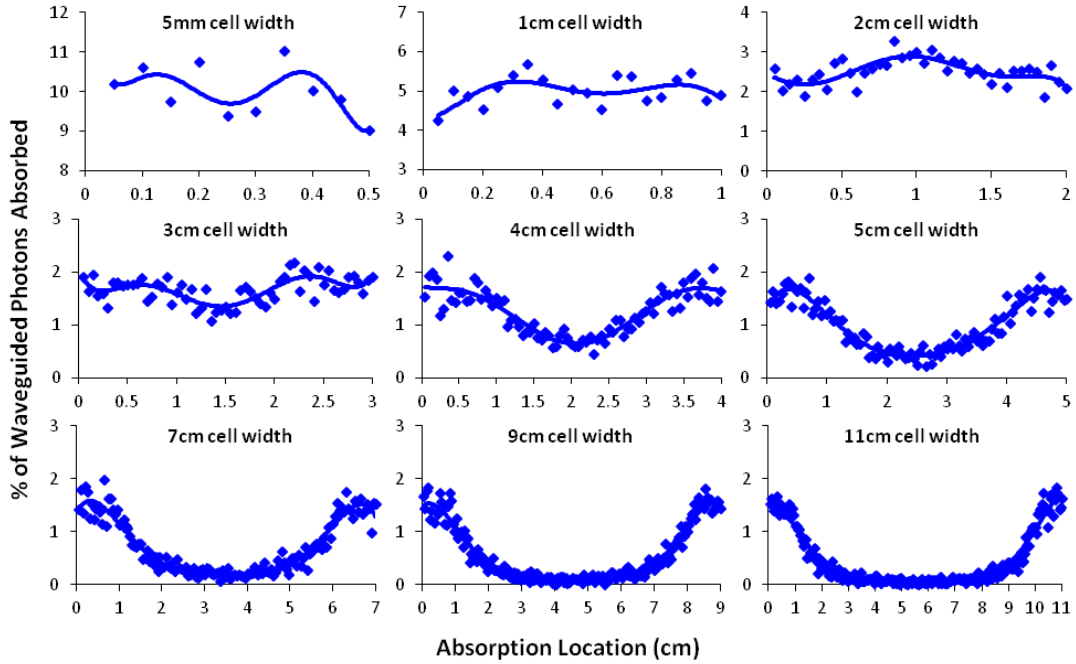


Figure 4.11 Waveguided photons absorbed by the PV cell are counted and grouped by the position absorbed. PV cell width is divided into 500 μ m sections each representing a group. Waveguide thickness: 4.76mm

4.3.2 Panel layout

Larger area of LSC increases the quantity of photon captured by the LSC panel which in turn raises the LSC current contribution. As such, from Equation (3.1), γ_{pwr} is expected to improve with higher LSC to PV cell ratio. In opposition to this, photons captured by the LSC further away from the PV cell experience higher

probabilities of re-absorption and scattering, which may negate any augmentation by the LSC. An optimum LSC to PV ratio results in the highest γ_{pwr} per area LSC added. This in turn would translate into the optimum separation between PV cells on the LSC panel. A series of simulations with increasing panel size were carried out and γ_{pwr} plotted. The PV cell width was set at 2cm and the illumination angle normal to the LSC panel.

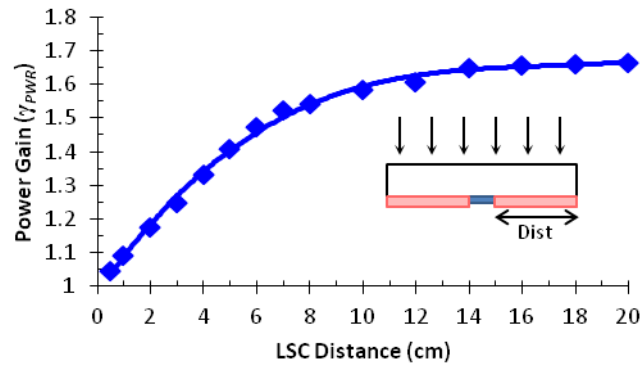


Figure 4.12 Power gain versus 1-sided LSC panel width. PV cell width:2cm, Photons incident angle: 0 deg with respect to plane normal.

Simulations results in Figure 4.12 show an initial linear increase in γ_{pwr} with LSC size which gradually approached a plateau. The linear portion indicates that the additional photons captured by extending the LSC experience little or no re-absorption/scattering events. The simulation results suggest that each PV cell should have 7-9cm of luminescent material on the long edge for the highest improvement in γ_{pwr} per area of LSC added.

To corroborate this with earlier experimental observations, the masked LSC setup (Figure 3.2) was recreated in the simulation model. Measurements were taken from 1-3pm in the middle of September, which places the sun at approximately 48° from the horizon[60]. A comparison of the two results in Figure 4.13 shows a high degree of correlation with an offset between the two. The non-linear transition occurs more gently but begins at about the same point as before, with the mask edge around 7-9cm from the PV cell.

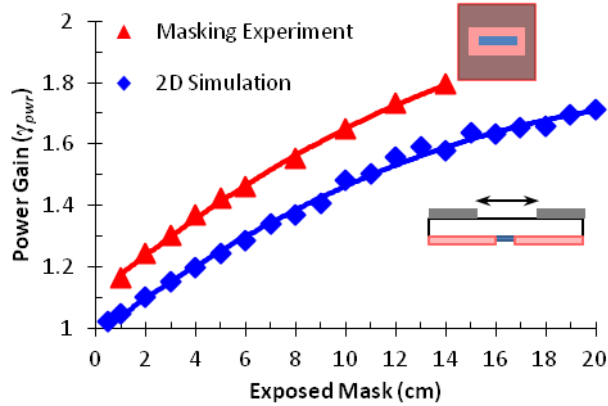


Figure 4.13. Power gain versus the size of exposed LSC, comparing experimental (triangle) and simulation (diamond) results

The difference between experimental and simulation results can be attributed to an overestimation of the overlap between the LR305 absorption/emission curves which leads to higher reabsorption losses in the simulation model. Differences in the reference used for γ_{pwr} calculation is also a contributing factor. Experimental results make use of a completely masked off cell (0cm LSC on each side) as a base line. Whereas in simulation, the number of photons from direct illumination collected by

the PV cell in each run is used as the base line. Another possible factor is the overestimation of scattering in the matrix which would reduce the mean-free-path of photons in the LSC panel and could lead to higher losses.

4.3.3 Response to illumination angle and edge surface treatment

An advantage often cited for LSCs is the ability to collect indirect or diffuse light, precluding the need for solar trackers found in other concentrator systems. To study the operating range of the LSC panel as the sun angle changes, the composition of photons collected by the PV cell was extracted from simulations and plotted (Figure 4.14). The setup consists of a 2cm wide PV cell with 10cm of luminescent material on each side and reflective panel edges. Light intensity on the LSC surface was diminished accordingly with the cosine of the solar zenith angle. Figure 4.14a is plotted as a percentage of the total incoming photons on the panel surface. Figure 4.14b shows the same graph but with percentages referenced to the maximum solar intensity when the solar zenith angle is at 0 degrees.

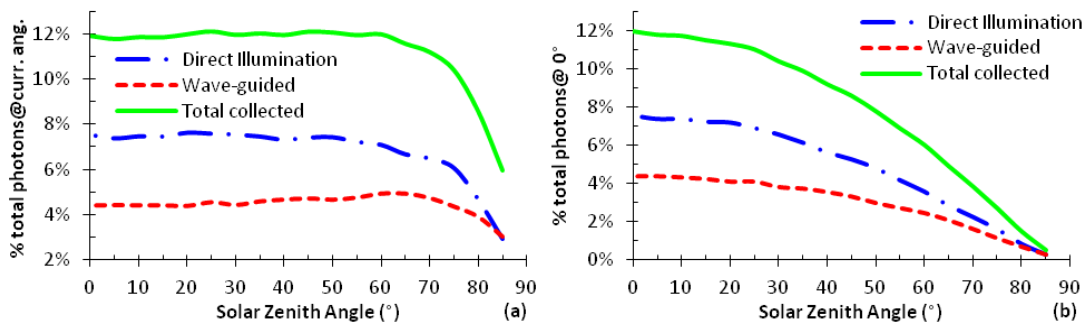


Figure 4.14 Apportionment of photons collected by the PV cell as a function of the incident illumination angle. (a) % of photons referenced to the total number of incident photons on the LSC panel. Light intensity is reduced for larger angles as light is spread over a larger area (b) % of photons referenced to the maximum number of incident photons possible (0 degrees) on the LSC

Over a large range of angles, photon contribution from the LSC remains fairly constant with a slight increase at higher solar zenith angles. Direct illumination on the PV cell on the other hand declines gradually with larger angles. When summed together, the percentage of photons collected by the cell remains within 10% of the maximum up to an angle of 70 degrees. Reflections off the waveguide top increase dramatically beyond this and is manifested by the sharp decline in photons collected. Plotting the data in terms of power gain (Figure 4.15) highlights the larger proportional contribution by the LSC to gain at larger zenith angles.

The front-face orientation of the PV cells allows light to escape through the edges of the waveguide. To alleviate this issue, we consider modifying the edge surface to make it reflective, keeping light trapped in the waveguide. Doing so raises γ_{pwr} by 0.2 (Figure 4.15), a 14% increment, over an unmodified LSC panel. A detailed breakdown of the photon distribution (Figure 4.16) on a 22cm wide LSC panel shows all escaping photons redirected onto the PV cell without increasing re-absorption losses. Higher LR305 concentrations or luminescent particles with larger absorption-emission curve overlaps might result in a percentage of reflected photons being reabsorbed, in which case the panel size would have to be reduced.

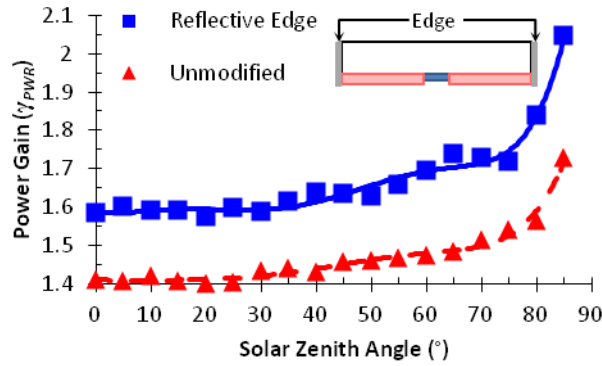


Figure 4.15 Power gain as a function of the incident illumination angle, with (solid line) and without (dotted line) reflective edges.

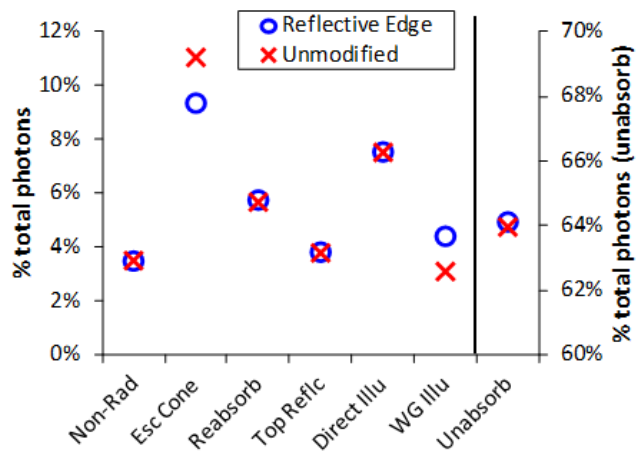


Figure 4.16 Photon distribution in the LSC with (circle) and without (cross) reflective edges. Non-radiative and escape cone losses from single and multiple absorption events are classified separately. Losses from multiple absorptions are grouped collectively under re-absorption losses. Top-reflection refers to incident light reflecting off the top of the waveguide. Photons collected by the PV cell are also separated into those from direct irradiation and those channelled by the waveguide. Photons which pass through the LSC panel without undergoing any absorption or scattering are classified as unabsorbed.

4.3.4 LSC loss mechanisms

In examining the loss mechanism distribution of the LSC panel constructed (Figure 4.16 and Figure 4.17), we can attribute the bulk of it to the narrow absorption

bandwidth of LR305 with over 60% of the solar spectrum lying out of band. Expanding the absorption bandwidth offers the largest potential gain, but this has to be coupled with a larger stoke shift to prevent re-absorption losses from mounting. Incident photons reflecting off the top of the waveguide give a constant 4% loss irrespective of panel size and can be suppressed with anti-reflection coatings. With the assumption that light is emitted isotropically from the luminescent dye, approximately 10% is lost from emission angles that are less than the critical angle and leave the waveguide through this escape cone. A number of solutions include increasing the refractive index of the waveguide material but the drawback is a greater amount of top reflections as indicated by Equation (4.9). Luminescent particles with anisotropic emission can be oriented to transmit light in directions favorable for total internal reflection. Re-absorption losses amount to 5% of the total photons as a result of significant overlap in the dye's emission and absorption spectrum (Figure 3.3A). Quantum dots with larger stoke shifts and multi-dye LSC have been proposed as viable options but care must be taken to ensure that quantum yields remain high enough to not deplete any potential gains. Reviews on LSCs, their loss mechanisms and proposed solutions have been extensively covered in literature[17], [28], [61], [62].

The sharp rise in losses from 0-3cm (Figure 4.17) is mostly from the drop in direct illumination following an increase in the LSC:PV-cell area. For larger panel sizes, this value become less significant and levels out. Non-radiative losses from first absorption events attain a constant value due to the higher quantum efficiencies

provided by the LR305 dye. Losses from unabsorbed photons and escape cone will continuously increase with panel size as larger proportions of incident photons are exposed to the luminescent layer. As expected, re-absorption losses show an initial faster rise with panel size due to the increase probability of absorption with distance travelled. But as each re-absorption event can only result in emitted photons with longer wavelengths, a red-shift occurs in the emission spectrum profile until no overlap occurs with the absorption spectrum and a plateau is eventually reached.

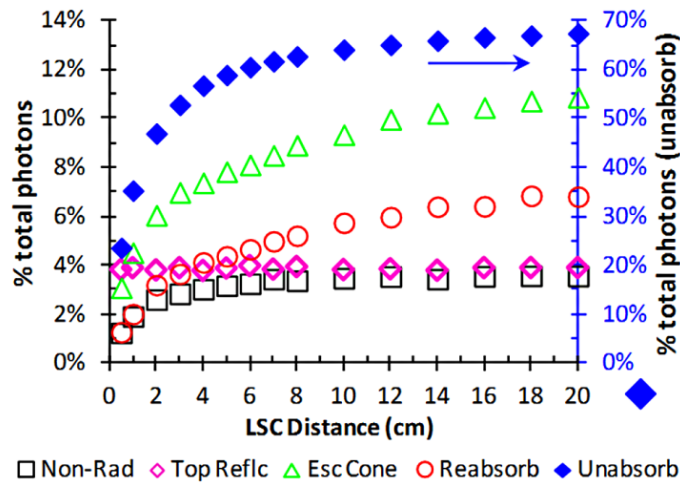


Figure 4.17 Distribution of photon losses in response to increasing panel size. Similar to Figure 4.16, losses from multiple absorption events are grouped into the Reabsorb category

4.4 Comparisons of LSC Layout

With the 3D model, I was able to simulate different layout of PV cells in the LSC panel to better understand the results we were seeing from section 3.3.4. Three panels with the exact same PV to luminescent material area were defined and simulated. Figure 4.18 shows the models and loss bins for each panel. Unexpectedly, there were

only small variations in the escape cone losses, re-absorption losses and indirect photons collected. Improvements in gain and power output with the zig-zag and tic-tac-toe pattern do not seem to be realized. As mentioned in section 4.3.2, the absorption/emission overlap of LR304 and photon scattering in the matrix would have to be relooked at in order to determine if such designs are feasible.

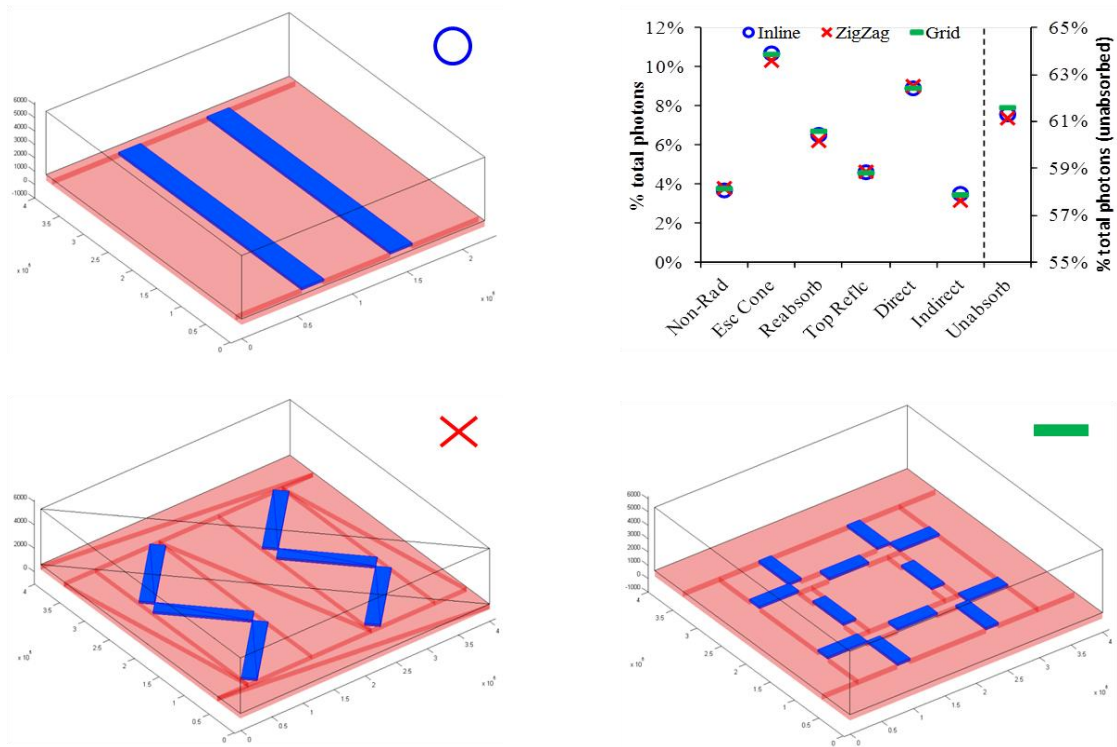


Figure 4.18 Simulation model and results of three panels with the same PV to luminescent area ration but different layout of PV cells.

4.5 Summary and Conclusions

Results from the LSC model closely parallels the behavior of data collected from the experimental mock up panels. This enables the model to reasonably predict the

dimensions and layout of an LSC panel for the desired performance parameter. By tracking the photon's path of travel and analyzing its final outcome, a greater appreciation on the physical mechanisms at work is obtained. Scrutinizing the distribution of the photon outcomes reveals the effect of various design parameters on the power gain, effective operating angles and loss mechanisms in the LSC panel.

III. Quantum Dot Solar Cells

5 Introduction

Recent progress in quantum dot research has shown great promise in our quest for cheaper and more efficient photovoltaics. Quantum dots can be made from economical, earth abundant materials and do not require the high temperature, high input energy processing of first generation crystalline photovoltaics that are common in the market today[63]–[65]. Quantum dots or nano-particles/crystals have diameters typically in the order of nanometer to tens of nanometers. At these dimensions, which approximate the exciton Bohr radius of many semiconductor materials, quantum confinement effects begin to modify the optical and electrical properties away from bulk, opening up such materials for many interesting applications [8]. Applications in third generation photovoltaics have the potential to overcome the Shockley–Queisser limit, raising power conversion efficiency and possibly lowering electrical price-per-watt⁴ generation as compared to current solar technologies.

The electronic band-gap of quantum dots can be tuned by simply changing the size of the particle and this allows for the design of PV cells that are spectrally matched to the sun’s irradiation. This enables the creation of tandem solar cells, where successive layers absorb photons of decreasing energy, thereby harvesting a large portion of the solar spectrum (Figure 5.1) and maximizing power conversion. [66]–[69]. With the proper choice, tandem cells can be created from a single material system, thus simplifying the fabrication process.

⁴ A measure of the capital cost spent to generate one watt of power

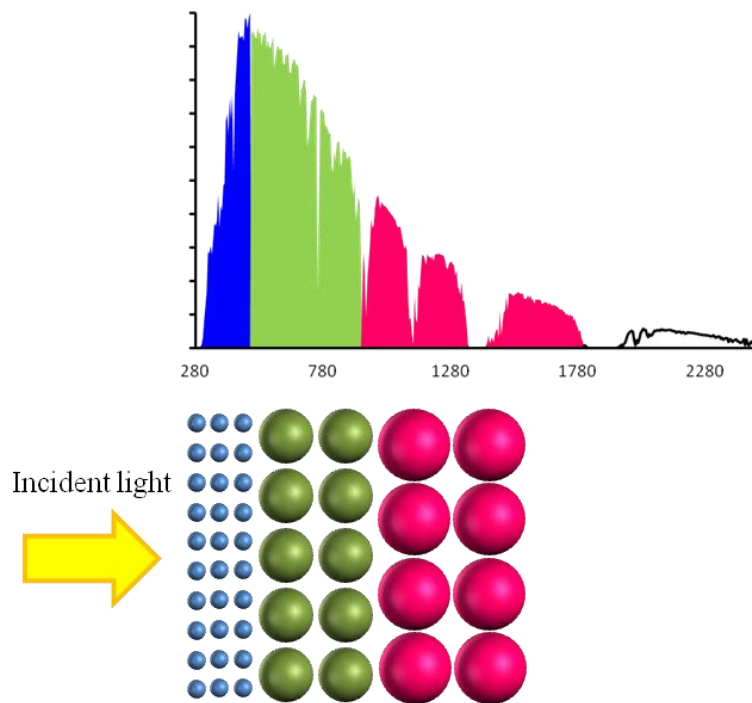


Figure 5.1 Broad-band absorption of the solar spectrum by multi-junction tandem solar cells

Quantum dots synthesized or dispersed in a solution can be applied to a variety of substrates at low temperatures via spin coating, drop casting, ink jet printing or spray coating[70]–[80]. These highly scalable processes can be carried out at room temperature and pressure, a significant cost saving as compared to the expensive vacuum technology that is required in crystalline solar cell manufacturing. . The ease of applying these solar materials to surfaces opens up many options for PV to be incorporated into a building’s structure and design. Coupled with spectral tuning, as described earlier, to absorb non-visible light or incorporating thin film deposition for partial transparency, windows and skylights may be turned into energy harvesting PV cells, utilizing a large portion of the building’s exterior for energy harvesting.



Figure 5.2 Example of a window coated with optically transparent/semi-transparent PV material⁵

⁵Image reproduced from New Energy Technologies, Inc. “SolarWindow”

6 Quantum Dot Solar Cells

6.1 Quantum Confinement

In semiconductors, when sufficient energy is absorbed, an electron is able to surpass the band-gap of the material and move into the conduction band, leaving behind a hole. Columbic attraction between electron and hole creates a bound pair known as an exciton. In bulk materials, excitons are free to move in any direction but when the size of a particle becomes comparable to its exciton Bohr radius (Equation(6.1)), excitons experience quantum confinement[81].

$$a_B = \frac{4\pi\hbar^2\epsilon}{q^2} \left(\frac{1}{m_e^*} + \frac{1}{m_h^*} \right) \quad (6.1)$$

Where ϵ is the dielectric constant and m_e^* , m_h^* are the effective mass of electrons and holes in the material.

Depending on the number of dimension in which this confinement occurs, three types of structures can be defined, each with differing optical and electronic properties. In quantum wells, confinement occurs in only one direction with the exciton free to move in the other two. Likewise in quantum wires and quantum dots, each structure imposes an additional confinement dimension with excitons being unable to move freely in any direction inside quantum dots.

The physical boundaries of these structures act like infinite potential well barriers and solutions to Schrodinger's equation results in discrete energy levels in the

confined space. The confined energy level can be related to the energy of its bulk band-gap by the equation[66], [82]–[84]:

$$E_g(r) = E_{g_bulk} + \frac{\hbar^2\pi^2}{2r^2} \left(\frac{1}{m_e^*} + \frac{1}{m_h^*} \right) \quad (6.2)$$

Where E_{g_bulk} is the band-gap of the bulk material and r the radius of the nano-particle. The second term arises from the increase in energy due to quantum confinement.

We can conclude from this relation that the band-gap energy increases from the bulk value in proportion to the inverse square of the nano-particle’s radius. It is this property that permits quantum dot band-gaps to be altered and spectral tuning to occur. This effect can be clearly seen from the absorbance measurements and fluorescence peak in colloidal nano-particle solutions(Figure 6.1), where the exciton and emission peaks shift toward longer wavelengths with increasing particles size.

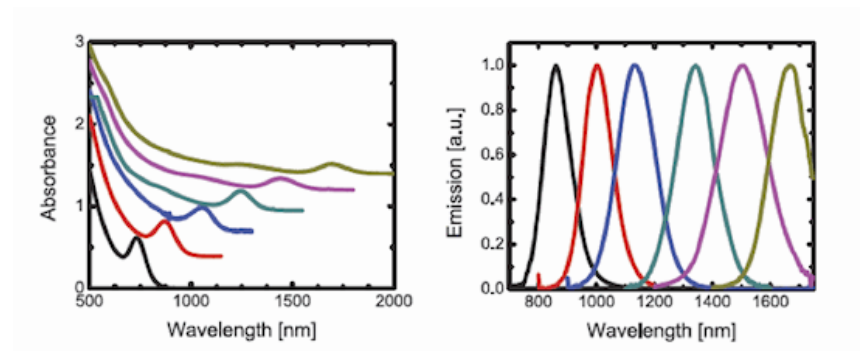


Figure 6.1 Absorbance and emission spectra of PbS nano-particles increasing in size from ~3nm (left) to ~7nm(right) (reproduced with permission)⁶.

⁶ Absorbance and emission spectra reproduced with permission from the Wise research group, Cornell University <http://wise.research.engineering.cornell.edu/qd.html>

6.2 The Schokley-Queisser Limit

The Schokley-Queisser (SQ) limit[85] presents the theoretical maximum efficiency that can be achieved by a single junction solar cell under solar AM 1.5 illumination. The model makes the following assumptions:

- 1) The solar cell is a black body with uniform temperature throughout.
- 2) Radiative recombination is the dominant form of recombination in the solar cell.
- 3) All photons with energy above or equal to the band gap produce the same effect. Electron-hole pairs with excess kinetic energy above the band-gap relax to the band edge via lattice vibration.
- 4) All photons with energy below the band gap are not absorbed.
- 5) Electron-hole pairs which do not combine radiatively are immediately eliminated/extracted.

With these parameters, there is a tradeoff between having smaller band-gaps to absorb more photons at the expense of carrier kinetic energy and vice versa. For the AM 1.5 solar spectrum, the calculated maximum conversion efficiency of 33.7% is attained with a band-gap 1.34eV.

6.2.1 Carrier generation beyond the SQ limit

To go beyond the SQ limit requires addressing the assumptions of the model. Tandem PV cells discussed in Chapter 5 and wavelength converters[86]–[91] seek to reduce losses from wavelength mismatch. Ideally, in tandem cells, excited carriers

from each PV layer are harvested independently to minimize the thermalization effects on charge. Similarly, photon down converters split high energy photons into multiple lower energy photons that are more closely attuned to the band-gap of the material. Wavelength up-converters do the opposite, by combining two or more lower energy photons to form one with higher energy thus extending the absorption bandwidth of the device. The relative ease at which quantum dot band-gaps can be controlled makes it a compelling choice for the production of tandem cell systems.

Carrier multiplication has long been observed in bulk semiconductor devices. When the energy of the photon absorbed exceeds the material band-gap by at least two times, the excess energy, in theory, could be used to promote a second or multiple carriers through impact ionization instead of being lost as heat. But the rate of carrier generation in current commercial solar cells made from Si, CdTe and $\text{CuIn}_x\text{Ga}_{1-x}\text{Se}_2$ are too low compared with rate of thermalization. Significant additional current contribution is only achieved at energy levels many times the band-gap of bulk semiconductors. In Si solar cells, the added efficiency at 4eV (UV light) is only about 5% [92]. These high energy photons only occupy a small fraction of the solar spectrum, resulting in minimal improvement in quantum yield for bulk materials.

In quantum dots where e-h pairs are tightly bound, this effect is seen as the creation of multiple excitons[92]–[95]. While there have been several proposed mechanism to explain the process behind multiple exciton generation (MEG)[86], impact ionization is frequently mentioned as being a likely route. Impact ionization in

quantum dots is sometimes thought of as an inverse Auger process as shown in Figure 6.2. As in the case with bulk semiconductors, ionization must occur at a competitive rate as compared to exciton relaxation, in order to benefit the quantum yield.

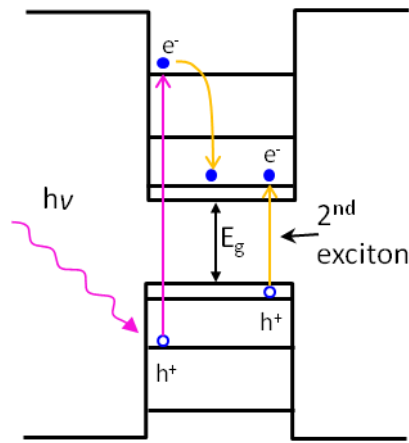


Figure 6.2 Multiple exciton generation via impact ionization

MEG in quantum dots occurs very quickly, in the order of fs, due to strong carrier confinement and increased e-h Coulomb interaction, which favor Auger process[92], [96]. Hot carrier⁷ relaxation dynamics are also known to be affected by the degree of quantization [93]. It was proposed that carrier cooling in nanostructures would require a multi-step phonon emission process, when energy levels were quantized and separated by more than some fundamental phonon energy [97]. Thus strong quantization and greater separation between energy levels serve to raise the cooling time into the ps levels, as compared to sub ps cooling in bulk semiconductors.

⁷ Charge carriers excited to energy levels above the semiconductor band-gap possess kinetic energy equivalent to photons at elevated temperatures and are referred to as “hot carriers”. It does not refer to the physical temperature of the material.

However, alternate pathways for phonon emission exists which might undermine this process, including an Auger mechanism for electrons to transfer excess energy to rapid cooling holes. Slower cooling rates can also improve PV cell efficiency, by providing sufficient time for hot carriers to be extracted from the device before thermal relaxation can occur, resulting in higher output voltages.

6.2.2 Charge carrier recombination

Recombination of charge carriers in semiconductors can take place via three primary mechanisms, namely Radiative, Auger and Shockley-Reed-Hall recombination[8], which can be further subdivided into two categories. Radiative recombination is a result of normal band-band transition by carriers giving rise to photon emission. As this is also a fundamental property of the material by which the carriers are generated, carrier losses in this category cannot be mitigated. Incidentally, this is the only limiting factor accounted for in the Schokley-Queisser limit.

Auger recombination involves interactions between similar carriers. One carrier gains kinetic energy at the expense of another, which undergoes recombination across the band-gap with a carrier of opposite polarity. The surplus kinetic energy is soon lost when the hot carrier relaxes back to the band edges. The rate of recombination is proportional to the density of carriers and shallow traps in the device. While the elimination of shallow traps can reduce the probability of occurrence, this process is largely unavoidable

Shockley-Reed-Hall recombination occurs when carriers captured by trap states in the band-gap recombine with opposite charge carriers before they can gain sufficient thermal energy to escape. This process is greatly facilitated by deep traps where the probability of either electron or hole entering that state is higher. Deep traps are usually a result of defects or impurities in the crystal structure and can be mollified by better processing or annealing. These additional sources of recombination act to diminish the performance of PV cells below the SQ limit.

6.3 Synthesis of Quantum Dots

Quantum dots can be manufactured from a top down or bottom up approach. Top down methods involve fabricating small structures from bulk material through methods such as grinding, lithography and etching. There tends to be a broad size distribution of resulting particles and contamination of the quantum dots. Lithographic-etch processes are also slow and expensive.

Bottom up syntheses usually involve the formation of quantum dots through the mixing of precursors and some form of self-assembly. These can be further subdivided into vapor phase or liquid phase processes. In vapor phase fabrication, precursors are vaporized and then injected into a reaction chamber to form nanoparticles. In pyrolysis, precursors are forced through a nozzle at high pressure and burned to produce solid particles which are then recovered from the gas. Super cooling of vaporized material in an inert gas jet stream is also used to form metal

nano-particles. Spontaneous nucleation of quantum dots on a substrate can also occur using deposition techniques, such as chemical vapor deposition and molecular beam epitaxy[98]. These fabrication techniques, while promising, involve high temperature and expensive vacuum technology.

Liquid phase fabrication involves wet chemical routes which include Sol-gel and colloidal synthesis. These methods are of particular interest because they are simple, cheap processes which can be easily scaled up into high levels of production. Sol-gel begins with precursors which undergo hydrolysis, forming a solution which can then proceed on toward polymerization to form a gel-like network. The resulting sol-gel can be precipitated to produce nano-particle powders or spun on to a substrate to form mesoporous films[99], [100]. Figure 6.3 shows a schematic representation of the process.

Colloidal synthesis is carried out by the rapid injection of precursors into a heated solution containing organic molecules or surfactants and solvents. The precursors decompose and nucleate to form quantum dots. The surfactants attach to the surface of the quantum dots and limit particle growth. They also prevent particles from agglomerating. Proper control of the temperature and concentration are essential in controlling the shape and size of the nano-particles produced [64], [100], [101].

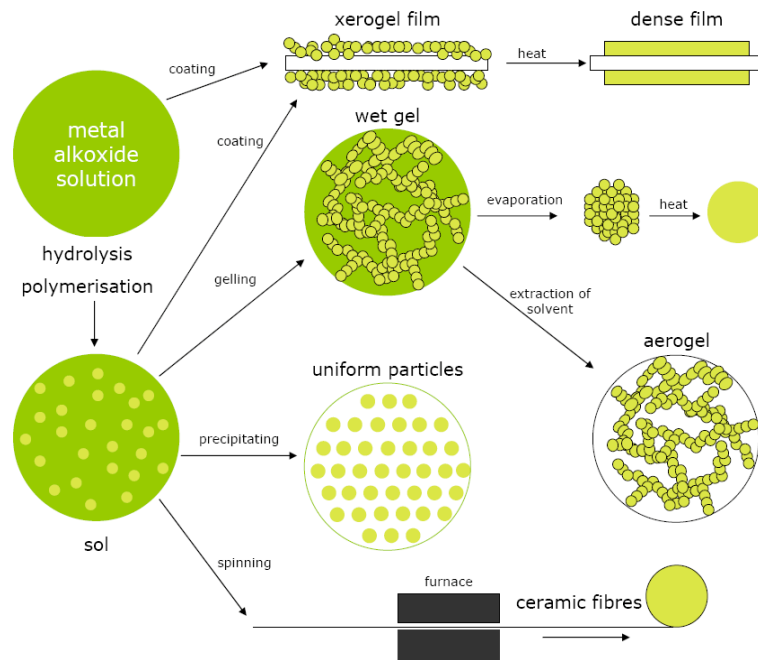


Figure 6.3 Schematic representation of sol-gel synthesis and subsequent processing routes⁸

6.4 Fabrication of QD Solar Cell Devices

In this section, I will describe the process flow used in the production of all our test devices. It is instructive to know how each device is laid out in order to better interpret the results from characterization.

All devices were fabricated on 1" x 1" glass substrates purchased from Thin Film Devices Incorporated and came pre-patterned with Indium-Tin-Oxide (ITO) as the transparent conductor. ITO was deposited via magnetron sputtering to a thickness of $1450\text{\AA} \pm 100\text{\AA}$ with 5\AA (root mean square) roughness and has a resistivity of 20 ± 2

⁸ Image reproduced from <http://www.centexbel.be/solgel-treatment>

Ω/square . The film has a transmittance of 88% at 550nm and a work function of approximately 4.8eV.

6.4.1 Substrate cleaning

Before any deposition, ITO slides underwent ultra sonic cleaning in the following sequence: (1) 1 hour - Alkonox ®; (2) 10mins - Deionized (DI) water; (3) 30mins - Isopropanol; (4) 30mins – Ethanol . This was followed by blow drying using compressed nitrogen (N_2) gas. Except step (1), slides were rinsed in the corresponding solution before undergoing sonication.

6.4.2 Sol-Gel and nano-particle titanium dioxide deposition

Titanium-dioxide (TiO_2), which is able to efficiently extract electrons [93], [102] from the absorber layer, is deposited as a window layer. This is done in two stages, first with sol-gel and then with a colloidal suspension of TiO_2 .

TiO_2 sol-gel was prepared using a standard process described in [103] and briefly repeated here. 125 μL of DI water was mixed with 5mL of denatured anhydrous ethanol (94-96% from AlfaAesar). This was followed by two drop of concentrated hydrochloric acid (HCl) and stirred for 2mins. Lastly, 375 μL of the precursor titanium(IV)-ethoxide ($\geq 97\%$, Sigma-Aldrich) was added.40 μL of Sol-gel was spun onto the substrate at 1350 rpm in air for 40s.Excess sol-gel was cleaned off using ethanol and the substrates were pre-baked at $\sim 140^\circ\text{C}$ on a hot plate for 1 hour before undergoing sintering at 450°C to promote grain growth. After cooling for 1 hour, 40 μL of TiO_2 nano-particles ($\sim 3\%$ by weight concentration, Solaronix) were spun on

at 1500rpm for 40s. This was again treated to the same pre-bake and sintering conditions as the sol-gel.

6.4.3 Quantum Dot deposition

Colloidal nano-particle inks were deposited either by spin casting, dipping, doctor blade or drop casting. Figure 6.4 show examples of films produced using these approaches.

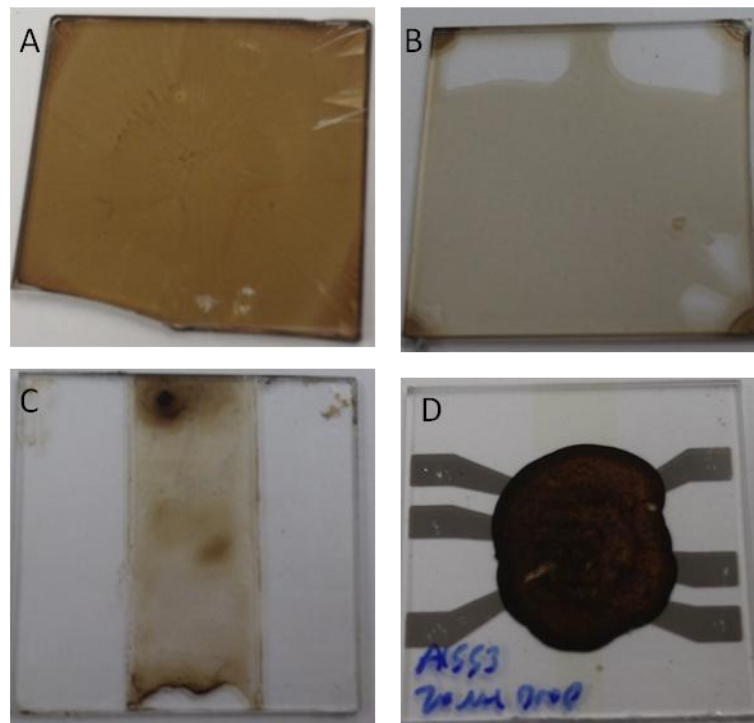


Figure 6.4 Sample images of spun cast (A), dip coated (B), doctor blade (C) and drop casted (D) QD films on glass

Drop casting is a simple method but often results in films which have poor uniformity across the substrate and across samples. This method is usually used to

produce films rapidly and on small substrates. A measured quantity of solution is dispensed quickly onto a substrate and left to dry. In principle, the film thickness depends on the quantity and concentration of the solution used. However, in practice, how well the solvent wets the substrate, the rate of evaporation and capillary forces interpose to vary the thickness and film homogeneity.

Doctor blade is another quick method to deposit films. The solution is dropped onto a substrate between two guides. A blade is then pulled across the guides spreading the solution as show in Figure 6.5. Film thickness is controlled by the height of the guides, the surface energy of the substrate and the concentration and surface tension of the solution. This method can produce uniform thin films but is subjected to the thickness of the guides.

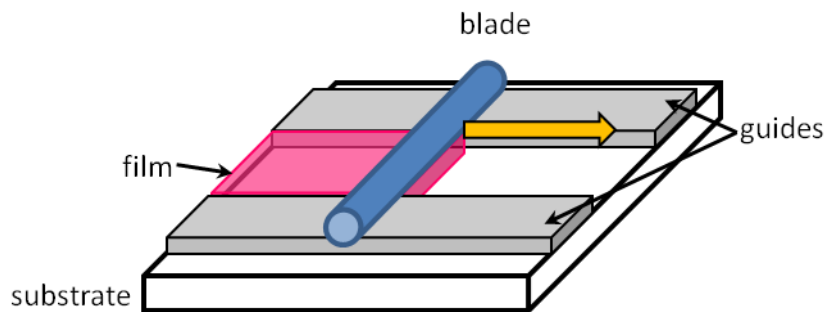


Figure 6.5 Doctor blade coating process.. The blade is use to shear the colloidal nano-particle into a evenly distributed film with the guides determining the thickness of the deposited material.

Dip coating is done by immersing the substrate in the nano-particle solution and then slowly withdrawing it. In the process, nano-particles in the solution are pulled

into the meniscus forming a thin layer on the surface of the substrate. Pull rate, solution concentration and surface tension control the final film thickness.

In spin coating , a substrate is placed on a vacuum chuck and spun at a high rate while a quantity of nano-particle solution is introduced into the center of the substrate. The film is dispersed uniformly across the substrate via centrifugal force, leaving behind a thin layer of particles after the solvent has evaporated. Film thickness depends on the spin speed, spin duration and solution concentration. This method boasts better uniformity, good control of film thickness and low variability across samples.

In this work, dip coating and spin casting produced films that were individually too thin. Ligand exchange was performed to render the film insoluble in the colloidal solution solvent so that another layer may be added. In this way, films are built layer by layer and the final thickness can be well controlled.

6.4.4 Ligands

The synthesized colloidal nano-particle solutions typically contain long hydrocarbon chains, such as oleic acid (OA) and oleylamine (OAm), attached to the particle surface. As mentioned in section 6.3, these ligands limit the growth of nanoparticles and also act to stabilize the particles in non-polar and hydrophobic solvents[100]. During film deposition, these ligands also play a key role in determining the packing structure and electronic properties of the film. The organic ligands are usually electrically insulating, which help to keep charge carriers confined.

In order to produce conducting films, the quantum dots must be spaced close enough to have sufficient electronic coupling for mini bands to form[93], [104]–[106]. The coupling energy[69] between neighboring QDs can be expressed as:

$$\beta \approx h\Gamma \quad (6.3)$$

Γ is the tunneling rate approximated by:

$$\Gamma \approx \exp\left(-2\pi\Delta x \sqrt{\frac{8m^*\Delta E}{h^2}}\right) \quad (6.4)$$

where m^* is the carrier effective mass, Δx the tunneling barrier width and ΔE the barrier height. From Equations (6.3) and(6.4), narrower QD separation reduces the barrier width (Figure 6.6),favoring higher tunneling probability and raising the coupling energy. It has been shown as well that carrier mobility decreases exponentially with ligand length, as expected from the hopping mode of carrier transport[104].

Syntheses of quantum dots contain a certain amount of dispersion in their size. This in turn could lead to some measure of disorder in the deposited films, which may have a detrimental effect on the formation of mini-bands. But if the coupling energy is high enough to overcome the dispersion in energy, extended wave functions and hence mini-bands can still exists[107], enabling long range carrier transport.

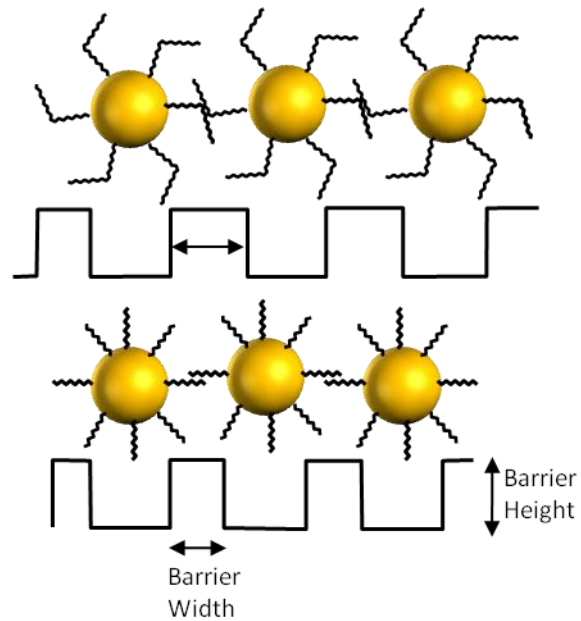


Figure 6.6 Schematic of the ligand exchange process. Shorter ligands result in a closer packed structure which reduces the tunneling barrier width.

6.4.5 Metallization

In the final fabrication step, 100nm of silver (Ag) were thermally evaporated onto the substrate under high vacuum ($<10^{-6}$ Torr). The overlap between the metal back contact and ITO forms the device area of 0.03cm^2 . The final top down layout and cross section of the QD solar cell are shown in Figure 6.7. Sol-gel TiO_2 forms a hard glass layer that helps to prevent short circuit pathways from forming.

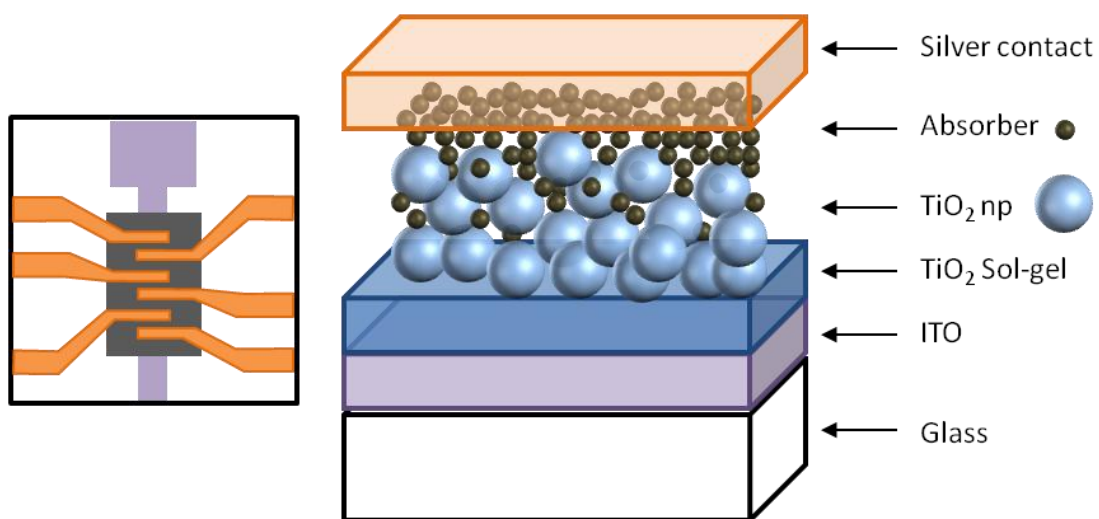


Figure 6.7 Top down layout and cross sectional view of the quantum dot solar cell structure. Overlap between the metal leads and ITO defines the device area.

7 Germanium Quantum Dot Solar Cells

7.1 Introduction

Germanium (Ge) has a long history of use in the semiconductor industry. Early semi conductor devices were mostly based on Ge before it was gradually replaced by cheaper and more readily available silicon (Si). Ge is relatively abundant in the earth's crust. Its low toxicity and recent improvements in synthesis of colloidal solutions, has attracted attention into research the replacement of lead and cadmium quantum dot solar cells with Ge quantum dot devices..

Earlier work performed at our group has succeeded in fabricating Ge-TiO₂ hetero junction photo diodes with up to 100 μ A photo current at 0.5V bias and possesses on-off current ratios that are greater than 100 [71]. Recently, the group has achieved a first in producing a working, all nano-particle, Ge-TiO₂ PV cell with efficiencies higher than previously demonstrated PV cells made from polymer-Ge blends and Ge nano-particles on Silicon.

Moving forward from this, we seek to improve upon these earlier lab results by investigating alternative methods to treat Ge QD surfaces, and exploring other types of QDSC structures to improve output current densities and voltage. We also attempt to further characterize the Ge films in order to gain a deeper understanding on how the films may be processed.

7.2 Experimental Methods

Colloidal Ge nano-particles were provided by UC Davis synthesized using microwave assisted heating as described in literature[108]. Oleylamine was used as the binding ligand and the particles were dispersed in Toluene.

Ge-TiO₂ QD devices were fabricated according to the procedure outlined in section 6.4. ITO slides were cleaned using the four step ultra-sonic process after which sol-gel and nano-particle TiO₂ were spun onto the substrate in air and at room temperature. The slides were then brought into a glove box over pressured with nitrogen gas. All Ge devices were fabricated with oxygen levels less than 50ppm. 10-20 μ L of Ge QD solution was dispensed onto the substrate, spun at 2500 rpm for 30sec and left to dry. Large QD separation caused by the long Oleylamine (C₁₈H₃₇N) ligand produces films which exhibit poor conductivity. Ligand exchange was carried out by dipping the spun cast films in 1 Molar Hydrazine in Acetonitrile (1M Hyd:AcN) for 15sec. After drying, the next layer of Ge QD is spun on. The whole spin-exchange process is repeated until the desired thickness is reached. Any excess film is removed from the sides and back of the substrate before evaporation of contacts. Completed devices were allowed to sit for 24 hours after metallization before electrical characterization.

Light testing was carried out using a Oriel solar simulator with its output calibrated to match the AM 1.5 (air mass index) solar spectrum. Illumination intensity was calibrated before each test session by measuring the known response of a silicon

photo detector using a Keithley 2400 source meter. Current-Voltage curves were obtained by sweeping the bias voltage across the device from -1V to 1V while recording the current. I-V curves were obtained for the device with and without illumination. Film absorbance was measured using a Jasco V670 spectrometer.

Three samples of QD solution with nano-particle size ranging from ~3-7nm were provided. Powder X-ray diffraction measurement (Figure 7.1) indicates a cubic crystal structure. A rounding of the diffraction peaks suggest that there is a decrease in crystallinity with particle size.

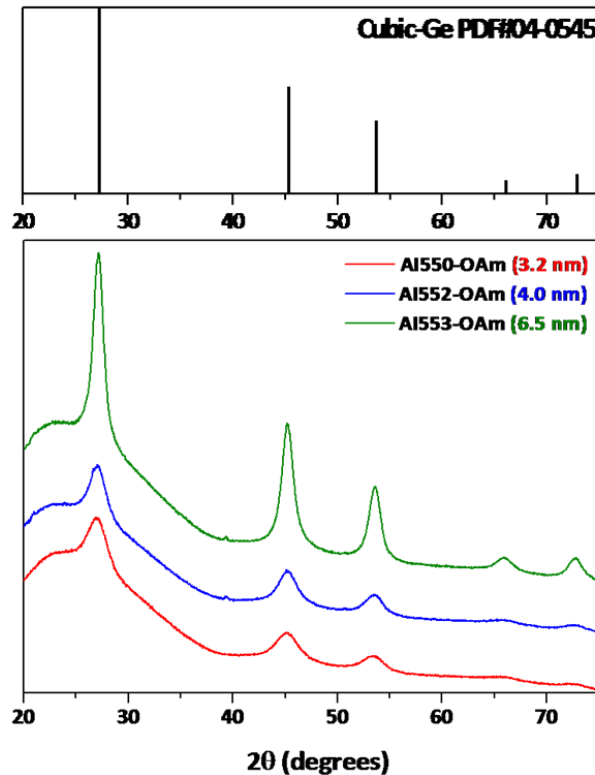


Figure 7.1 Powder X-ray diffraction measurement of the germanium nano-particles

7.3 Results and Discussion

To measure the absorbance of the nano-particles, films consisting of three spin-cast cycles each were deposited on to a glass substrate and measured. From the absorbance spectrum shown in Figure 7.2 it would appear the 3.2nm (AI550) QD films were much more absorbing at higher energies. This result is complicated by the fact that although all nano-particle inks provided have the same concentration of about 17mg/mL and passivated by the same oleylamine ligand, the films produced were consistently different visually. The inset image in Figure 7.2 shows that AI550 is much darker with the same number of spin cycles, followed by AI553 and then AI552. It is possible that the nano-particle size is affecting the surface chemistry which in turn influences the spin-cast and ligand exchange process.

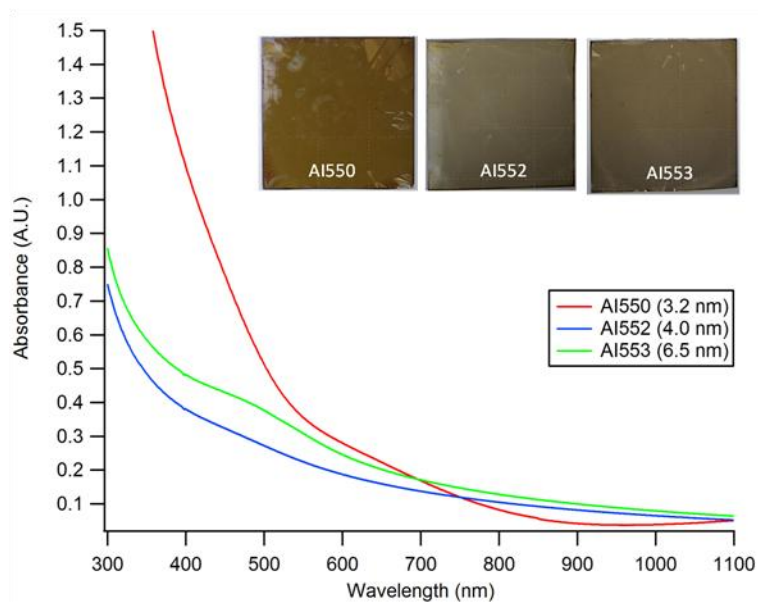


Figure 7.2 Absorbance measurements of Ge nano-particle films fabricated with three spin-cast cycles. Inset: image of the films deposited.

A small hump seen on the absorbance curve of AI553 seems to indicate an excitonic peak near 500nm. The lack of a peak in the curves of AI550 and AI552 is in line with the amorphous nature of those particles, whose larger spread in particle sizes smoothes out the peak.

Interestingly, the illuminated current density-voltage (J-V) curves (Figure 7.3) of devices fabricated show that AI552/3 possess higher current densities despite having lower absorption values. Both films have the same short circuit densities of $\sim 80\mu\text{A}/\text{cm}^2$ and very similar absorbance levels, which implies that the difference in J_{sc} is related to the film thickness. This result could be indicative of low carrier life time and high recombination in these devices.

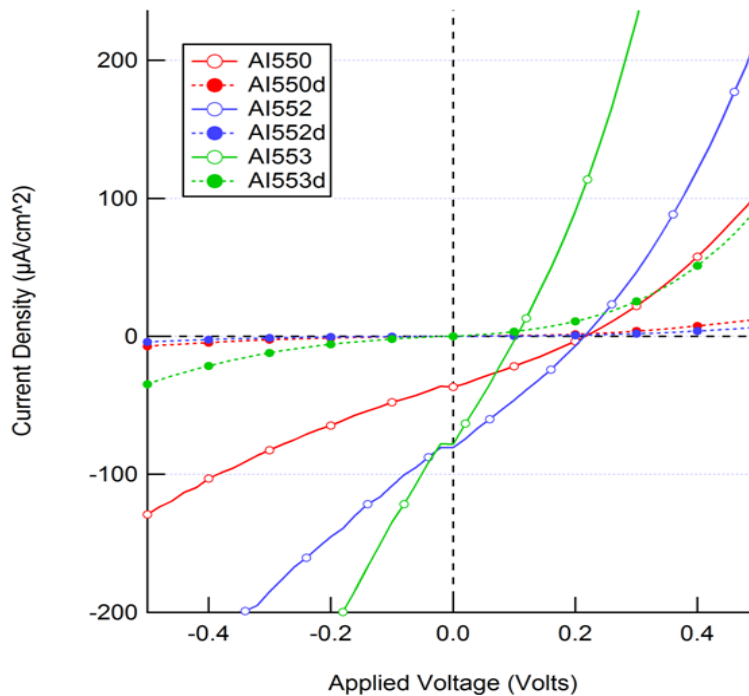


Figure 7.3 J-V curves of Ge quantum dot solar cells with nano-particles ranging from 3-7nm taken in the dark (dotted) and under AM1.5 solar illumination (solid)

V_{oc} of AI553 is 0.102V which is half that of AI550 at 0.21V. It is unclear from Figure 7.3, if the reduction in V_{oc} is due to the smaller band-gap in AI553 or parasitic resistances. Following this, a thickness study was performed using AI550 where film thickness was varied using 2,3 and 4 spin-cast cycles. The J-V results shown in Figure 7.4 presents very similar variations and values to Figure 7.3, with J_{sc} and V_{oc} of the Ge 2x film reading $0.90\mu A/cm^2$ and 0.104 V respectively. This gives a strong indication that the films contain strong resistive and shunt pathways reducing both J_{sc} and V_{oc} .

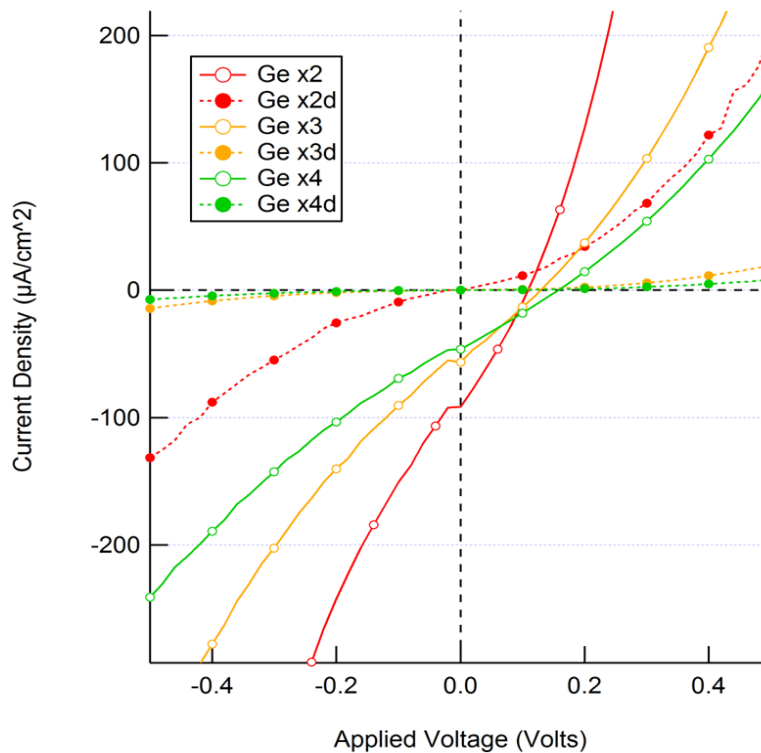


Figure 7.4 J-V cures of Ge nano-particle devices with increasing number of spin-cast cycles (thickness). Dotted lines indicate dark curves and solid lines are light curves.

7.3.1 Thermal Annealing

To improve mobility and long range transport of carriers in the Ge-np films, a thermal anneal study was carried out. The expectation is that annealing will crystallize the nano-particles producing larger grain size and also reducing QD-QD spacing by burning off some of the surface ligands. The negative connotation is that we lose the quantum confinement properties bringing the system closer to an amorphous film as opposed to an array of quantum dots.

Figure 7.5(A) shows log plots of the J-V with substrates annealed at various temperatures. All QD films were deposited using three spin-cast cycles of AI553 nano-particle ink. Devices were then heated on a hot plate at temperatures 80, 120, 200, and 300°C for 10 mins before undergoing cooling and metallization. Thermal anneal results in an increase in current density with temperature, saturating at approximately 200°C. The highest J_{sc} attained was 301 μ A, four times higher than the reference device. V_{oc} is reduced drastically from 0.11V to 0.015V. While this behavior may be a result of grain growth and closer packing structures, it could also be a result of a more porous film, providing opportunities for shunting pathways to form during metallization. Nano-particle film absorbance (Figure 7.6) for the most part shows little change with annealing except for the film annealed at 300 °C. A slight shift in the inflection point at 500nm is observed but further test would be required to ascertain this result.

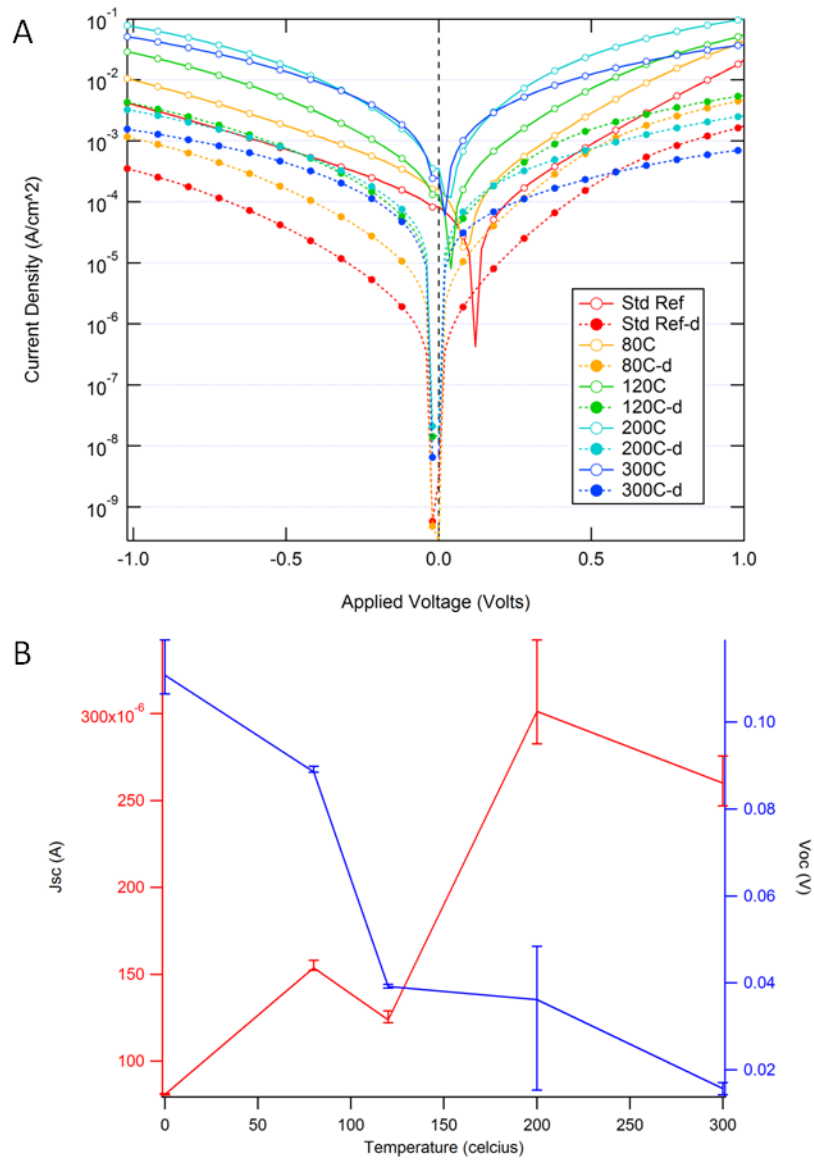


Figure 7.5 (A) J-V curves of Ge nano-particle devices annealed at 0, 80, 120, 200 and 300°C for 10 mins. (B) Plot of J_{sc} and V_{oc} versus anneal temperature. All Ge films deposited using AI553 for 3 spin-cast cycles.

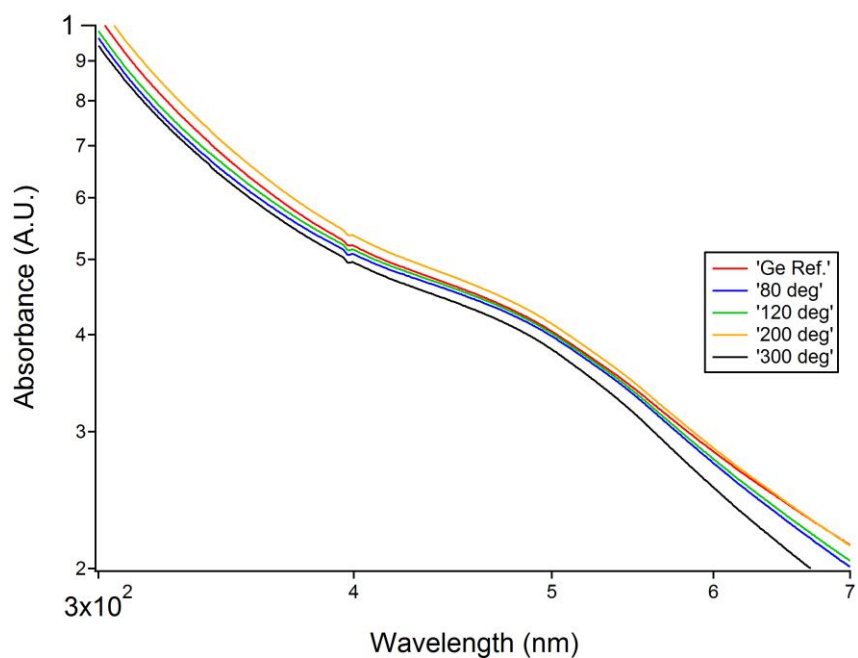


Figure 7.6 Log plot of the absorbance curves for thermally anneal Ge nano-particle films. Anneal temperatures at 0, 80, 120, 200 and 300°C.

7.4 Conclusions

Current Ge nano-particle solar cell device performance may be limited by high parasitic resistance in the quantum dot film. Data collected on the impact of film thickness and particles size on J-V curve behavior indicates short carrier lifetime and likely high carrier recombination. Thermal treatment succeeded in raising photo current by up to four times but at the expense of open circuit voltage.

Much work remains to be done in seeking better passivation techniques for the QD films. A change in device structure may be needed to enable faster extraction of carriers form the device.

8 Silicon Nano-Particle Solar Cells

Similar to germanium nano-particle solar cells, silicon nano-particles (Si-np) offers the same benefits of potentially higher efficiencies by circumventing the Shockley-Queisser limit and reduced cost through the application of thin film processes [109]–[112]. In addition to that, silicon is very abundant in the earth's crust and is considered non-toxic. It is also currently the most widely used semiconductor material in industry.

Common methods of producing large quantities of Si-np are through the mechanical fracturing of porous silicon or chemically decomposing gaseous silicon compounds. However, both of these approaches require further etching with nitric acid and hydrofluoric acid before yielding a stable, well passivated hydrogen surface [113]. A method to chemically synthesize hydrogen capped silicon at ambient temperature, without the use of acids would help simplify processing and reduce the use of hazardous chemicals. After passivation, the functionalization of the nano-particles can then be carried out.

Our collaborators at UC Davis provided colloidal Si-np synthesized using low temperature solution routes described in [113]–[115]. Solution reaction of sodium silicide or the decomposition of silicon tetrachloride was used to produce hydrogen and chlorine capped nano-particles respectively. Further treatment was then carried out to produce propylamine terminated Si-np. The particles were stable in air and soluble in water or other polar solvents.

8.1 Experimental Methods

Samples of Si-np provided were dispersed in de-ionized (DI) water, acetone or methanol. For the most part, fabrication of Si-np devices follows that of Ge-np and utilizes the same steps described in section 6.4. An issue encountered with Si-np was the failure of the ligand exchange process. Strong Si-C bonds on the nano-particle surface made it difficult to displace the long propylamine chains with shorter ligands. As such, attempts to build Si-np films through layer by layer deposition were abandoned in favor of drop casting, which employs only a single deposition step.

To perform drop casting, Si-np solutions not dispersed in DI water underwent a solvent exchange with pyridine. This was performed by repeatedly boiling off part of the solvents and continuously diluting the solution with pyridine until the original solvent is replaced. To ensure that a sufficiently thick Si-np film is produced, the nano-particle solutions were concentrated (Figure 8.1) up to six times through gentle heating at 80° C. Care was taken not to evaporate too much solvent such as to cause the nano-particles to crash out of solution.

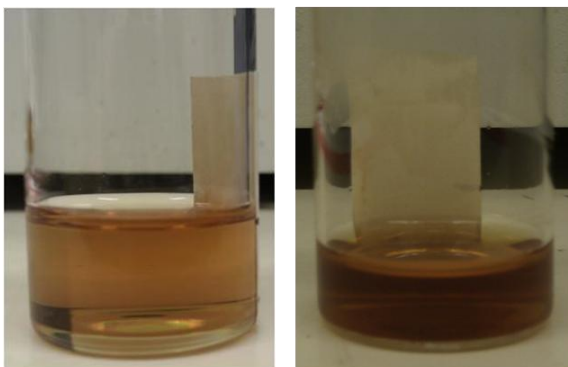


Figure 8.1 Concentrating Si-np solutions to produce sufficiently thick films during the drop cast process

Si-np films in pyridine, drop-cast under vacuum produce the most uniform films (Figure 8.2D). Allowing the film to dry in air resulted in bands of thicker material forming (Figure 8.2A and C). It is critical that the slides are thoroughly cleaned of oils and other hydrocarbons to reduce surface tension. This allows for the solution to spread thinly over the glass slide with improved film uniformity. To carry out electrical test, several Schottky diodes were made using the vacuum drop-cast technique with Si-np on ITO-glass. 100nm of silver were deposited via evaporation to form the back contacts.

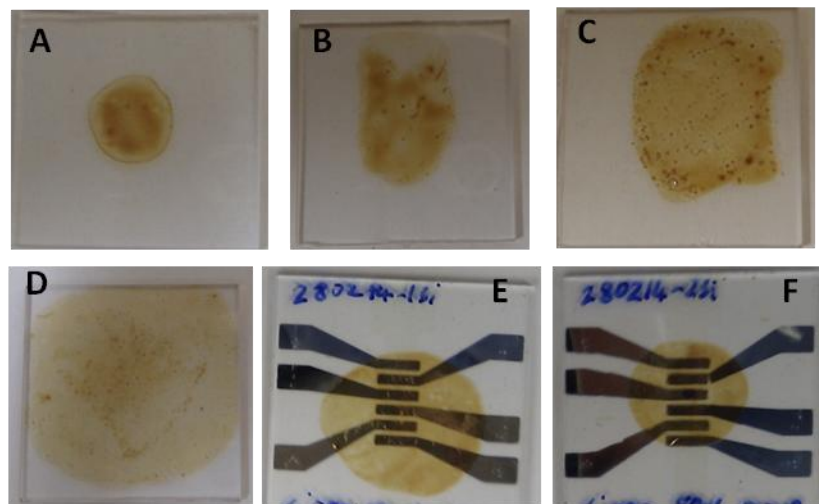


Figure 8.2 (A) Si-np in DI water drop cast in air; (B) Si-np in DI water drop cast under 25'' hg vacuum; (C) Si-np in Pyridine drop cast in air; (D) Si-np in Pyridine drop cast under 25'' hg vacuum. (E) ITO-Si-np schottky diode formed by vacuum drop cast of 100µl Si-np solution; (F) ITO-Si-np schottky diode formed by vacuum drop cast of 50µl Si-np solution;

Optical testing and electrical characterization was carried out following the same procedures as germanium described in section 7.2. In addition photo luminescence spectroscopy was performed using a PerkinElmer LS 45 Fluorescence Spectrometer.

8.2 Results and Discussion

Figure 8.3 shows the absorbance and photoluminescence spectra of Si-np films made by drop-casting 100 μ l of solution. The absorbance spectrum (Figure 8.3A) does not show any excitonic peak which could indicate that the nano-particle size dispersion is large. The photoluminescence spectrum shown in Figure 8.3B exhibits multiple peaks at all excitation wavelengths, with two larger peaks located at ~400nm and ~540nm when excited by a 320nm and 405nm light source respectively. This could indicate the presence of mini-bands in the Si-np or a distribution of nano-particles sizes in the films clustered around the two strongest peaks [116]. When converted to energy, the emission peaks correspond to energy transitions between 2-3eV. If the transitions correspond to the energies of band-gaps in the film, we can estimate the Si nano-particles to be between 1nm and 3nm in size [117]. This is smaller than the exciton Bohr radius of Si, approximately 5nm [109], and suggest that the Si-np exhibits quantum confinement.

It is interesting to note that the large luminescence peak at 400nm is suppressed strongly when the excitation wavelength shifts from 320nm to 345nm and 355nm, even though the photon energies exceed the band-gap. Similarly the 450nm luminescence peak is reduced when excitation wavelength is increased from 345nm to 355nm and 405nm. This could imply that the Si-np band-gap is indirect.

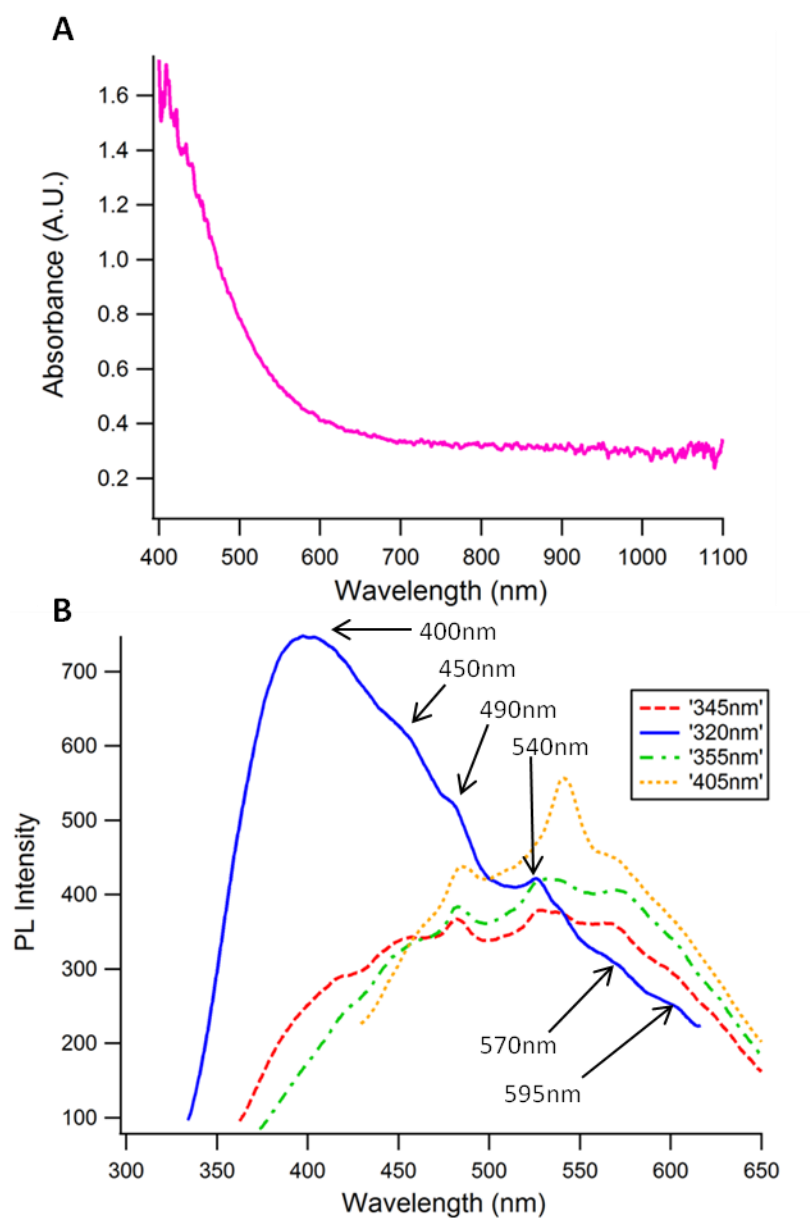


Figure 8.3 (A) Absorbance spectrum of a 100µl drop-cast Si-np film; (B) Photoluminescence spectrum of a 100µl drop-cast Si-np film.

Figure 8.4 shows the Current Density versus Voltage (J-V) plot of Schottky devices made by drop-casting 100µl and 50µl of Si-np solution in vacuum. Both

devices exhibit a photovoltaic effect but with very low current density, in the hundreds of nano-amp range. As ligand exchange was not successful, the Si-np remains insulated by long propylamine molecules, increasing nano-particle separation and reducing charge transport. Short-circuit current and open-circuit voltage increase with the amount of solution used and could be correlated to the thickness of the films. Interestingly, the devices exhibit an open-circuit voltage even in the dark when none is expected.

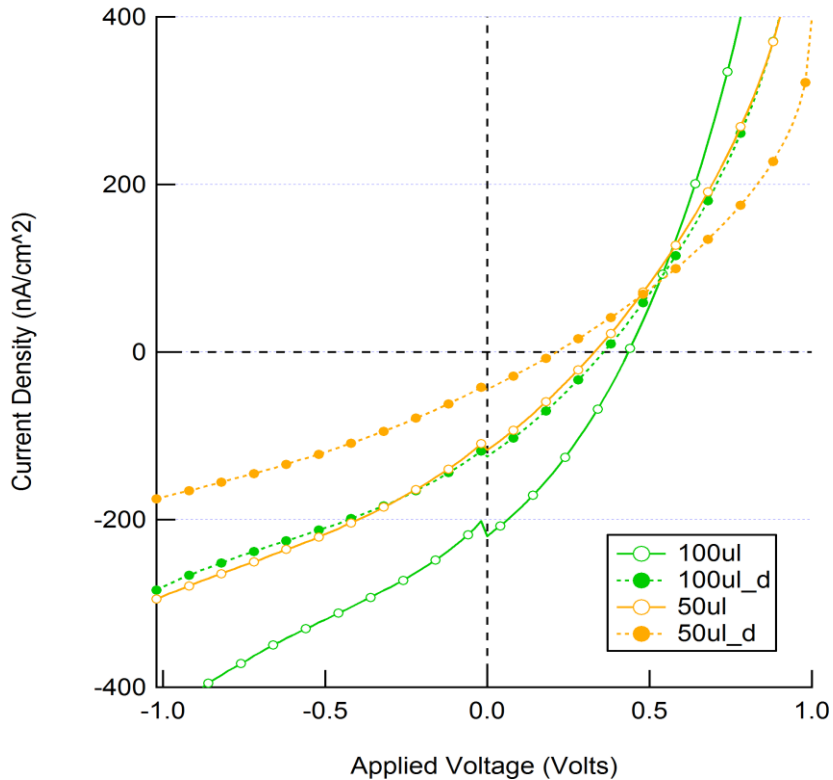


Figure 8.4 J-V curves with (solid) and without (dotted) illumination of Si-np Schottky diodes, made using the drop-cast technique with 100 μ l (green) or 50 μ l (yellow) of Si-np colloidal solution. Bias voltage swept from -1V to +1V.

To investigate the cause of a dark open-circuit voltage, a series of J-V curves were taken with increased voltage range and reversed polarity sweeps.

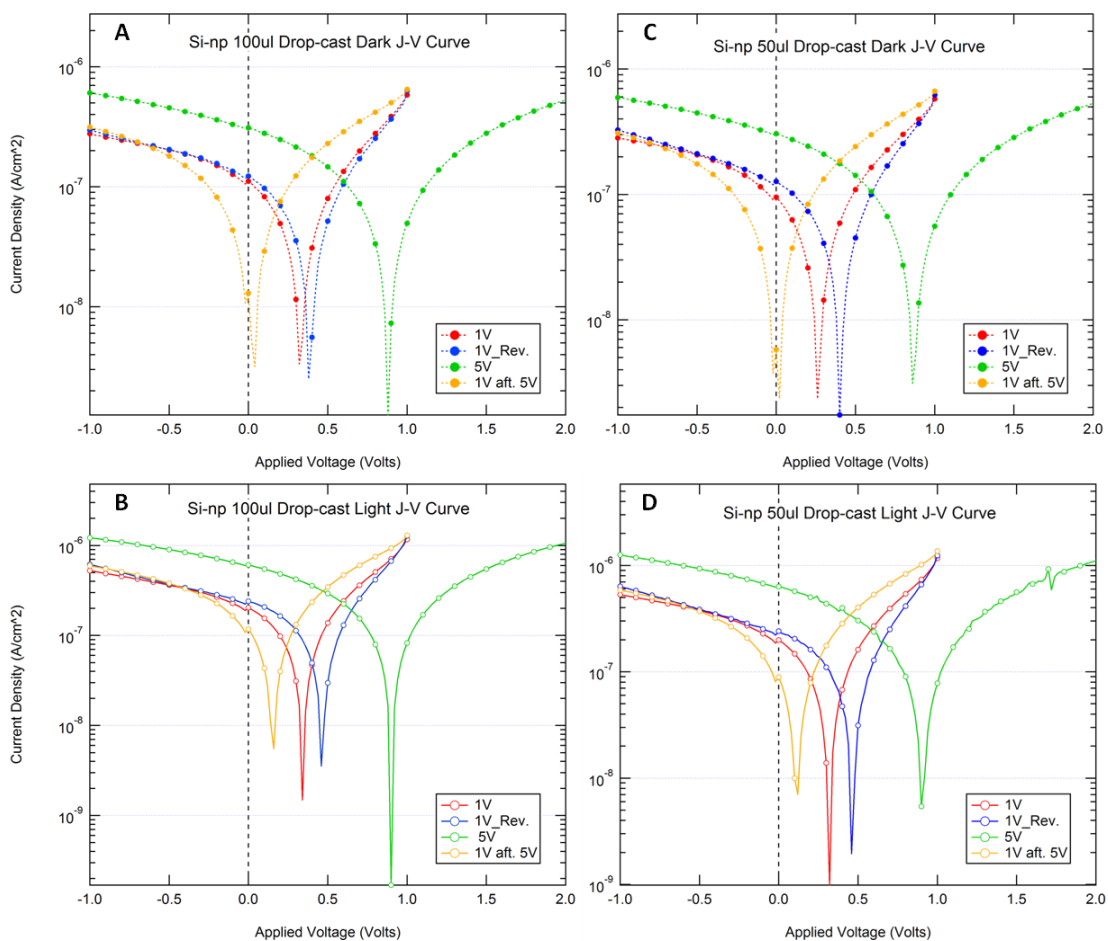


Figure 8.5 (A) Dark J-V curves: Si-np 100µl drop-cast Schottky device; (B) Illuminated J-V curves: Si-np 100µl drop-cast Schottky device; (C) Dark J-V curves: Si-np 50µl drop-cast Schottky device; (D) Illuminated J-V curves: Si-np 50µl drop-cast Schottky device

Figure 8.5 shows the light and dark J-V curves for forward (red) and reverse (blue) polarity $\pm 1V$ bias voltage sweeps, $\pm 5V$ (green) bias voltage sweep and a $\pm 1V$ bias voltage sweep (yellow) immediately following a $\pm 5V$ sweep. The forward/reverse

sweeps were carried out with a pause of several minutes in between measurements. The devices exhibit a small amount of hysteresis and could be the result of the movement of trapped charges in the nano-particle films. The $\pm 5\text{V}$ sweep shows considerable gain in J_{sc} and V_{oc} but otherwise produces consistent diode J-V curves. Of note is the shift in the $\pm 1\text{V}$ J-V curve (yellow) toward the origin when measured without pause after the $\pm 5\text{V}$ sweep. It was also observed that after the completion of J-V measurements, a rapid discharge current could be seen with the device biased at 0V. After a pause of about one minute, the device J-V curve is returned to its original state. This memory effect and discharge current is indicative of charge storage occurring within the Si-np film during testing.

8.3 Conclusion

Silicon nano-particle Schottky diodes were fabricated using the drop-cast method under vacuum. Devices demonstrated photovoltaic effects but with low current densities as a consequence of large nano-particle separation, and reduced carrier mobility in the nano-particle films. Presence of a significant open circuit voltage even in the dark could be the result of trapped charges in the Si-np films. The films at their present state have a tendency to collect charge as displayed in the J-V curves of voltage sweeps performed. Further investigation is ongoing to elucidate the charge retention and Dark- V_{oc} phenomena observed in this first batch of Si-np produced.

Appendix

3D Ray Tracing Program for Luminescent Solar Concentrators

This iteration of code performs a sweep on the LSC panel width. To perform sweeps on other parameters, modify the variable list and loop control variable.

```
% NOTE all dimensions are in MICRONS
% Panel dimensions: Wave guide [h=0.47625cm (3/16")], LSC [h=0.04318cm (0.017")], PV cell [h=0.01778cm (0.007")]
clear; %clear previous simulation data stored in memory
%*****Anonymous Functions*****
round_dp=@(X,dp) round(X*10^dp)/(10^dp); %anonymous function to round up to the number of decimal places specified by dp
Fresnel=@(n1,n2,cos t) (((n1^2*abs(cos t))-n2^2*abs(cos t))/(n1^2*abs(cos t)+n2^2*abs(cos t)))^2; ...
% Fresnel equation: calculates fresnel reflection coefficient
%abs(cos ?) used in refract bcos formula works for 0<Theta<90 but we have not put that restriction on Theta in this program
%*****

% NOTE: limitation, only able to handle 3D objects with 6 faces (8 vertices) at this time.
% Define all zones in the Panel by the COORDINATES of their VERTICES in a CLOCKWISE sequence starting with the bottom later then the top
% as shown in the figure below
%
%      P6-----P7
%      /       \
%     /         \
%    /           \
%   P5-----P8
%   /       \
%  /         \
% /           \
% P1-----P4
%
% data is stored in a cell-array (curly brackets) to allow storing of mixed "TEXT" and "NUMERICAL" data (special handling required to use contents)

Cell_Length=12.5*10000; %Length of PV cell in Microns
Cell_Width=2*10000; %Width of PV cell in Microns
Cell_num=1; %number of PV cells
Cell_sep=7.8*10000; %separation between PV cells
%Panel_Width=[3 4 6 8 10 12 14 18 22 26 30 34 38 42]*10000; %Loop the program with varying Panel Sizes
Panel_Width=22*10000; %Total Width of the Panel
Panel_Length=22*10000; %Total Length of the Panel

WG_Tik=4.75*1000; %thickness of waveguide
LSC_Tik=431.8; %thickness of Luminescent sheet
Cell_Tik=177.8; %thickness of PV cell
Panel_Tik=WG_Tik+LSC_Tik; %thickness of the whole panel (Luminescent sheet + Waveguide)
AG_Tik=LSC_Tik-Cell_Tik; %thickness of air-gap below the PV cell

for Q=1:1:size(Panel_Width,2)
Panel Wth=Panel WidR(Q);

%
%-----Defining the Data Array for each Region-----
%
%Row 1-8: Contains vertices of the object
%Row 9: Name of Region, "Row 10 & 11": assigns the surface type: [bottom left top; right front back]

%Assigning coordinates for simple regularly spaced, alternating strips of LSC and PV cells placed side-by-side

%PV cells are spaced regularly apart with the remaining spaces between filled with LSC material.
LSC edgeWth=(Panel Wth-(Cell num*Cell Width))/(Cell num+1)*Cell_sep)/2; %length of LSC on the extreme edges of the panel
if LSC edgeWth<0, error('Panel width too small for PV and LSC size defined');end %error when total PV Cell width and spacing > Panel width
LSC edgeLen=(Panel_Length-Cell_Length)/2;
if LSC edgeLen<0, error('Panel length too small for PV and LSC size defined');end %error when PV Cell length > Panel length

for i=1:1:(Cell_num+1)
if i==1
LSC L=0; LSC R=LSC edgeWth; %left most LSC
PV L=LSC R; PV R=PV L+Cell_Width; %left most PV cell and air gap

LSC(:,i)=(LSC L LSC edgeLen 0;LSC L (LSC edgeLen+Cell_Length) 0;LSC R (LSC edgeLen+Cell_Length) 0;LSC R LSC edgeLen 0;...
LSC L LSC edgeLen LSC Tik;LSC L (LSC edgeLen+Cell_Length) LSC Tik;LSC R (LSC edgeLen+Cell_Length) LSC Tik;LSC R LSC edgeLen LSC Tik;...
'LSC' 'L';'Refract' 'Refract' 'Transp';'Refract' 'Transp' 'Transp');

PV(:,i)=(PV L LSC edgeLen AG_Tik;PV L (LSC edgeLen+Cell_Length) AG_Tik;PV R (LSC edgeLen+Cell_Length) AG_Tik;PV R LSC edgeLen AG_Tik;...
PV L LSC edgeLen LSC Tik;PV L (LSC edgeLen+Cell_Length) LSC Tik;PV R (LSC edgeLen+Cell_Length) LSC Tik;PV R LSC edgeLen LSC Tik;...
'PV' 'L';'Refract' 'Refract' 'Transp';'Refract' 'Refract' 'Refract' 'Refract' 'Refract' 'Refract');

air gap(:,i)=(PV L LSC edgeLen 0;PV L (LSC edgeLen+Cell_Length) 0;PV R (LSC edgeLen+Cell_Length) 0;PV R LSC edgeLen 0;...
PV L LSC edgeLen AG_Tik;PV L (LSC edgeLen+Cell_Length) AG_Tik;PV R (LSC edgeLen+Cell_Length) AG_Tik;PV R LSC edgeLen AG_Tik;...
'air gap' 'L';'Transp' 'Refract' 'Transp' 'Refract' 'Refract' 'Refract' 'Refract');

continue; %spaces control to the next loop iteration skipping the rest of the code below

elseif i==(Cell_num+1)
LSC L=PV R; LSC R=LSC L+LSC edgeWth; %right most LSC
LSC(:,i)=(LSC L LSC edgeLen 0;LSC L (LSC edgeLen+Cell_Length) 0;LSC R (LSC edgeLen+Cell_Length) 0;LSC R LSC edgeLen 0;...
LSC L LSC edgeLen LSC Tik;LSC L (LSC edgeLen+Cell_Length) LSC Tik;LSC R (LSC edgeLen+Cell_Length) LSC Tik;LSC R LSC edgeLen LSC Tik;...
'LSC' 'R';'Refract' 'Refract' 'Transp';'Refract' 'Transp' 'Transp');

break; %there is NO right most PV and air gap so don't define one
else
LSC L=PV R; LSC R=LSC L+Cell_sep; %all other LSC pieces in between
PV L=LSC R; PV R=PV L+Cell_Width; %all other PV cell and air gap pieces in between

end

LSC(:,i)=(LSC L LSC edgeLen 0;LSC L (LSC edgeLen+Cell_Length) 0;LSC R (LSC edgeLen+Cell_Length) 0;LSC R LSC edgeLen 0;...
LSC L LSC edgeLen LSC Tik;LSC L (LSC edgeLen+Cell_Length) LSC Tik;LSC R (LSC edgeLen+Cell_Length) LSC Tik;LSC R LSC edgeLen LSC Tik;...
'LSC' 'L';'Refract' 'Refract' 'Transp';'Refract' 'Transp' 'Transp');

PV(:,i)=(PV L LSC edgeLen AG_Tik;PV L (LSC edgeLen+Cell_Length) AG_Tik;PV R (LSC edgeLen+Cell_Length) AG_Tik;PV R LSC edgeLen AG_Tik;...
PV L LSC edgeLen LSC Tik;PV L (LSC edgeLen+Cell_Length) LSC Tik;PV R (LSC edgeLen+Cell_Length) LSC Tik;PV R LSC edgeLen LSC Tik;...
'PV' 'L';'Refract' 'Refract' 'Transp';'Refract' 'Refract' 'Refract' 'Refract' 'Refract' 'Refract');

```

```
air_gap(:,:,:1)=(PV_L_LSC_edgeLen 0;PV_L (LSC_edgeLen+Cell_Length) 0;PV_R (LSC_edgeLen+Cell_Length) 0;PV_R_LSC_edgeLen 0;...
PV_L_LSC_edgeLen AG_Tik;PV_L (LSC_edgeLen+Cell_Length) AG_Tik;PV_R (LSC_edgeLen+Cell_Length) AG_Tik;PV_R_LSC_edgeLen AG_Tik;...
'air_gap' ' ','','Refract' 'Transp';'Refract' 'Transp';'Refract' 'Refract');
end
LSC_Fr=[0 0 0;LSC_edgeLen 0;Panel_Wth LSC_edgeLen 0;Panel_Wth 0 0;...
0 0 LSC_Tik;0 LSC_edgeLen LSC_Tik;Panel_Wth LSC_edgeLen LSC_Tik;Panel_Wth 0 LSC_Tik;...
'LSC' ' ','','Refract' 'Reflect' 'Transp';'Reflect' 'Reflect' 'Transp']; %Front LSC piece
LSC_Bk=[0 (LSC_edgeLen+Cell_Length) 0;0 Panel_Length 0;Panel_Wth Panel_Length 0;Panel_Wth (LSC_edgeLen+Cell_Length) 0;...
0 (LSC_edgeLen+Cell_Length) LSC_Tik;0 Panel_Length LSC_Tik;Panel_Wth Panel_Length LSC_Tik;Panel_Wth (LSC_edgeLen+Cell_Length) LSC_Tik;...
'LSC' ' ','','Refract' 'Reflect' 'Transp';'Reflect' 'Transp' 'Reflect']; %Back LSC piece
WG=[0 0 LSC_Tik 0 Panel_Length LSC_Tik;Panel_Wth Panel_Length LSC_Tik;Panel_Wth 0 LSC_Tik;...
0 0 Panel_Tik 0 Panel_Length Panel_Tik;Panel_Wth Panel_Length Panel_Tik;Panel_Wth 0 Panel_Tik;...
'WG' ' ','','Transp' 'Refract';'Reflect' 'Reflect' 'Reflect']; %Waveguide
%.....Assignment of AIR space surround the whole panel.....
AIR_T=[0 0 Panel_Tik;0 Panel_Length Panel_Tik;Panel_Wth Panel_Length Panel_Tik;Panel_Wth 0 Panel_Tik;...
0 0 Panel_Tik+200;0 Panel_Length Panel_Tik+200;Panel_Wth Panel_Length Panel_Tik+200;Panel_Wth 0 Panel_Tik+200;...
'AIR' ' ','',' ',' ',''];
AIR_Bo=[0 0 -200;0 Panel_Length -200;Panel_Wth Panel_Length -200;Panel_Wth 0 -200;...
0 0 0;0 Panel_Length 0;Panel_Wth Panel_Length 0;Panel_Wth 0 0;...
'AIR' ' ',' ',' ',' ',''];
AIR_L=[-200 0 -200;-200 Panel_Length -200;0 Panel_Length -200;0 0 -200;...
-200 0 Panel_Tik+200;-200 Panel_Length Panel_Tik+200;0 Panel_Length Panel_Tik+200;0 0 Panel_Tik+200;...
'AIR' ' ',' ',' ',' ',''];
AIR_R=[Panel_Wth 0 -200;Panel_Wth Panel_Length -200;Panel_Wth+200 Panel_Length -200;Panel_Wth+200 0 -200;...
Panel_Wth 0 Panel_Tik+200;Panel_Wth Panel_Length Panel_Tik+200;Panel_Wth+200 Panel_Length Panel_Tik+200;Panel_Wth+200 0 Panel_Tik+200;...
'AIR' ' ',' ',' ',' ',''];
AIR_Fr=[-200 -200 -200; -200 0 -200;Panel_Wth+200 0 -200;Panel_Wth+200 -200 -200;...
-200 -200 Panel_Tik+200; -200 0 Panel_Tik+200;Panel_Wth+200 0 Panel_Tik+200;Panel_Wth+200 -200 Panel_Tik+200;...
'AIR' ' ',' ',' ',' ',''];
AIR_Bk=[-200 Panel_Length -200;-200 Panel_Length+200 -200;Panel_Wth+200 Panel_Length+200 -200;Panel_Wth+200 Panel_Length -200;...
-200 Panel_Length Panel_Tik+200;-200 Panel_Length+200 Panel_Tik+200;Panel_Wth+200 Panel_Length+200 Panel_Tik+200;Panel_Wth+200 Panel_Length Panel_Tik+200;...
'AIR' ' ',' ',' ',' ',''];
%-----
Region=cat(3,WG,LSC,LSC_Fr,LSC_Bk,PV,air_gap,AIR_T,AIR_Bo,AIR_L,AIR_R,AIR_Fr,AIR_Bk);
%creates a 3 Dimensional Array. Each layer in the 3rd Dimension contains the vertices for 1 Region
%-----
%-----END DATA Array-----
%-----
vertices=cell2mat(Region(1:end-3,:)); %Extracts the vertices discarding the rows containing the Region names and the Surface types
for i=1:size(vertices,3) %Defines the Planes bounding each region
%NOTE: all planes vertices are arranged in a clockwise direction looking from inside the Region out through the plane
Plane(:,1,i)=vertices(1,4,i); %bottom plane
Plane(:,2,i)=vertices(1,5,6,2,i); %left plane
Plane(:,3,i)=vertices(1,5,8,7,6,i); %top plane
Plane(:,4,i)=vertices(1,3,7,8,4,i); %right plane
Plane(:,5,i)=vertices(1,4,8,5,1,i); %front plane
Plane(:,6,i)=vertices(1,2,6,7,3,i); %back plane
end
%-----
%-----|Drawing the structure of the LSC Panel|-----
%-----
%set(gca,'CLim',[0 40]) % this sets the numerical scale of the colour map which cdata later references to
%face=[1 2 3 4; 5 6 2 5 6 7 8 4; 8 7 3; 1 5 8 4; 2 6 7 3]; % tells MATLAB which vertices in the array defines each face.
%NOTE: vertices in each row are connected in sequential order when plotted. (1 5 6 2) not the same as (1 2 5 6)
%for i=1:size(vertices,3)
% switch cell2mat(Region(end-2,1,i))
% case 'WG', face colour=1; edge colour='k'; face def='none'; %Wave Guide piece
% case 'LSC', face colour=1; edge colour='r'; face def='none'; %LSC piece
% case 'PV', face colour=8; edge colour='b'; face def='flat'; %PV Cell piece
% case 'air_gap', face colour=30; edge colour='none'; face def='none'; %air gap
% case 'AIR', face colour=25; edge colour={0.8 0.8 0.8}; face_def='none'; %sets face colour to grey using "face_def" ignoring the "face_colour" value
% otherwise, error('Region name undefined');
% end
% patch('Vertices',vertices(:,i),'Faces',face,'FaceColor','face_def','FaceVertexCData',face_colour,'EdgeColor',edge_colour)
% NOTE: need to set FaceColor to 'flat' or 'interp' else patch ignores values in FaceVertexCData
end
%axis([-10000 Panel_Wth+10000 -1000 Panel_Length+1000 -1000 Panel_Tik+1000]); %sets the limit of the plot axis: axis (xmin xmax ymin ymax)
%-----
%-----END Drawing LSC|-----
%-----
%-----|Ray Tracing Simulation |-----
%-----
%Spec=xlsread('Spectrum_280-2500nm','Spectra Prob','A2:B1583'); %reads excel file:Spectrum_380-1000nm, Sheet: Spectra Prob, Range:A2-B1583
%Col A: wavelengths in the solar spectrum
%Col B probability distribution of wavelength normalized to the peak emission = 1
%LSC_Spec=xlsread('Spectrum 280-2500nm','Spectra Prob','F2:H1583'); %Col F: wavelengths, Col G: LSC absorption, Col H: LSC emission
SSpec=importdata('SunSpec_280-2500nm.csv',''); %imports a csv file containing (1)solar spectrum wavelengths (2)probability distribution of wavelength normalized to the peak emission = 1
LSC_Spec=importdata('LR305_Pldata.csv',''); %imports a csv file containing (1)wavelength (2) LR305 absorption (3) LR305 emission at wavelengths in (1)
Imax=10000; %set maximum number of iterations for the path of each photon (to prevent endless looping)
iph_max=round(100000*((Cell_Len+Dist(Q)^2)/(Cell_Len+Dist(1)^2))); %total num of photons for the simulation. Maintain the same concentration for different area
ph_max=1000000; %fixed number of photons falling on the Panel
n_air=1; %refractive index of air
n_acrylic=1.491; %refractive index of acrylic. diff. wavelengths have diff. speed in acrylic. Do I want to account for the changing n?
x_ini=(1:(Panel_Wth/ph_max):Panel_Wth-1); %creates an array of positions for initial ray entry. MASKING: change range to simulate
y_ini=(1:(Panel_Length/ph_max):Panel_Length-1); %creates an array of positions for initial ray entry. MASKING: change range to simulate
%-----Tracking and Photon Collection Counters-----
SunWL_cnt=zeros(length(SSpec),1); %pre define an array to track the QTY of each wavelength from incident Solar irradiation
DyeEmWL_cnt=zeros(length(LSC_Spec),1); %pre define an array to track the QTY of each wavelength re-emitted by the Luminescent Dye
Hist_FVl=[]; %Histogram data for positions of Waveguided photons collected on the PV cell
FVdirAbs=0; %number of photons absorbed by PV from direct illumination
FVdirAbs_lpl=0; %number of photons absorbed by PV from direct illumination which have energy > 1.1eV (-1127nm & below)
FVdirAbs=0; %number of photons absorbed by PV from direct illumination photons by wavelength
FVindirAbs=0; %number of photons absorbed by PV from indirect photons in wave guide and other scattering methods (Indirect)
FVwlDir=0; %track the break down of collected waveguided photons by wavelength
%-----Photon Loss Counters-----
ph_reflect=0; %number of photons reflected off the top of the cell
ph_refract=0; %number of photons escaped through refraction (i.e. passes through panel without any absorption)
ph_refractscat=0; %photons refracted out by scattering ONLY and no absorption
ph_esc=0; %escape cone losses from SINGLE absorption
ph_escRE=0; %escape cone losses from RE-absorption
ph_nonRad=0; %non-radiatively losses in LSC form SINGLE absorption
ph_nonRadRE=0; %non-radiatively RE-absorption losses in LSC
ph_lost=0; %number of photons lost through other means
ph_cornr=0; %number of photons hitting the corners exactly. Record as a loss for now. Occurrence is rare and not expected to impact results
ph_err=0; %photons lost to errors in the code or something
ph_miss=0; %initial photon misses the hitting the panel
ph_stuck=0; %for photons that get trapped in air pockets (which they should not be)
%-----
%-----Loop counters used in the Raytrace loop-----
% i: photon/ray propagation path iteration number
```



```

Plane_2=circshift(Plane,[-1,0,0]); %shifts vertices of each plane in a circular manner moving 1 row up (as indicated by the dimension shifted)
%creates a replicate of the array "Plane" but with the vertices shifted. (ie. vertex 2 becomes 1, 3->2, 4->3 .... 1->last)

Interxn=Photon_pos+Photon_dir.*repmat(s_int,[1,size(Photon_dir,2),1,1]); %generate intersection points the Ray has with the various planes

%if Interxn is only used in the sum of angle test then we should convert it to an array the same size as "Plane" and "Plane 2"
TestPoint=repmat(Interxn,[size(Plane,1),1,1,1]); %expands the Intersection point array to make it the same size as the "Plane"
%sqrt(sum((vector.^2),2)); %square each element in vector => sum them up column wise => take the square root of the sum = Magnitude of vector
TestAngles=acos(dot(Plane_2-TestPoint,Plane-TestPoint,2)./(sqrt(sum(((Plane_2-TestPoint).^2),2)).*sqrt(sum(((Plane-TestPoint).^2),2))));
%calculates the angle between the TestPoint and each pair of points making up the polygon using "arccos((B.A)/(|B|*|A|))"

%radians to degrees %converts angles from radians to degrees. Not sure which has more precision error, "2*pi()" or "360 deg".

side_hit=logical(round_dp(sum(TestAngles,1),10)==round_dp(2*pi(),10))&logical(s_int>0); %round to 12 decimal places to prevent MATLAB induced precision
errors
%produces a logical array of all the Planes that have successful Ray-Plane intersections characterized by:
% (1) Intersection occurring in the photon direction "s_int">0. (2) Intersection point falls within the polygon boundary "sum(TestAngles=2*pi)"
RayPl_intxn=logical(sum(side_hit,3)==1); %Produces an array of all Regions that have "1 and only 1" Ray-Plane intersection (ie. 1 Boundary crossing)

if(not(any(RayPl_intxn))) %if All Regions have multiple Boundary crossing, then a "vertex intersection" might have occurred
RayPl_intxn=any(side_hit,3); %produces a logical array of all the Regions that have 1 or more successful Ray-Plane intersections
%There is no way to distinguish the correct Region from other regions in the path of the photon.
%This result must be combined with the "PIB test" to accurately place the photon.
end

%Intersection and PIB test overlap ONLY on the valid region.
%If PIB=1 => then the photon is sitting on a boundary between 2 Regions. But this also means it is leaving 1 region and entering another
Box_hit=RayPl_intxn&PIB; %this should give a Logical Array with a unique final Region selected

end

if (nnz(Box_hit)==1), ph_err=ph_err+1; break; end %error('Unable to determine a unique Photon location'); end %terminates current loop
zone=cell2mat(Region(end-2,1,Box_hit)); %extracts the photon region location using Matrix Logical Indexing

%=====End Photon Position and Heading test=====
%=====

switch zone
% Wave Guide
case 'WG'
Surface=cat(2,Region(end-1,1,Box_hit),Region(end,1,Box_hit)); %extracts surfaces types for the Planes bounding the photon's Region
surf_type=''; %resets surface type for the edge

%-----Re-uses Intersection test to find the intersection plane-----
zPlane=Plane(:,1,Box_hit); %extracts the Planes bounding the selected Zone/Region
zPlane_2=circshift(zPlane,[-1,0,0]);
zRef=zPlane(1,:); %extracts a reference point on each plane
zNormal=cross(zPlane(2,:),zPlane(1,:),zPlane(3,:))-zPlane(1,:); %obtains the normal for each plane
zPos=repmat([x(I),y(I),z(I)],[1,size(zRef,3)]); %creates an array with replicates of the photon's current position

zDir=repmat(direction,[1,size(zNormal,3)])*FP_Matx; %photon direction with remaining free-path length factored in.
%"direction" is a unit vector and hence we can directly multiply with FP_Matx to when including the free-path length
zInt=round_dp(dot(zNormal,zRef-zPos,2)./dot(zNormal,zDir,2),12); %the rounding to 12 decimal. Fewer decimal places and errors might occur

zInterxn=zPos+zDir.*repmat(z_int,[1,size(zDir,2),1]); %generates the Ray-Plane intersection points for each plane
zTestPoint=repmat(Interxn,[size(zPlane,1),1,1]); %make the intersection point array the same size as "zPlane"
zTestAngles=acos(dot(zPlane_2-zTestPoint,zPlane-zTestPoint,2)./(sqrt(sum(((zPlane_2-zTestPoint).^2),2)).*sqrt(sum(((zPlane-zTestPoint).^2),2))));

MATLAB induced precision error
%produces a logical array of all the Planes that have successful Ray-Plane intersections
%successful intersections must cross (1) within the boundaries of the plane (2) in front of the Ray (3) within the free-path length

if nnz(zSide_hit)>1, ph_err=ph_err+1; break; end %corner hits record as IOSB cos I don't know what to do with it at this time
%we can assume nnz(>1) Indicates corner hit because earlier Intersection + PIB test have filtered out other possibilities
%-----

if nnz(zSide_hit)==0 %no Ray-Plane intersection: Photon scattered before boundary collision
x(I+1)=x(I)+FP_Matx*x_dir; %new coordinates of Photon after travelling the free-path length and scattering
y(I+1)=y(I)+FP_Matx*y_dir;
z(I+1)=z(I)+FP_Matx*z_dir;
scatt_cnt=scatt_cnt+1; %track number scattering events
Theta=randi([0,180],1); %random deflection angle in all directions
Phi=randi([0,360],1);
x_dir=sind(Phi)*sind(Theta); y_dir=cosd(Phi)*sind(Theta); z_dir=cosd(Theta);
FP_Matx=MFP_Arry; %resets the Matrix free-path value
else %Boundary collision has occurred
surf_type=cell2mat(Surface(zSide_hit)); %selects the surface type for the edge
x(I+1)=round_dp(zInterxn(:,1,zSide_hit),3); y(I+1)=round_dp(zInterxn(:,2,zSide_hit),3); z(I+1)=round_dp(zInterxn(:,3,zSide_hit),3);
%round to 3 decimal places to prevent precision errors
zRay_dist=z_int(:,zSide_hit)*FP_Matx; %distance Ray has travelled
FP_Matx=round_dp(FP_Matx-zRay_dist,3); %Tracks remaining free-path of the photon in the matrix

switch surf_type
case 'Ttanap' %nothing to do
case 'ReflEct'
%Find the vector component of the Incident ray projected onto the plane Normal => (I.N)*N where "I"-incident ray, "N"-plane Normal
%Rearrange to give a vector combination that results in the Reflected ray
z_pNormal=zNormal(:,zSide_hit)/norm(zNormal(:,zSide_hit),2); %"unit" vector of the selected Plane normal
zReflEct=direction-2*dot(z_pNormal,direction,2)+z_pNormal; %vector of the "Reflected" ray
x_dir=zReflEct(1);y_dir=zReflEct(2);z_dir=zReflEct(3);
case 'RefrACT'
%Decomposes Incident vector in components parallel and perpendicular to the plane Normal vector: I=N*cos(theta)+M*sin(theta) where N is the
normal and M parallel to plane
%The Refracted/Transmitted vector is then recomposed: T=N*cos(theta)+M*sin(theta) => combining the 2: T=N*cos(theta)+[I-N*cos(theta)]*(sin(theta)/sin(theta))
%From snells law: sin(theta)/sin(theta1)=n1/n2. Using this relation and trigonometric manipulation to express T in terms of cos(theta), I and
(n1/n2) ONLY.

n_r=n_acrylic/n_air; %ray moving from WG to Air
z_pNormal=zNormal(:,zSide_hit)/norm(zNormal(:,zSide_hit),2); %"unit" vector of the selected Plane normal
cosNu_i=dot(z_pNormal,direction,2); %cosine of the angle between the incident ray and the plane Normal
cosNu_t=real(sqrt(1-(n_r^2*(1-cosNu_i^2)))); %cosine of the angle between the Reflected ray and the plane Normal
%Only the Real component is extracted for sqrt(x) for x<0, so Fresnels eqn can function properly.

R=Fresnel(n_acrylic,n_air,cosNu_i,cosNu_t); %Obtain reflection coefficient.
if rand(1)<=R %do probability check for reflection.
%total internal reflection
zReflEct=direction-2*dot(z_pNormal,direction,2)+z_pNormal; %vector of the "Reflected" ray
x_dir=zReflEct(1);y_dir=zReflEct(2);z_dir=zReflEct(3);
else %Photon refracted and escapes
zRefrACT=(cosNu_t-n_r*cosNu_i)+z_pNormal+(n_r*direction); %vector of the "Refracted" ray
%norm(a,2) can't be used for 3-dimensional and higher arrays. In such cases, magnitude has to be calculated explicitly for each element
%NOTE: for some reason to use the above equation, I must convert both the direction and normal vector to unit vectors. WHY is this so?
x_dir=zRefrACT(1);y_dir=zRefrACT(2);z_dir=zRefrACT(3);
end
otherwise, ph_err=ph_err+1; break %an unassigned edge_type should not occur if the code reaches this point
end
if y_dir<0, Phi=180-atand(x_dir/y_dir); else Phi=atand(x_dir/y_dir); end %updates Phi variable for checking purposes
Theta=acosd(z_dir); %updates Theta variable for checking purposes
end
% End Wave Guide

%=====

case 'LSC'
Surface=cat(2,Region(end-1,1,Box_hit),Region(end,1,Box_hit)); %extracts surfaces types for the Planes bounding the photon's Region
surf_type=''; %resets surface type for the edge
if (strcmp(zone_previous,'LSC')); %if previous zone was LSC, don't reset the LSC free-path
else FP_Lsc=MFP_LSC; end %Fresh entry of photon into LSC. Set LSC free-path to maximum

```

```

Free_Path=0;
Absor_Flag=0; %Flag to indicate if photon is absorbed or scattered
if FP_Matx==FP_lsc, Free_Path=FP_lsc; Absor_Flag=1; %check which remaining Free path value is higher, matrix or luminescent dye
else Free_Path=FP_Matx; Absor_Flag=2;
end

%-----Re-uses Intersection test to find the intersection plane-----
zPlane=Plane(:,z,Box_hit); %extracts the Planes bounding the selected Zone/Region
zPlane 2=cirshift(zPlane,[-1,0,0]);
zRef=zPlane(1,:); %extracts a reference point on each plane
zNormal=cross(zPlane(2,:),zPlane(1,:),zPlane(3,:)-zPlane(1,:),2); %obtains the normal for each plane
zPos=repmat([x(I),y(I),z(I)],1,1,size(zRef,3)); %creates an array with replicates of the photon's current position

zDir=repmat(direction,[1,1,size(zNormal,3)])*Free_Path; %photon direction with remaining free-path length factored in.
%direction is a unit vector and hence we can directly multiply with FP_Matx to when including the free-path length
z_int=round_dp(dot(zNormal,zRef-zPos,2)/dot(zNormal,zDir,2),12); %the rounding to 12 decimal. Fewer decimal places and errors might occur
zInterxn=zPos+zDir.*repmat(z_int,[1,size(zDir,2)]); %generates the Ray-Plane intersection points for each plane
zTestPoint=repmat(zInterxn,[size(zPlane,1),1]); %make the intersection point array the same size as "zPlane"
zTestAngles=acos(dot(zPlane_2-zTestPoint,zPlane-zTestPoint,2)/sqrt(sum((zPlane_2-zTestPoint).^2,2))); %sqrt(sum((zPlane-zTestPoint).^2,2));

zSide_hit=logical(round_dp(sum(zTestAngles,1),10)==round_dp(2*pi(),10)&logical(z_int>0)&logical(z_int<=1)); %round to 10 decimal places to prevent
MATLAB induced precision errors
%produces a logical array of all the Planes that have successful Ray-Plane intersections
%successful intersections must cross (1)within the boundaries of the plane (2)in front of the Ray (3)within the free-path length
if nnz(zSide_hit)>1, ph_cornr=ph_cornr+1; break; end %corner hits record as LOS cos I don't know what to do with it at this time
%we can assume nnz(>1) Indicates corner hit because earlier intersection + PIB test have filtered out other possibilities
%-----

if nnz(zSide_hit)==0 %no Ray-Plane intersection;
if Absor_Flag==2 %Scattering Event;
x(I+1)=x(I)+Free_Path*x_dir; %new coordinates of Photon after travelling the free-path length and scattering
y(I+1)=y(I)+Free_Path*y_dir;
z(I+1)=z(I)+Free_Path*z_dir;
scatt_cnt=scatt_cnt+1; %track number scattering events
Theta=randi([0,180],1); %random deflection angle in all directions
Phi=randi([0,360],1);
x_dir=sind(Phi)*sind(Theta); y_dir=cosd(Phi)*sind(Theta); z_dir=cosd(Theta);
FP_Matx=MFP_Acry; %resets the Matrix free-path value
FP_lsc=FP_lsc-Free_Path; %decrease remaining free-path for Luminescent particles
elseif Absor_Flag==1 %Absorption Event
x(I+1)=x(I)+Free_Path*x_dir; %new coordinates of Photon after travelling the free-path length
y(I+1)=y(I)+Free_Path*y_dir;
z(I+1)=z(I)+Free_Path*z_dir;
FP_Matx=FP_Matx-Free_Path; %decrease remaining free-path for Matrix background
abs_cnt=abs_cnt+1; %record absorption
if randi(1,1,1)<=0.45 %55 percent Quantum efficiency assumed
Theta=randi([0,180],1); %random emission angle in all directions
Phi=randi([0,360],1);
x_dir=sind(Phi)*sind(Theta); y_dir=cosd(Phi)*sind(Theta); z_dir=cosd(Theta);
em_cnt=em_cnt+1;
while em_cnt<=1
w1=randi(length(LSC_Spec)); % Select a wavelength at random
if rand(1)<=LSC_Spec(w1,3) % emission probability check using the wavelength selected
DyeEmiW1_cnt(w1)=DyeEmiW1_cnt(w1)+1; % keep track of the number of each wavelengths emitted
em_cnt=em_cnt+1; % ray emitted hence increment loop by 1, if no ray emitted, loop count is not incremented and
end % loop again. What we want is to not lose any rays to non-emission. Result is better that if we
lose rays.
end
MFP_LSC=abs(LSC_Tik/log(1-LSC_Spec(w1,2))); %recalculate mean free path in LSC for new wavelength
FP_lsc=MFP_LSC;
else %photon not re-emitted
if abs_cnt==1,ph_nonRad=ph_nonRad+1; break
else ph_nonRadRE=ph_nonRadRE+1; break; end %non-radiative losses: 1st absorption event recorded
%RE-absorption non-radiative losses
end
error('Unable to determine absorption or scattering event');
end
else %Boundary collision has occurred
surf_type=cell2mat(Surface(zSide_hit)); %selects the surface type for the edge
x(I+1)=round_dp(zInterxn(:,1,zSide_hit),3); y(I+1)=round_dp(zInterxn(:,2,zSide_hit),3); z(I+1)=round_dp(zInterxn(:,3,zSide_hit),3);
%round to 3 decimal places to prevent precision errors
zRay_dist=z_int(:,zSide_hit)*Free_Path; %distance Ray has travelled
FP_Matx=round_dp(FP_Matx-zRay_dist,3); %Tracks remaining free-path of the photon in the matrix
FP_lsc=round_dp(FP_lsc-zRay_dist,3); %Tracks remaining free-path of the photon in the luminescent material

switch surf_type
case 'Transp'
case 'Refract'
z_pNormal=zNormal(:,zSide_hit)/norm(zNormal(:,zSide_hit),2); %unit" vector of the selected Plane normal
zReflect=direction-2*dot(z_pNormal,direction,2)*z_pNormal; %vector of the "Reflected" ray
x_dir=zReflect(1);y_dir=zReflect(2);z_dir=zReflect(3);
case 'Refract'
n_r=n_acrylic/n_air; %ray moving from LSC to Air
z_pNormal=zNormal(:,zSide_hit)/norm(zNormal(:,zSide_hit),2); %unit" vector of the selected Plane normal
cosNu_i=dot(z_pNormal,direction,2); %cosine of the angle between the incident ray and the plane Normal
cosNu_t=real(sqrt(1-n_r^2*(1-cosNu_i^2))); %cosine of the angle between the Refracted ray and the plane Normal
%Only the Real component is extracted for sqrt(x) for x<0,so Fresnels eqn can function properly.
R=Fresnel(n_acrylic,n_air,cosNu_i,cosNu_t); %Obtain reflection coefficient.
if rand(1)<=R %do probability check for reflection.
%total internal reflection
zReflect=direction-2*dot(z_pNormal,direction,2)*z_pNormal; %unit vector of the "Reflected" ray
x_dir=zReflect(1);y_dir=zReflect(2);z_dir=zReflect(3);
else %Photon refracted and escapes
zRefract=(cosNu_t-n_r*cosNu_i)*z_pNormal+(n_r*direction); %unit vector of the "Refracted" ray
x_dir=zRefract(1);y_dir=zRefract(2);z_dir=zRefract(3);
end
otherwise, ph_err=ph_err+1; break %an unassigned edge_type should not occur if the code reaches this point
end
if y_dir<0, Phi=180-atand(x_dir/y_dir); else Phi=atand(x_dir/y_dir); end %updates Phi variable for checking purposes
Theta=acosd(z_dir); %updates Theta variable for checking purposes
end

%-----
%-----
LSC END

PV

case 'PV'
%-----Re-uses Intersection test to find the intersection plane-----
zPlane=Plane(:,z,Box_hit); %extracts the Planes bounding the selected Zone/Region
zPlane 2=cirshift(zPlane,[-1,0,0]);
zRef=zPlane(1,:); %extracts a reference point on each plane
zNormal=cross(zPlane(2,:),zPlane(1,:),zPlane(3,:)-zPlane(1,:),2); %obtains the normal for each plane
zPos=repmat([x(I),y(I),z(I)],1,1,size(zRef,3)); %creates an array with replicates of the photon's current position

zDir=repmat(direction,[1,1,size(zNormal,3)]); %photon direction
z_int=round_dp(dot(zNormal,zRef-zPos,2)/dot(zNormal,zDir,2),12); %the rounding to 12 decimal. Fewer decimal places and errors might occur
zInterxn=zPos+zDir.*repmat(z_int,[1,size(zDir,2)]); %generates the Ray-Plane intersection points for each plane
zTestPoint=repmat(zInterxn,[size(zPlane,1),1]); %make the intersection point array the same size as "zPlane"
zTestAngles=acos(dot(zPlane_2-zTestPoint,zPlane-zTestPoint,2)/sqrt(sum((zPlane_2-zTestPoint).^2,2))); %sqrt(sum((zPlane-zTestPoint).^2,2));

zSide_hit=logical(round_dp(sum(zTestAngles,1),10)==round_dp(2*pi(),10)&logical(z_int>0)); %round to 10 decimal places to prevent MATLAB induced
precision errors
%NOTE: conditions for successful hit differs from 'MFP' and 'LSC' blocks.
%successful intersections must cross (1)within the boundaries of the plane (2)in front of the Ray or at the current position
%-----

if (zSide_hit(:,3) && not(strcmp(zone_previous,'PV'))) %photon strikes "top" of PV cell (3rd element of zSide_hit) from "outside" the cell
if (abs_cnt==0 && reflc_cnt==0) && (scatt_cnt==0)
PVdirAbs=PVdirAbs+1; %photon absorbed on PV through direct illumination
end
end

```

```

        if SSpec(wl,1)<=1127, PVDdirAbs_lpl=PVDdirAbs_lpl+1; end %no of direct illumination photons with energy >1.1eV
        PVDdir(wl)=PVDdir(wl)+1; break
    else
        PVDdirAbs=PVDdirAbs+1; %photon absorbed on PV through wave guiding/reflections
        %Hist_PVI=[Hist_PVI; round(x(I)-LSC_edge)]; %add location photon was collected to the list
        Hist_PVI_cat(1,Hist_PVI,[round(x(I)) round(y(I))]); %add location photon was collected to the list
        PVDdir(wl)=PVDdir(wl)+1; break
    end
    else
        ph_lost=ph_lost+1; break %photon hits side or back of PV and is lost
    end
end
%-----
% PV END
%-----
% air gap
case 'air_gap'
    FP_Matx=MFP_Acry; %Photon moves out of the matrix. Reset the Matrix free-path values
    %NOTE LSC free-path value is tested and reset within the LSC code block
    SurfType=cat(2,Region(end-1,:),Box hit); %extracts surfaces types for the Planes bounding the photon's Region
    surf_type=''; %resets surface type for the edge
    %-----
    %Re-uses Intersection test to find the intersection plane-----
    zPlane=Plane(1,1,Box hit); %extracts the Planes bounding the selected Zone/Region
    zPlane_2=cirshift(zPlane,-1,0,0);
    zRef=zPlane(1,1); %extracts a reference point on each plane
    zNormal=cross(zPlane(2,1,:),zPlane(1,1,:),zPlane(3,1,:)-zPlane(1,1,:),2); %obtains the normal for each plane
    zPos= repmat([x(I),y(I),z(I)],1,1,size(zRef,3)); %creates an array with replicates of the photon's current position
    zDir= repmat(direction,[1,1,size(zNormal,3)]); %photon direction
    z_int=round_dp(dot(zNormal,zRef-zPos,2)/dot(zNormal,zDir,2),12); %the rounding to 12 decimal. Fewer decimal places and errors might occur
    zInterxn=zPos+zDir.*repmat(z_int,[1,size(zDir,2),1]); %generates the Ray-Plane intersection points for each plane
    zTestPoint=repmat(zInterxn,[size(zPlane,1),1,1]); %make the intersection point array the same size as "zPlane"
    zTestAngles=acos(dot(zPlane_2-zTestPoint,zPlane-zTestPoint,2)/(sqrt(sum((zPlane_2-zTestPoint).^2,2)).*sqrt(sum((zPlane-zTestPoint).^2,2))));
    zSide_hit=logical(round_dp(sum(zTestAngles,1),10)-round_dp(2*pi(1),10))&logical(z_int>0); %round to 10 decimal places to prevent MATLAB induced
precision errors
    %"NOTE": conditions for successful hit differs from 'WG', 'LSC' blocks.
    %successful intersections must cross (1)within the boundaries of the plane (2)in front of the Ray
    if nnz(zSide_hit)>1, ph_corner=ph_corner+1; break; end %Corner hits record as LOSS cos I don't know what to do with it at this time
    %we can assume nnz(>1) indicates corner hit because earlier Intersection + PIB test have filtered out other possibilities
    %-----
    if nnz(zSide_hit)==0, ph_stuck=ph_stuck+1; break; end %error('Photon stuck in airgap'); end %no intersection with any side; impossible in the air gap
    surf_type=cell2mat(Surface(zSide_hit)); %selects the surface type for the edge
    x(I+1)=round_dp(zInterxn(1,1,zSide_hit),3); y(I+1)=round_dp(zInterxn(1,2,zSide_hit),3); z(I+1)=round_dp(zInterxn(1,3,zSide_hit),3);
    %round to 3 decimal places to prevent precision errors
    switch surf_type
        case 'Transp' %nothing to do; either hits the back of the PV or escapes to AIR
        case 'Reflect'
            z_pNormal=zNormal(:,zSide_hit)/norm(zNormal(:,zSide_hit),2); %"unit" vector of the selected Plane normal
            zReflect=direction-2*dot(z_pNormal,direction,2)+z_pNormal; %vector of the "Reflected" ray
            x_dir=zReflect(1);y_dir=zReflect(2);z_dir=zReflect(3);
        case 'Refract'
            n_r=n_air/n_acrylic; %ray moving from 'air' to 'acrylic'
            z_pNormal=zNormal(:,zSide_hit)/norm(zNormal(:,zSide_hit),2); %"unit" vector of the selected Plane normal
            cosNu_i=dot(z_pNormal,direction,2); %cosine of the angle between the Incident ray and the plane Normal
            cosNu_t=real(sqrt(1-(n_r^2*(1-cosNu_i^2)))); %cosine of the angle between the Refracted ray and the plane Normal
            %Only the Real component is extracted for sqrt(x) for x<0,so Fresnels eqn can function properly.
            R=Fresnel(n_air,n_acrylic,cosNu_i,cosNu_t); %Obtain reflection coefficient. NOTE: photon moves from 'air' to 'acrylic'
            if rand(1)<R %Do probability check for reflection.
                %total internal reflection
                zReflect=direction-2*dot(z_pNormal,direction,2)+z_pNormal; %unit vector of the "Reflected" ray
                x_dir=zReflect(1);y_dir=zReflect(2);z_dir=zReflect(3);
            else %Photon refracted back into the LSC
                zRefract=(cosNu_t-n_r*cosNu_i)+z_pNormal*(n_r*direction); %unit vector of the "Refracted" ray
                x_dir=zRefract(1);y_dir=zRefract(2);z_dir=zRefract(3);
            end
        otherwise, ph_err=ph_err+1; break %an unassigned edge_type should not occur if the code reaches this point
    end
    if y_dir<0, phi=180+atan(x_dir/y_dir); else phi=atan(x_dir/y_dir); end %updates phi variable for checking purposes
    Theta=acos(z_dir); %updates Theta variable for checking purposes
    % air gap END
%-----
% AIR
case 'AIR'
    FP_Matx=MFP_Acry; %Photon moves out of the matrix. Reset the Matrix free-path values
    %NOTE LSC free-path value is tested and reset within the LSC code block
    %-----
    %Re-uses Intersection test to find the intersection plane-----
    zPlane=Plane(1,1,Box hit); %extracts the Planes bounding the selected Zone/Region
    zPlane_2=cirshift(zPlane,-1,0,0);
    zRef=zPlane(1,1); %extracts a reference point on each plane
    zNormal=cross(zPlane(2,1,:),zPlane(1,1,:),zPlane(3,1,:)-zPlane(1,1,:),2); %obtains the normal for each plane
    zPos= repmat([x(I),y(I),z(I)],1,1,size(zRef,3)); %creates an array with replicates of the photon's current position
    zDir= repmat(direction,[1,1,size(zNormal,3)]); %photon direction array
    z_int=round_dp(dot(zNormal,zRef-zPos,2)/dot(zNormal,zDir,2),12); %the rounding to 12 decimal. Fewer decimal places and errors might occur
    zInterxn=zPos+zDir.*repmat(z_int,[1,size(zDir,2),1]); %generates the Ray-Plane intersection points for each plane
    zTestPoint=repmat(zInterxn,[size(zPlane,1),1,1]); %make the intersection point array the same size as "zPlane"
    zTestAngles=acos(dot(zPlane_2-zTestPoint,zPlane-zTestPoint,2)/(sqrt(sum((zPlane_2-zTestPoint).^2,2)).*sqrt(sum((zPlane-zTestPoint).^2,2))));
    zSide_hit=logical(round_dp(sum(zTestAngles,1),10)-round_dp(2*pi(1),10))&logical(z_int>0); %round to 10 decimal places to prevent MATLAB induced
precision errors
    %"NOTE": conditions for successful hit differs from 'WG', 'LSC' blocks.
    %successful intersections must cross (1)within the boundaries of the plane (2)in front of the Ray
    if nnz(zSide_hit)>1, ph_corner=ph_corner+1; break; end %Corner hits record as LOSS cos I don't know what to do with it at this time
    %we can assume nnz(>1) indicates corner hit because earlier Intersection + PIB test have filtered out other possibilities
    %-----
    if nnz(zSide_hit)==0, ph_stuck=ph_stuck+1; break; end %error('Photon stuck in AIR'); end %no intersection with any side; impossible in the AIR
surrounding the Panel
    %???should I put a counter to catch this error but continue simulating with the next photon??
    %Assumes initial ray is always coming from the top of the panel.
    if I==1
        if z_dir<0 %only concerned with downward pointing rays
            x(I+1)=round_dp(zInterxn(1,1,zSide_hit),3); y(I+1)=round_dp(zInterxn(1,2,zSide_hit),3); z(I+1)=round_dp(zInterxn(1,3,zSide_hit),3); %advance
            photon to the top interface
            %round to 3 decimal places to prevent precision errors
            if (zSide_hit(1,1)) %zSide_hit(1,1) indicates if Ray-Plane intersection occurred on the 'Top' of the WG (ie. bottom of top AIR zone)
                %Ray intersects with the top of the panel successfully
                n_r=n_air/n_acrylic; %ray moving from 'air' to 'acrylic'
                z_pNormal=zNormal(:,zSide_hit)/norm(zNormal(:,zSide_hit),2); %"unit" vector of the selected Plane normal
                cosNu_i=dot(z_pNormal,direction,2); %cosine of the angle between the Incident ray and the plane Normal
                cosNu_t=real(sqrt(1-(n_r^2*(1-cosNu_i^2)))); %cosine of the angle between the Refracted ray and the plane Normal
                %Only the Real component is extracted for sqrt(x) for x<0,so Fresnels eqn can function properly.
                R=Fresnel(n_air,n_acrylic,cosNu_i,cosNu_t); %Obtain reflection coefficient. NOTE: photon moves from 'air' to 'acrylic'
                if rand(1)<R %Do probability check for reflection.
                    %reflection off the top
                    zReflect=direction-2*dot(z_pNormal,direction,2)+z_pNormal; %unit vector of the "Reflected" ray
                    x_dir=zReflect(1);y_dir=zReflect(2);z_dir=zReflect(3);
                else
                    %refraction into the panel
                    zRefract=(cosNu_t-n_r*cosNu_i)+z_pNormal*(n_r*direction); %unit vector of the "Refracted" ray
                    x_dir=zRefract(1);y_dir=zRefract(2);z_dir=zRefract(3);
                end
            end
        end
    end
end
%-----
% WG END
%-----
end

```



```

x(I+2)=x(I+1)+x_dir*100; y(I+2)=y(I+1)+y_dir*100; z(I+2)=z(I+1)+z_dir*100; %for visualization purpose; to see the photon path as it
escapes
    ph_reflect=ph_reflect+1; break %Photon reflected and lost. Track their count and initiate next photon.
    else
        %Photon refracted and enters waveguide
        zRefract=(cosNu_t-n_r*cosNu_i)*z_pNormal+(n_r*direction); %unit vector of the "Refracted" ray
        x_dir=zRefract(1);y_dir=zRefract(2);z_dir=zRefract(3);
        if y_dir<0, Phi=180-atand(x_dir/y_dir); else Phi=atand(x_dir/y_dir); end %updates Phi variable for checking purposes
        Theta=acosd(z_dir); %updates Theta variable for checking purposes
    end
    else
        ph_miss=ph_miss+1; break %Ray misses the top of the panel
    end
    else
        ph_miss=ph_miss+1; break %Initial rays pointing in the wrong direction; Count as miss hits
    end
    else
        x(I+1)=x(I)+x_dir*100; y(I+1)=y(I)+y_dir*100; z(I+1)=z(I)+z_dir*100; %for visualization purpose; to see the photon path as it escapes
        %if Ray-Tracing loop is not in the 1st iteration it means photon has escaped out of the Wave-Guide;
        if (abs_cnt==0)&&(scatt_cnt==0), ph_refract=ph_refract+1; break %un-absorbed and non-WG losses
        elseif (abs_cnt==0)&&(scatt_cnt>0), ph_refractScat=ph_refractScat+1; break %un-absorbed and scattered out of WG
        elseif (abs_cnt==1), ph_esc=ph_esc+1; break % escape cone losses
        elseif (abs_cnt>1), ph_escRE=ph_escRE+1; break % RE-absorption escape cone losses
    end
end
%-----
end % AIR END
%-----
I=I+1; %increment loop counter
zone_previous=zone; %keeps track of where the photon was in previously
end
%plot the photon path
%line(x,y,z,'Color','g','LineWidth',1,'LineStyle','-','Marker','o') % adds a line to the current plot/axis without deleting the current plot (as opposed to plot
function)
%if (abs_cnt==0)&&(reflc_cnt==0), line(x,y,z,'Color',[0.7,0.7,0.7],'LineWidth',1,'LineStyle','-'), end %plot only reflected photons
%-----end of Photon Tracking Loop-----
end
%if ph_err>1, break, end
%if ph_reflect>1, break, end
%-----end Emission Probability Check-----
end
%-----|End Ray Tracing Simulation|-----
%-----
Enh_Fact=(PVindirAbs+PVdirAbs_ipi)/PVdirAbs_ipi;
Percn_LSC=1-((Cell_Length*Cell_Width*Cell_num)/(Panel_Length*Panel_Wth));

sheet='sheet1';
row=strcat('A',num2str(Q+1));
%----for saving Histogram data-----
col1=strcat(char(64+2*Q-1),'1');
col2=strcat(char(64+2*Q-1),'2');
%-----
xlswrite('Raytrace3D_data.xls',{'ph_nonRad','ph_nonRadRE','ph_cornr','ph_err','ph_refract','ph_refractScat','ph_esc','ph_escRE','ph_lost','ph_reflect','ph_miss','PVdirAbs',
'PVdirAbs_ipi','PVindirAbs','ph_max','Panel_Width','Enh_Fact','% LSC'},sheet,'A1')
xlswrite('Raytrace3D_data.xls',[ph_nonRad,ph_nonRadRE,ph_cornr,ph_err,ph_refract,ph_refractScat,ph_esc,ph_escRE,ph_lost,ph_reflect,ph_miss,PVdirAbs,PVdirAbs_ipi,PVindirAbs,
ph_max,Panel_Width,Enh_Fact,Percn_LSC],sheet,row)
%dlmwrite('Raytrace3D_data.csv',[ph_nonRad,ph_nonRadRE,ph_cornr,ph_err,ph_refract,ph_refractScat,ph_esc,ph_escRE,ph_lost,ph_reflect,ph_miss,PVdirAbs,PVdirAbs_ipi,PVindirAbs
,ph_max,Panel_Width,Enh_Fact,Percn_LSC],'-append','newline','pc');
%Write simulation data into a .csv file. Have not figure out how to write a text array properly into a csv file yet.

%Record data on position where waveguided/scattered photon are absorbed on to the PV cell
xlswrite('Raytrace3D_Histo.xls',{'Hist_PVi'},sheet,col1)
xlswrite('Raytrace3D_Histo.xls',Hist_PVi,sheet,col2)
%dlmwrite('Raytrace3D_Histo.csv',Hist_PVi,'-append','offset',2);
%write Histogram data into a .csv file.

%Record data on Solar and Luminescent emission wavelength distribution
%xlswrite('Raytrace3D_data.xls',{'Wave_Length','SunWL_cnt','DyeEmiWL_cnt','PVwldir','PVwldirDir'},sheet,'R1')
%xlswrite('Raytrace3D_data.xls',[Sspec(:,1),SunWL_cnt,DyeEmiWL_cnt,PVwldir,PVwldirDir],sheet,'R2')

end

```

Bibliography

- [1] P. Lorenz and Dickon, "The economics of solar power," *McKinsey Q.*, pp. 1–10, 2008.
- [2] V. Fthenakis, J. E. Mason, and K. Zweibel, "The technical, geographical, and economic feasibility for solar energy to supply the energy needs of the US," *Energy Policy*, vol. 37, no. 2, pp. 387–399, Feb. 2009.
- [3] B. Norton, P. C. Eames, T. K. Mallick, M. J. Huang, S. J. McCormack, J. D. Mondol, and Y. G. Yohanis, "Enhancing the performance of building integrated photovoltaics," *Sol. Energy*, vol. 85, no. 8, pp. 1629–1664, Aug. 2011.
- [4] M. Oliver and T. Jackson, "Energy and economic evaluation of building-integrated photovoltaics," *Energy*, vol. 26, no. 4, pp. 431–439, Apr. 2001.
- [5] G. Kocher-Oberlehner, M. Bardosova, M. Pemble, and B. S. Richards, "Planar photonic solar concentrators for building-integrated photovoltaics," *Sol. Energy Mater. Sol. Cells*, vol. 104, pp. 53–57, Sep. 2012.
- [6] C. Zomer, A. Nobre, P. Cassatella, T. Reindl, and R. R  ther, "The balance between aesthetics and performance in building-integrated photovoltaics in the tropics," *Prog. Photovolt. Res. Appl.*, vol. 22, no. 7, pp. 744–756, Jul. 2014.
- [7] L. Stamenic, E. Smiley, and K. Karim, "Low light conditions modelling for building integrated photovoltaic (BIPV) systems," *Sol. Energy*, vol. 77, no. 1, pp. 37–45, Jan. 2004.
- [8] J. Nelson, *The physics of solar cells*. London : River Edge, NJ: Imperial College Press ; Distributed by World Scientific Pub. Co, 2003.
- [9] A. Izadian, A. Pourtaherian, and S. Motahari, "Basic model and governing equation of solar cells used in power and control applications," in *2012 IEEE Energy Conversion Congress and Exposition (ECCE)*, 2012, pp. 1483–1488.
- [10] S. Silvestre and A. Chouder, "Effects of shadowing on photovoltaic module performance," *Prog. Photovolt. Res. Appl.*, vol. 16, no. 2, pp. 141–149, Mar. 2008.
- [11] R. Ramaprabha and B. L. Mathur, "Impact of partial shading on solar PV module containing series connected cells," *Int. J. Recent Trends Eng.*, vol. 2, no. 7, pp. 56–60, Nov. 2009.

- [12] V. Quaschnig and R. Hanitsch, "Numerical simulation of current-voltage characteristics of photovoltaic systems with shaded solar cells," *Sol. Energy*, vol. 56, no. 6, pp. 513–520, Jun. 1996.
- [13] R. Koeppe, N. S. Sariciftci, and A. Büchtemann, "Enhancing photon harvesting in organic solar cells with luminescent concentrators," *Appl. Phys. Lett.*, vol. 90, no. 18, pp. 181126–181126–3, May 2007.
- [14] M. J. Currie, J. K. Mapel, T. D. Heidel, S. Goffri, and M. A. Baldo, "High-Efficiency Organic Solar Concentrators for Photovoltaics," *Science*, vol. 321, no. 5886, pp. 226–228, Jul. 2008.
- [15] G. V. Shcherbatyuk, R. H. Inman, C. Wang, R. Winston, and S. Ghosh, "Viability of using near infrared PbS quantum dots as active materials in luminescent solar concentrators," *Appl. Phys. Lett.*, vol. 96, no. 19, pp. 191901–191901–3, May 2010.
- [16] R. Koeppe, O. Bossart, G. Calzaferri, and N. S. Sariciftci, "Advanced photon-harvesting concepts for low-energy gap organic solar cells," *Sol. Energy Mater. Sol. Cells*, vol. 91, no. 11, pp. 986–995, Jul. 2007.
- [17] B. C. Rowan, L. R. Wilson, and B. S. Richards, "Advanced Material Concepts for Luminescent Solar Concentrators," *IEEE J. Sel. Top. Quantum Electron.*, vol. 14, no. 5, pp. 1312–1322, Oct. 2008.
- [18] R. Reisfeld, "Prospects of sol–gel technology towards luminescent materials," *Opt. Mater.*, vol. 16, no. 1–2, pp. 1–7, Feb. 2001.
- [19] S. J. Gallagher, B. Norton, and P. C. Eames, "Quantum dot solar concentrators: Electrical conversion efficiencies and comparative concentrating factors of fabricated devices," *Sol. Energy*, vol. 81, no. 6, pp. 813–821, Jun. 2007.
- [20] J. Bomm, A. Büchtemann, A. J. Chatten, R. Bose, D. J. Farrell, N. L. A. Chan, Y. Xiao, L. H. Slooff, T. Meyer, A. Meyer, W. G. J. H. M. van Sark, and R. Koole, "Fabrication and full characterization of state-of-the-art quantum dot luminescent solar concentrators," *Sol. Energy Mater. Sol. Cells*, vol. 95, no. 8, pp. 2087–2094, Aug. 2011.
- [21] A. M. Hermann, "Luminescent solar concentrators—A review," *Sol. Energy*, vol. 29, no. 4, pp. 323–329, 1982.
- [22] W. H. Weber and J. Lambe, "Luminescent greenhouse collector for solar radiation," *Appl. Opt.*, vol. 15, no. 10, pp. 2299–2300, Oct. 1976.
- [23] C. F. Rapp and N. L. Boling, "Luminescent solar concentrators," in *13th Photovoltaic Specialists Conference*, 1978, vol. -1, pp. 690–693.

- [24] A. Goetzberger and W. Greube, "Solar energy conversion with fluorescent collectors," *Appl. Phys. Mater. Sci. Process.*, vol. 14, no. 2, pp. 123–139, 1977.
- [25] D. Chemisana, "Building Integrated Concentrating Photovoltaics: A review," *Renew. Sustain. Energy Rev.*, vol. 15, no. 1, pp. 603–611, Jan. 2011.
- [26] J. W. E. Wiegman and E. van der Kolk, "Building integrated thin film luminescent solar concentrators: Detailed efficiency characterization and light transport modelling," *Sol. Energy Mater. Sol. Cells*, vol. 103, pp. 41–47, Aug. 2012.
- [27] B. Rezaie, E. Esmailzadeh, and I. Dincer, "Renewable energy options for buildings: Case studies," *Energy Build.*, vol. 43, no. 1, pp. 56–65, Jan. 2011.
- [28] M. G. Debijs and P. P. C. Verbunt, "Thirty Years of Luminescent Solar Concentrator Research: Solar Energy for the Built Environment," *Adv. Energy Mater.*, vol. 2, no. 1, pp. 12–35, Jan. 2012.
- [29] L. H. Slooff, E. E. Bende, A. R. Burgers, T. Budel, M. Pravettoni, R. P. Kenny, E. D. Dunlop, and A. Büchtemann, "A luminescent solar concentrator with 7.1% power conversion efficiency," *Phys. Status Solidi RRL - Rapid Res. Lett.*, vol. 2, no. 6, pp. 257–259, Dec. 2008.
- [30] L. H. Slooff, R. Kinderman, A. R. Burgers, A. Büchtemann, R. Danz, T. B. Meyer, A. J. Chatten, D. Farrell, K. W. J. Barnham, and J. A. M. van Roosmalen, "The luminescent concentrator illuminated," presented at the Society of Photo-Optical Instrumentation Engineers (SPIE) Conference Series, 2006, vol. 6197, p. 17.
- [31] B. S. Richards, "Enhancing the performance of silicon solar cells via the application of passive luminescence conversion layers," *Sol. Energy Mater. Sol. Cells*, vol. 90, no. 15, pp. 2329–2337, Sep. 2006.
- [32] E. Klampaftis, D. Ross, K. R. McIntosh, and B. S. Richards, "Enhancing the performance of solar cells via luminescent down-shifting of the incident spectrum: A review," *Sol. Energy Mater. Sol. Cells*, vol. 93, no. 8, pp. 1182–1194, Aug. 2009.
- [33] C. Strümpel, M. McCann, G. Beaucarne, V. Arkhipov, A. Slaoui, V. Švrček, C. del Cañizo, and I. Tobias, "Modifying the solar spectrum to enhance silicon solar cell efficiency—An overview of available materials," *Sol. Energy Mater. Sol. Cells*, vol. 91, no. 4, pp. 238–249, Feb. 2007.
- [34] E. Klampaftis and B. S. Richards, "Improvement in multi-crystalline silicon solar cell efficiency via addition of luminescent material to EVA encapsulation layer," *Prog. Photovolt. Res. Appl.*, vol. 19, no. 3, pp. 345–351, 2011.

- [35] C. Corrado, S. W. Leow, M. Osborn, E. Chan, B. Balaban, and S. A. Carter, "Optimization of gain and energy conversion efficiency using front-facing photovoltaic cell luminescent solar concentrator design," *Sol. Energy Mater. Sol. Cells*, vol. 111, pp. 74–81, Apr. 2013.
- [36] A. . Mansour, "On enhancing the efficiency of solar cells and extending their performance life," *Polym. Test.*, vol. 22, no. 5, pp. 491–495, Aug. 2003.
- [37] R. Reisfeld, M. Eyal, V. Chernyak, and R. Zusman, "Luminescent solar concentrators based on thin films of polymethylmethacrylate on a polymethylmethacrylate support," *Sol. Energy Mater.*, vol. 17, no. 6, pp. 439–455, Oct. 1988.
- [38] L. R. Wilson and B. S. Richards, "Measurement method for photoluminescent quantum yields of fluorescent organic dyes in polymethyl methacrylate for luminescent solar concentrators," *Appl. Opt.*, vol. 48, no. 2, pp. 212–220, Jan. 2009.
- [39] S. W. Leow, C. Corrado, M. Osborn, M. Isaacson, G. Alers, and S. A. Carter, "Analyzing luminescent solar concentrators with front-facing photovoltaic cells using weighted Monte Carlo ray tracing," *J. Appl. Phys.*, vol. 113, no. 21, p. 214510, Jun. 2013.
- [40] S. W. Leow, C. Corrado, M. Osborn, and S. A. Carter, "Monte Carlo ray-tracing simulations of luminescent solar concentrators for building integrated photovoltaics," 2013, vol. 8821, pp. 882103–882103–7.
- [41] L. H. Slooff, R. Kinderman, A. R. Burgers, A. Büchtemann, R. Danz, T. B. Meyer, A. J. Chatten, D. Farrell, K. W. J. Barnham, and J. A. M. van Roosmalen, "The luminescent concentrator illuminated," in *Photonics for Solar Energy Systems: Proceedings of SPIE*, Strasbourg, France, 2006, p. 61970K–61970K–8.
- [42] M. Carrascosa, S. Unamuno, and F. Agullo-Lopez, "Monte Carlo simulation of the performance of PMMA luminescent solar collectors," *Appl. Opt.*, vol. 22, no. 20, pp. 3236–3241, Oct. 1983.
- [43] S. J. Gallagher, P. C. Eames, and B. Norton, "Quantum dot solar concentrator behaviour, predicted using a ray trace approach," *Int. J. Ambient Energy*, vol. 25, no. 1, pp. 47–56, 2004.
- [44] A. Burgers, L. Slooff, R. Kinderman, and J. Van Roosmalen, "Modelling of luminescent concentrators by ray-tracing," in *Presented at the 20th European Photovoltaic Solar Energy Conference and Exhibition*, Barcelona, Spain, 2005, vol. 6, p. 10.
- [45] A. Schüler, A. Kostro, C. Galande, M. Valle del Olmo, E. Chambrier, and B. Huriel, "Principles of Monte-Carlo Ray-Tracing Simulations of Quantum Dot Solar Concentrators," in *Proceedings of ISES World Congress 2007 (Vol. I – Vol. V)*, D. Y. Goswami and Y. Zhao, Eds. Springer Berlin Heidelberg, 2009, pp. 1033–1037.

- [46] D. Şahin, B. Ilan, and D. F. Kelley, "Monte-Carlo simulations of light propagation in luminescent solar concentrators based on semiconductor nanoparticles," *J. Appl. Phys.*, vol. 110, no. 3, pp. 033108–033108–8, Aug. 2011.
- [47] M. Bendig, J. Hanika, H. Dammertz, J. C. Goldschmidt, M. Peters, and M. Weber, "Simulation of fluorescent concentrators," in *Interactive Ray Tracing, 2008. RT 2008. IEEE Symposium on*, Los Angeles, California, USA, 2008, pp. 93–98.
- [48] W. G. J. H. M. van Sark, K. W. J. Barnham, L. H. Slooff, A. J. Chatten, A. Büchtemann, A. Meyer, S. J. McCormack, R. Koole, D. J. Farrell, R. Bose, E. E. Bende, A. R. Burgers, T. Budel, J. Quilitz, M. Kennedy, T. Meyer, C. D. M. Donegá, A. Meijerink, and D. Vanmaekelbergh, "Luminescent Solar Concentrators - A review of recent results," *Opt. Express*, vol. 16, no. 26, pp. 21773–21792, Dec. 2008.
- [49] M. Kennedy, A. Chatten, D. Farrell, R. Bose, A. Büchtemann, S. McCormack, J. Doran, B. Norton, and K. Barnham, "Thermodynamic Modelling and Ray-trace Modelling of Luminescent Solar Concentrators: a Comparison of the two Approaches," in *23rd European Photovoltaic Solar Energy Conference and Exhibition*, Valencia, Spain, 2008, pp. 334 – 337.
- [50] A. J. Chatten, D. Farrel, C. Jermyn, P. Thomas, B. F. Buxton, A. Buchtemann, R. Danz, and K. W. Barnham, "Thermodynamic modelling of luminescent solar concentrators," in *Photovoltaic Specialists Conference, 2005. Conference Record of the Thirty-first IEEE*, 2005, pp. 82–85.
- [51] P. Poli, L. Rota, and C. Jacoboni, "Weighted Monte Carlo for electron transport in semiconductors," *Appl. Phys. Lett.*, vol. 55, no. 10, pp. 1026–1028, Sep. 1989.
- [52] S. Portolan, R. C. Iotti, and F. Rossi, "Microscopic modelling of semiconductor-based infrared photodetectors: a weighted Monte Carlo approach," *Semicond. Sci. Technol.*, vol. 19, no. 4, pp. S107–S109, Apr. 2004.
- [53] M. Avellaneda, R. Buff, C. Friedman, N. Grandechamp, L. Kruk, and J. Newman, "Weighted Monte Carlo: A new technique for calibrating asset-pricing models," *Int. J. Theor. Appl. Finance*, vol. 04, no. 01, pp. 91–119, Feb. 2001.
- [54] M. E. Mortenson, "Intersections," in *Computer graphics handbook : geometry and mathematics*, 1st ed., New York, N.Y.: Industrial Press, 1990, pp. 195–204.
- [55] J. O'Rourke, "Search and Intersection," in *Computational geometry in C*, 2nd ed., Cambridge, UK; New York, NY, USA: Cambridge University Press, 1998, pp. 220–293.
- [56] J. H. Hannay, "Polarization of sky light from a canopy atmosphere," *New J. Phys.*, vol. 6, no. 1, p. 197, Dec. 2004.

- [57] Y. Liu and K. Voss, "Polarized radiance distribution measurement of skylight. II. Experiment and data," *Appl. Opt.*, vol. 36, no. 33, pp. 8753–8764, Nov. 1997.
- [58] C. F. Bohren, "Atmospheric Optics," in *The Optics Encyclopedia*, Wiley-VCH Verlag GmbH & Co. KGaA, 2007.
- [59] S. N. Kasarova, N. G. Sultanova, C. D. Ivanov, and I. D. Nikolov, "Analysis of the dispersion of optical plastic materials," *Opt. Mater.*, vol. 29, no. 11, pp. 1481–1490, Jul. 2007.
- [60] NOAA, US Department of Commerce, "ESRL Global Monitoring Division - GRAD Group," *NOAA Solar Calculator*. [Online]. Available: <http://www.esrl.noaa.gov/gmd/grad/solcalc/>. [Accessed: 02-Nov-2012].
- [61] M. G. Debije, P. P. C. Verbunt, B. C. Rowan, B. S. Richards, and T. L. Hoeks, "Measured surface loss from luminescent solar concentrator waveguides," *Appl. Opt.*, vol. 47, no. 36, pp. 6763–6768, Dec. 2008.
- [62] W. R. L. Thomas, J. M. Drake, and M. L. Lesiecki, "Light transport in planar luminescent solar concentrators: the role of matrix losses," *Appl. Opt.*, vol. 22, no. 21, pp. 3440–3450, Nov. 1983.
- [63] W. A. Badawy, "A review on solar cells from Si-single crystals to porous materials and quantum dots," *J. Adv. Res.*
- [64] G. Chen, J. Seo, C. Yang, and P. N. Prasad, "Nanochemistry and nanomaterials for photovoltaics," *Chem. Soc. Rev.*, vol. 42, no. 21, pp. 8304–8338, Oct. 2013.
- [65] N. S. Lewis, "Toward Cost-Effective Solar Energy Use," *Science*, vol. 315, no. 5813, pp. 798–801, Feb. 2007.
- [66] S. Huang and G. Conibeer, "Sputter-grown Si quantum dot nanostructures for tandem solar cells," *J. Phys. Appl. Phys.*, vol. 46, no. 2, p. 024003, Jan. 2013.
- [67] X. Wang, G. I. Koleilat, J. Tang, H. Liu, I. J. Kramer, R. Debnath, L. Brzozowski, D. A. R. Barkhouse, L. Levina, S. Hoogland, and E. H. Sargent, "Tandem colloidal quantum dot solar cells employing a graded recombination layer," *Nat. Photonics*, vol. 5, no. 8, pp. 480–484, Aug. 2011.
- [68] L. Dou, J. You, J. Yang, C.-C. Chen, Y. He, S. Murase, T. Moriarty, K. Emery, G. Li, and Y. Yang, "Tandem polymer solar cells featuring a spectrally matched low-bandgap polymer," *Nat. Photonics*, vol. 6, no. 3, pp. 180–185, Mar. 2012.

- [69] J. Tang and E. H. Sargent, "Infrared Colloidal Quantum Dots for Photovoltaics: Fundamentals and Recent Progress," *Adv. Mater.*, vol. 23, no. 1, pp. 12–29, Jan. 2011.
- [70] G. Zhai, C. P. Church, A. J. Breeze, D. Zhang, G. B. Alers, and S. A. Carter, "Quantum dot PbS_{0.9}Se_{0.1}/TiO₂ heterojunction solar cells," *Nanotechnology*, vol. 23, no. 40, p. 405401, Oct. 2012.
- [71] C. P. Church, E. Muthuswamy, G. Zhai, S. M. Kauzlarich, and S. A. Carter, "Quantum dot Ge/TiO₂ heterojunction photoconductor fabrication and performance," *Appl. Phys. Lett.*, vol. 103, no. 22, p. 223506, Nov. 2013.
- [72] I. Gur, "Air-Stable All-Inorganic Nanocrystal Solar Cells Processed from Solution," *Science*, vol. 310, no. 5747, pp. 462–465, Oct. 2005.
- [73] J. Tang, G. Konstantatos, S. Hinds, S. Myrskog, A. G. Pattantyus-Abraham, J. Clifford, and E. H. Sargent, "Heavy-Metal-Free Solution-Processed Nanoparticle-Based Photodetectors: Doping of Intrinsic Vacancies Enables Engineering of Sensitivity and Speed," *ACS Nano*, vol. 3, no. 2, pp. 331–338, Feb. 2009.
- [74] H. M. Haverinen, R. . Myllylä, and G. E. Jabbour, "Inkjet Printed RGB Quantum Dot-Hybrid LED," *J. Disp. Technol.*, vol. 6, no. 3, pp. 87–89, Mar. 2010.
- [75] H. M. Haverinen, R. A. Myllylä, and G. E. Jabbour, "Inkjet printing of light emitting quantum dots," *Appl. Phys. Lett.*, vol. 94, no. 7, p. 073108, Feb. 2009.
- [76] M. Singh, H. M. Haverinen, P. Dhagat, and G. E. Jabbour, "Inkjet Printing-Process and Its Applications," *Adv. Mater.*, vol. 22, no. 6, pp. 673–685, Feb. 2010.
- [77] S. Maenosono, T. Okubo, and Y. Yamaguchi, "Overview of Nanoparticle Array Formation by Wet Coating," *J. Nanoparticle Res.*, vol. 5, no. 1–2, pp. 5–15, Apr. 2003.
- [78] F. C. Krebs, S. A. Gevorgyan, and J. Alstrup, "A roll-to-roll process to flexible polymer solar cells: model studies, manufacture and operational stability studies," *J. Mater. Chem.*, vol. 19, no. 30, pp. 5442–5451, Jul. 2009.
- [79] H. Lee, M. Wang, P. Chen, D. R. Gamelin, S. M. Zakeeruddin, M. Grätzel, and M. K. Nazeeruddin, "Efficient CdSe Quantum Dot-Sensitized Solar Cells Prepared by an Improved Successive Ionic Layer Adsorption and Reaction Process," *Nano Lett.*, vol. 9, no. 12, pp. 4221–4227, Dec. 2009.
- [80] S. E. Habas, H. A. S. Platt, M. F. A. M. van Hest, and D. S. Ginley, "Low-Cost Inorganic Solar Cells: From Ink To Printed Device," *Chem. Rev.*, vol. 110, no. 11, pp. 6571–6594, Nov. 2010.

- [81] E. G. Barbagiovanni, D. J. Lockwood, P. J. Simpson, and L. V. Goncharova, "Quantum confinement in Si and Ge nanostructures," *J. Appl. Phys.*, vol. 111, no. 3, p. 034307, Feb. 2012.
- [82] A. M. Smith and S. Nie, "Semiconductor Nanocrystals: Structure, Properties, and Band Gap Engineering," *Acc. Chem. Res.*, vol. 43, no. 2, pp. 190–200, Feb. 2010.
- [83] L. E. Brus, "Electron–electron and electron-hole interactions in small semiconductor crystallites: The size dependence of the lowest excited electronic state," *J. Chem. Phys.*, vol. 80, no. 9, pp. 4403–4409, May 1984.
- [84] L. E. Brus, "A simple model for the ionization potential, electron affinity, and aqueous redox potentials of small semiconductor crystallites," *J. Chem. Phys.*, vol. 79, no. 11, pp. 5566–5571, Dec. 1983.
- [85] W. Shockley and H. J. Queisser, "Detailed Balance Limit of Efficiency of p-n Junction Solar Cells," *J. Appl. Phys.*, vol. 32, no. 3, pp. 510–519, Mar. 1961.
- [86] D. Timmerman, I. Izeddin, P. Stallinga, I. N. Yassievich, and T. Gregorkiewicz, "Space-separated quantum cutting with silicon nanocrystals for photovoltaic applications," *Nat. Photonics*, vol. 2, no. 2, pp. 105–109, Feb. 2008.
- [87] Y. Teng, J. Zhou, X. Liu, S. Ye, and J. Qiu, "Efficient broadband near-infrared quantum cutting for solar cells," *Opt. Express*, vol. 18, no. 9, pp. 9671–9676, Apr. 2010.
- [88] D. Chen, Y. Wang, and M. Hong, "Lanthanide nanomaterials with photon management characteristics for photovoltaic application," *Nano Energy*, vol. 1, no. 1, pp. 73–90, Jan. 2012.
- [89] B. M. van der Ende, L. Aarts, and A. Meijerink, "Lanthanide ions as spectral converters for solar cells," *Phys. Chem. Chem. Phys.*, vol. 11, no. 47, p. 11081, 2009.
- [90] D. Chen, L. Lei, A. Yang, Z. Wang, and Y. Wang, "Ultra-broadband near-infrared excitable upconversion core/shell nanocrystals," *Chem. Commun.*, vol. 48, no. 47, p. 5898, 2012.
- [91] X. Huang, S. Han, W. Huang, and X. Liu, "Enhancing solar cell efficiency: the search for luminescent materials as spectral converters," *Chem. Soc. Rev.*, vol. 42, no. 1, p. 173, 2013.
- [92] A. J. Nozik, M. C. Beard, J. M. Luther, M. Law, R. J. Ellingson, and J. C. Johnson, "Semiconductor Quantum Dots and Quantum Dot Arrays and Applications of Multiple Exciton Generation to Third-Generation Photovoltaic Solar Cells," *Chem. Rev.*, vol. 110, no. 11, pp. 6873–6890, Nov. 2010.

- [93] A. J. Nozik, "Quantum dot solar cells," *Phys. E Low-Dimens. Syst. Nanostructures*, vol. 14, no. 1–2, pp. 115–120, Apr. 2002.
- [94] R. J. Ellingson, M. C. Beard, J. C. Johnson, P. Yu, O. I. Micic, A. J. Nozik, A. Shabaev, and A. L. Efros, "Highly Efficient Multiple Exciton Generation in Colloidal PbSe and PbS Quantum Dots," *Nano Lett.*, vol. 5, no. 5, pp. 865–871, May 2005.
- [95] M. C. Beard, J. M. Luther, O. E. Semonin, and A. J. Nozik, "Third Generation Photovoltaics based on Multiple Exciton Generation in Quantum Confined Semiconductors," *Acc. Chem. Res.*, vol. 46, no. 6, pp. 1252–1260, Jun. 2013.
- [96] V. I. Klimov, "Spectral and Dynamical Properties of Multiexcitons in Semiconductor Nanocrystals," *Annu. Rev. Phys. Chem.*, vol. 58, no. 1, pp. 635–673, May 2007.
- [97] D. S. Boudreaux, F. Williams, and A. J. Nozik, "Hot carrier injection at semiconductor-electrolyte junctions," *J. Appl. Phys.*, vol. 51, no. 4, pp. 2158–2163, Apr. 1980.
- [98] J. Drbohlavova, V. Adam, R. Kizek, and J. Hubalek, "Quantum Dots — Characterization, Preparation and Usage in Biological Systems," *Int. J. Mol. Sci.*, vol. 10, no. 2, pp. 656–673, Feb. 2009.
- [99] C. Su, B.-Y. Hong, and C.-M. Tseng, "Sol-gel preparation and photocatalysis of titanium dioxide," *Catal. Today*, vol. 96, no. 3, pp. 119–126, Oct. 2004.
- [100] J. Park, J. Joo, S. G. Kwon, Y. Jang, and T. Hyeon, "Synthesis of Monodisperse Spherical Nanocrystals," *Angew. Chem. Int. Ed.*, vol. 46, no. 25, pp. 4630–4660, Jun. 2007.
- [101] R. D. Tilley, "Synthesis and applications of nanoparticles and quantum dots," *Chem. N. Z.*, pp. 146–150, 2008.
- [102] T. Ju, R. L. Graham, G. Zhai, Y. W. Rodriguez, A. J. Breeze, L. Yang, G. B. Alers, and S. A. Carter, "High efficiency mesoporous titanium oxide PbS quantum dot solar cells at low temperature," *Appl. Phys. Lett.*, vol. 97, no. 4, p. 043106, Jul. 2010.
- [103] A. C. Arango, L. R. Johnson, V. N. Bliznyuk, Z. Schlesinger, S. A. Carter, and H.-H. Hörhold, "Efficient Titanium Oxide/Conjugated Polymer Photovoltaics for Solar Energy Conversion," *Adv. Mater.*, vol. 12, no. 22, pp. 1689–1692, Nov. 2000.
- [104] Y. Liu, M. Gibbs, J. Puthussery, S. Gaik, R. Ihly, H. W. Hillhouse, and M. Law, "Dependence of Carrier Mobility on Nanocrystal Size and Ligand Length in PbSe Nanocrystal Solids," *Nano Lett.*, vol. 10, no. 5, pp. 1960–1969, May 2010.

- [105] V. P. Kunets, M. Rebello Sousa Dias, T. Rembert, M. E. Ware, Y. I. Mazur, V. Lopez-Richard, H. A. Mantooth, G. E. Marques, and G. J. Salamo, "Electron transport in quantum dot chains: Dimensionality effects and hopping conductance," *J. Appl. Phys.*, vol. 113, no. 18, p. 183709, 2013.
- [106] C.-Y. Kuo, M.-S. Su, C.-S. Ku, S.-M. Wang, H.-Y. Lee, and K.-H. Wei, "Ligands affect the crystal structure and photovoltaic performance of thin films of PbSe quantum dots," *J. Mater. Chem.*, vol. 21, no. 31, p. 11605, 2011.
- [107] D. V. Talapin, J.-S. Lee, M. V. Kovalenko, and E. V. Shevchenko, "Prospects of Colloidal Nanocrystals for Electronic and Optoelectronic Applications," *Chem. Rev.*, vol. 110, no. 1, pp. 389–458, Jan. 2010.
- [108] E. Muthuswamy, A. S. Iskandar, M. M. Amador, and S. M. Kauzlarich, "Facile Synthesis of Germanium Nanoparticles with Size Control: Microwave versus Conventional Heating," *Chem. Mater.*, vol. 25, no. 8, pp. 1416–1422, Apr. 2013.
- [109] M. C. Beard, K. P. Knutsen, P. Yu, J. M. Luther, Q. Song, W. K. Metzger, R. J. Ellingson, and A. J. Nozik, "Multiple Exciton Generation in Colloidal Silicon Nanocrystals," *Nano Lett.*, vol. 7, no. 8, pp. 2506–2512, Aug. 2007.
- [110] G. Conibeer, M. Green, R. Corkish, Y. Cho, E.-C. Cho, C.-W. Jiang, T. Fangsuwannarak, E. Pink, Y. Huang, T. Puzzer, T. Trupke, B. Richards, A. Shalav, and K. Lin, "Silicon nanostructures for third generation photovoltaic solar cells," *Thin Solid Films*, vol. 511–512, pp. 654–662, Jul. 2006.
- [111] E.-C. Cho, S. Park, X. Hao, D. Song, G. Conibeer, S.-C. Park, and M. A. Green, "Silicon quantum dot/crystalline silicon solar cells," *Nanotechnology*, vol. 19, no. 24, p. 245201, Jun. 2008.
- [112] G. Conibeer, M. Green, E.-C. Cho, D. König, Y.-H. Cho, T. Fangsuwannarak, G. Scardera, E. Pink, Y. Huang, T. Puzzer, S. Huang, D. Song, C. Flynn, S. Park, X. Hao, and D. Mansfield, "Silicon quantum dot nanostructures for tandem photovoltaic cells," *Thin Solid Films*, vol. 516, no. 20, pp. 6748–6756, Aug. 2008.
- [113] D. Neiner, H. W. Chiu, and S. M. Kauzlarich, "Low-Temperature Solution Route to Macroscopic Amounts of Hydrogen Terminated Silicon Nanoparticles," *J. Am. Chem. Soc.*, vol. 128, no. 34, pp. 11016–11017, Aug. 2006.
- [114] J. Zou, P. Sanelle, K. A. Pettigrew, and S. M. Kauzlarich, "Size and Spectroscopy of Silicon Nanoparticles Prepared via Reduction of SiCl₄," *J. Clust. Sci.*, vol. 17, no. 4, pp. 565–578, Dec. 2006.

- [115] T. M. Atkins, A. Y. Louie, and S. M. Kauzlarich, "An efficient microwave-assisted synthesis method for the production of water soluble amine-terminated Si nanoparticles," *Nanotechnology*, vol. 23, no. 29, p. 294006, Jul. 2012.
- [116] K. W. Cheah, T. Chan, W. L. Lee, D. Teng, W. H. Zheng, and Q. M. Wang, "Multiple peak photoluminescence of porous silicon," *Appl. Phys. Lett.*, vol. 63, no. 25, pp. 3464–3466, Dec. 1993.
- [117] K. Sattler, "Chapter 2 - The energy gap of clusters, nanoparticles, and quantum dots," in *Handbook of Thin Films*, H. S. Nalwa, Ed. Burlington: Academic Press, 2002, pp. 61–97.